UNIVERSITY OF OKLAHOMA

GRADUATE COLLEGE

AN INTEGRATED DIAGENETIC AND PALEOMAGNETIC STUDY OF THE HAYNESVILLE SHALE, HARRISON COUNTY, TEXAS

A THESIS

SUBMITTED TO THE GRADUATE FACULTY

in partial fulfillment of the requirements for the

Degree of

MASTER OF SCIENCE

By

ALEXANDER KEITH BENTON
Norman, Oklahoma
2013

AN INTEGRATED DIAGENETIC AND PALEOMAGNETIC STUDY OF THE HAYNESVILLE SHALE, HARRISON COUNTY, TEXAS

A THESIS APPROVED FOR THE
CONOCO PHILLIPS SCHOOL OF GEOLOGY AND GEOPHYSICS

BY

[redacted]
Dr. R. Douglas Elmore, Chair

[redacted]
Dr. Mike Engel

[redacted]
Dr. Richard Andrews

Acknowledgements

So many people have been incredibly generous over the past two years and have made this research possible. I would like to begin by thanking GMX Resources and Samson Energy for allowing me to sample the cores used for this study. The foundation for this study was set in place by the tremendous work Dr. Elmore and his past students have done incorporating diagenesis and paleomagnetism, and without their foresight this study would not have been possible. I would like to thank Dr. Elmore for his guidance and direction in this research and for enabling me to pursue both my academic and professional goals. Thank you also to Dr. Andrews and Dr. Engel for their time and feedback as members of my committee.

The camaraderie of my fellow graduate students did not play an insignificant role in my success and enjoyment while here at O.U., and I would like the thank them. For this research I would like to specifically thank Shannon Dulin and Sarah Farzaneh for their input and advice.

My parents from an early age set a foundation for pursuing academic success and hard work, and I want to thank them, as well as my brother, for their unwavering support and encouragement as I grew up.

Lastly I thank my wife Brooke. When I came back to school it was just the two of us embarking on the journey. Now we have two wonderful boys because of her dedication and love. Never once was she impatient or frustrated with the time this work and process required, and without her support I most certainly would not have accomplished this goal.

Table of Contents

List of Tables

List of Figures

Abstract

An integrated diagenetic and paleomagnetic study of the Upper Jurassic Haynesville Shale was undertaken to determine the origin and timing of diagenetic events in this prolific shale-gas unit. Characterization of diagenesis in the Haynesville has not previously been conducted utilizing paleomagnetism. Distinguishing different diagenetic events and their extent within the reservoir has scalable impacts on production within the Haynesville Shale, particularly as related to the presence of natural vertical healed fractures. Two unoriented cores from Harrison County, Texas were sampled, described, and utilized in this study.

Five facies were described through petrographic analysis: siliceous mudstone, laminated siliceous mudstone, carbonate-rich mudstone, burrowed mudstone, and dolostone. Scanning electron and transmitting microscope analysis shows a complex paragenetic sequence within these facies and associated healed fractures including the presence of sphalerite, barite, celestite, anhydrite, double terminating quartz, and leucoxene. Horizontal veins are interpreted as early diagenetic events, and vertical veins and brecciation are interpreted as late events. Heterogeneity within vertical veins may indicate multiple activation events and certainly multiple exposures to diagenetic fluids.

Through thermal demagnetization a low temperature component was uncovered with moderate to steep inclinations interpreted as a viscous remanent magnetization (VRM) in a few specimens. An intermediate temperature component (160-320°C) with moderate to steep inclinations is interpreted as a chemical remanent magnetization (CRM) residing in pyrrhotite. A higher temperature component (300-480°C) with

moderate inclination is also interpreted as a CRM, with magnetization held in magnetite. Low temperature demagnetization resulted in a small decrease in magnetic intensity and in some cases increased maximum unblocking temperatures of the intermediate and higher temperature components. A drilling induced remanent magnetization (DIRM) was ruled out through Q-factor analysis. Inclination values of intermediate and high temperature CRMs from both cores are utilized because few specimens had a well-defined VRM that could be used for core orientation. Inclinations for the CRM residing in magnetite show possible remagnetizations occurring in the Late Jurassic/Early Cretaceous or Late Cretaceous/Middle Cenozoic. The intermediate temperature CRM is a Late Cretaceous to Cenozoic remagnetization. Because the intermediate temperature CRM may have an inclination direction associated with the Cenozoic, core orientation of the Snider A1-H was attempted through rotating these directions to the present-day direction (0°). Based on the rotation, the magnetite CRM has a good grouping and a Paleogene/Neogene pole position on the apparent polar wander path (APWP). The two cores contain moderate total organic carbon (TOC) values (~2-4 wt %) and the origin of magnetite remanence may be attributed to burial processes such as maturation of organic matter which occurred at ~140 Ma. Other burial processes such as dissolution-reprecipitation of pyrite may have triggered precipitation of authigenic magnetite. Alternatively, late diagenetic basinal fluids could have caused a Paleogene/Neogene remagnetization. A presence/absence test around veins in the cores yielded no conclusive results in regards to basinal remagnetizing fluids. The pyrrhotite remanence is interpreted as forming through thermochemical

sulfate reduction (TSR) relating to hydrocarbons perhaps as early as the Late Cretaceous.

1. Introduction

The objective of this study is to conduct an integrated paleomagnetic, petrographic, and geochemical study of two cores of the Haynesville Shale from Harrison County Texas (Figure 1A). Facies descriptions were completed through examination of the cores and thin section analysis. Diagenetic features and mineralogy were determined using a petrographic microscope and a scanning electron microscope in order to establish a paragenetic sequence. Paleomagnetic techniques were utilized to ascertain timing of diagenetic events in both cores. Strontium isotope data was used to determine origin of fluids that altered the rock.

Diagenetic events can exert a strong control on reservoir porosity and permeability and can also influence a rock's fracability, particularly for shale gas units like the Haynesville Shale. Characterizing the creation and destruction of secondary porosity is very important when analyzing a tight unconventional reservoir. Most research studies of shale gas units like the Haynesville have focused on the depositional history and the origin of the porosity and permeability with relatively few studies focusing on the diagenesis. Paleomagnetic analysis can be used to date diagenetic events such as maturation of organic matter (Banerjee et al. 1997; Blumstein et al. 2004; Elmore et al. 2012) and/or fluid migration events (Dennie et al. 2012). Determining the timing of such events can have implications for hydrocarbon exploration strategies. Determining timing and origin of diagenetic events, including development of a paragenetic sequence, will further characterize the Haynesville reservoir and is one aim of this study.

The diagenesis of shales has received less study than other lithologies such as sandstones and carbonates, and fundamental issues about shale diagenesis remain to be resolved. For example, the question of whether they are open or closed systems is currently the subject of debate (e.g. Land et al. 1997; Bjorlykke and Jahren 2012). This study will investigate the role of external and internal fluids in causing alteration of the Haynesville Shale.

Although research has been done characterizing the Haynesville from different approaches, it has not previously been undertaken integrating paleomagnetism and diagenesis. Paleomagnetism on shales and mudstones is a relatively new field as traditional paleomagnetic studies have centered on rocks with higher concentrations of iron oxides. Paleomagnetic studies from cores are also few in number as, conventionally, studies are done through outcrop sampling, and shales are difficult to sample in outcrop. Thorough diagenetic studies on shales have until recently (Dennie 2010; Deng 2011; Manning 2011) also been neglected and this research aims to add to that scientific knowledge base.

A.

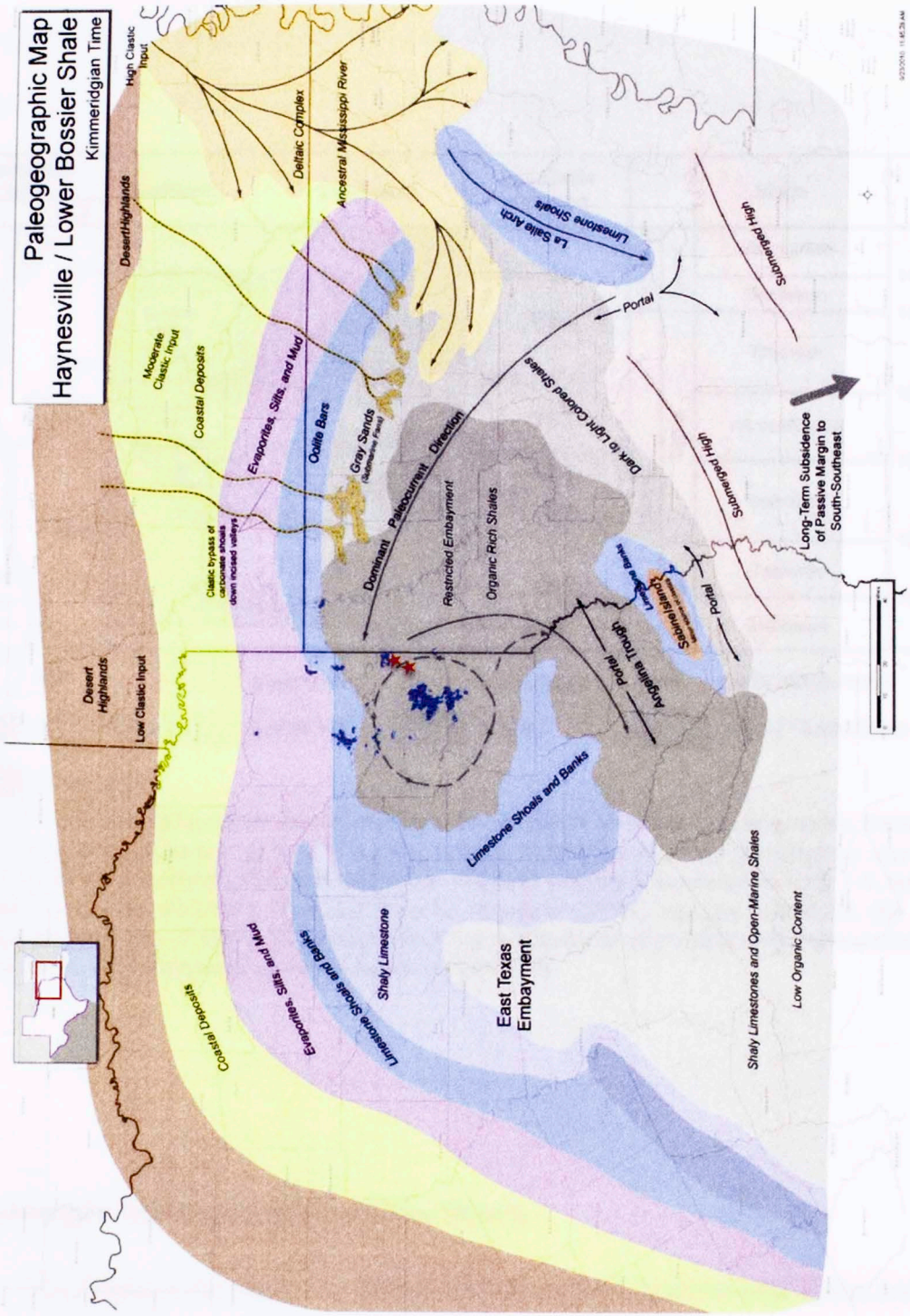
Paleogeographic Map
Haynesville / Lower Bossier Shale
Kimmeridgian Time
High Clastic Input
Deserthighlands
Deltaic Complex
Ancestral Mississippi River
La Salle Arch
Limestone Shoals
Sabinetown High
Portal
Moderate Clastic Input
Coastal Deposits
Evaporites, Silts and Mud
Oolite Bars
Gray Sands
Clastic bypass of carbonate shoals down incised valleys
Dominant Paleocurrent Direction
Restricted Embayment
Organic Rich Shales
Dark to Light Colored Shales
Sabinetown High
Long-Term Subsidence of Passive Margin to South-Southeast
Desert Highlands
Low Clastic Input
Angelina Trough
Portal
Limestone Shoals and Banks
Coastal Deposits
Evaporites, Silts and Mud
Limestone Shoals and Banks
Shaly Limestone
East Texas Embayment
Shaly Limestones and Open-Marine Shales
Low Organic Content

B.

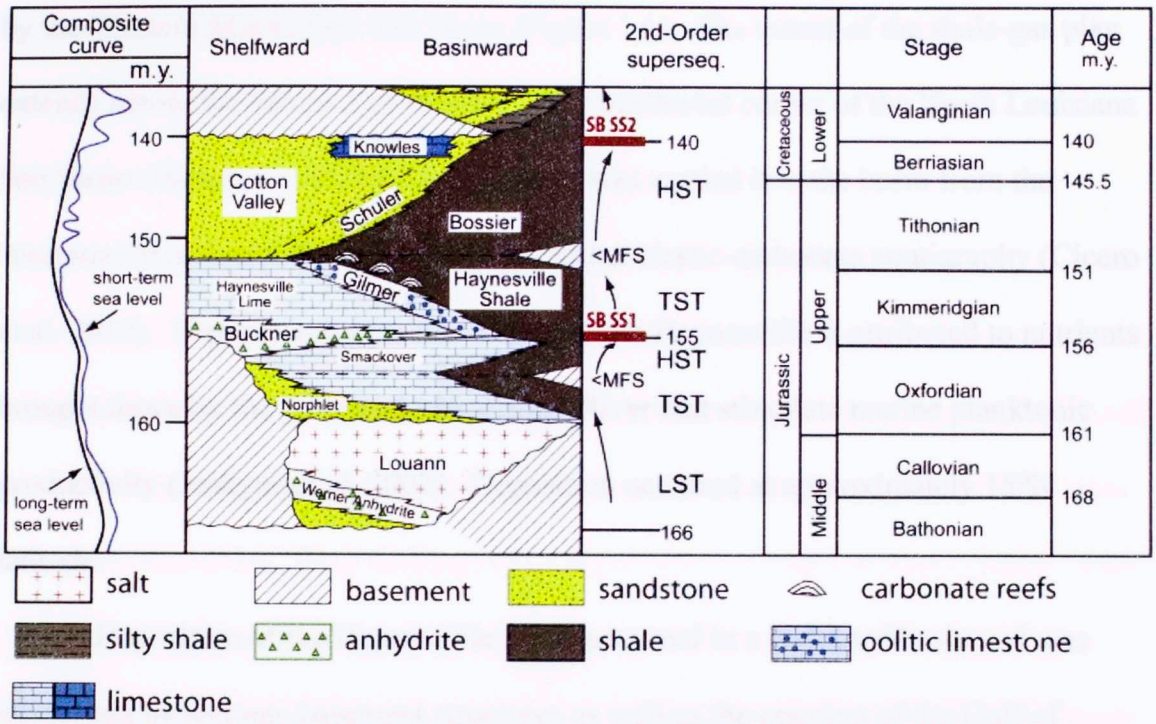

Figure 1: (A)Paleogeographic map of the Haynesville Shale showing key geographic features at time of deposition (Kimmeridgian). Location of cores in Harrison county indicated by stars. The Snider A1-H core, latitude: 34.65086 longitude: -94.0601 and the Coleman Gas Unit 1-6, latitude: 32.54661 longitude: -94.15967. Modified from Dr. Sommer (2010), courtesy of GMXR. (B) Stratigraphic column of Haynesville Shale showing sequence stratigraphic correlations and a long-term sea level composite curve (Hammes et al. 2011)

2. Geologic Setting and Previous Work

The Haynesville Shale is a calcareous mudstone located in east Texas and reaches into northwest Louisiana (Spain and Anderson 2010). It was deposited during the Late Jurassic, Kimmeridgian time, and lies at depths ranging from approximately 10,000 to 11,975 feet (Parker et al. 2009). It overlays an organic rich lime mudstone, the Smackover Formation, and is overlain by the Bossier Shale. The

paleogeographic distribution of the Haynesville was bounded to the west by the East Texas Salt Basin, to the south by the Sabine and Natchitoches Islands and to the east by the Western Mississippi Salt Basin (Figure 1A). The extent of the shale-gas play extends across the Sabine Uplift and into the northwest corner of the North Louisiana Salt Basin (Hammes et al. 2011). Sediment was carried into the basin from the Ancestral Mississippi River creating a complex clastic-carbonate stratigraphy (Cicero et al. 2010). Organic matter accumulation in the Haynesville is attributed to nutrients brought down by the Ancestral Mississippi River that stimulate marine planktonic productivity (Jenkyns et al. 2002). Deposition occurred at approximately 15°N latitude.

Deposition of the Haynesville Shale occurred in a restricted basin and was influenced by tectonic basement structures as well as the opening of the Gulf of Mexico (Spain and Anderson 2010). The Late Triassic and Early Jurassic marked the beginning of the separation of the North and South American plate. This produced many grabens and also produced volcanic activity throughout the future Gulf of Mexico region. It was not until the Late Jurassic that marine conditions became predominant in the region, the Gulf began to form and the Ancestral Mississippi became a source of clastic sediment influx into the basin (Salvador 1987). Connection to the modern Atlantic did not occur until the very end of the Jurassic and basin formation has been hypothesized to occur from the Yucatan block moving south away from the North American plate (Salvador 1987). Sedimentary rocks in the Gulf of Mexico are not older than the Middle to Early Triassic, further supporting the theory that it was at this time that the paleo-Gulf was forming. During the early

Kimmeridgian, the basin began to experience more prevalent regression, allowing for the formation of evaporites (Salvador 1987). During this time the Gulf was connected with the Pacific Ocean spanning across central Mexico. Transitioning into the late Kimmeridgian, the areas along the northwest rim of the Gulf that had evaporite formation now were being covered by carbonates due to transgression (Salvador 1987). The eastern portion of the Gulf geography was dominated by clastic influx from the Ancestral Mississippi prograding out into the deepest part of the basin where shales were deposited. During the Late Kimmeridgian the Yucatan and Florida blocks were above sea level, and it is likely that they greatly impacted the restriction of the Atlantic Ocean from influencing circulation in the Gulf (Salvador 1987). This restriction is favorable for creating anoxic and euxinic conditions critical for preservation of organics in the paleo-Gulf during deposition of the Haynesville Shale.

From the Late Triassic to the Late Jurassic two separate major tectonic periods occurred. The first period beginning in the Late Triassic and extending through the Middle Jurassic was marked by extension and the creation of many grabens and rift basins as the Yucatan block rotated south. The second period, which is time equivalent to the deposition of the Haynesville shale, is marked by a relative decrease in tectonic activity. This allowed for subsidence in the newly formed basin and created ample accommodation space for incoming clastics via the Ancestral Mississippi River (Salvador 1987).

Paleoclimate determination yields invaluable data for looking at processes controlling deposition of sediments and marine life required to create an organic-rich basin. Common problems arise, however, when analyzing the Jurassic paleoclimate.

Most of the available data are spatially distant and from varying times within the period, and the data yield poor stratigraphic controls which makes climatic trends difficult to place together (Abbink et al. 2001). Another inherent issue with attaining reliable paleoclimate data is its dependence upon topography, which is destroyed through weathering (Moore et al. 1992). During the deposition of the Haynesville in the Upper Jurassic, the Earth's climate was in a greenhouse with virtually no ice on the planet (Sellwood et al. 2000). The absence of polar ice caps has a large impact on ocean circulation in that the lack of cold bottom waters (~4°C) moving from high latitudes into mid and low-latitudes thwarts a great amount of circulation from occurring, in part due to the imbalance of varying surface and bottom water temperatures. The cold nutrient-rich currents coming from the poles serve to oxidize the ocean during icehouse conditions. A lack of ocean current circulation favors anoxic bottom water conditions that are required to avoid oxidation of organic matter. The Middle Jurassic was marked by humid conditions that then became increasingly arid and warmer up to the Late Jurassic (Kimmeridgian) (Abbink et al. 2001). Contrasted with today, the Kimmeridgian was a time of tremendous rainfall over the oceans while the continents were quite arid and the poles saw much more precipitation (Sellwood et al. 2000). The Gulf of Mexico during the Kimmeridgian is widely regarded to have been quite arid due to the amount of evaporites formed. The tropics, where Haynesville deposition occurred, of the Jurassic may have been subject to Milankovitch cycling on a large scale (Sellwood et al. 2000).

Jenkyns et al., (2002) refined chemostratigraphy from Britain and Europe during the Jurassic to show variances in the paleoceanography during that time.

During the Jurassic favorable organic-carbon flux conditions existed on the ocean floor. This flux has a direct correlation to the planktonic productivity in the region and the Jurassic has markedly high peaks of this productivity (Jenkyns et al. 2002). Although Kimmeridgian organic-rich facies are common globally, there has not been success in implementing high-resolution biostratigraphy outside of the British region. Despite multiple restricted basins existing during the Kimmeridgian there has been no evidence found for a global Oceanic Anoxic Event (OAE) during this time (Jenkyns et al. 2002). The Early Torcian, about 30 Ma prior to the Kimmeridgian, saw high amounts of organic-carbon deposition and mass extinction and has been determined to be an OAE (Hesselbo et al. 2000). Further studies may prove that an OAE had occurred during deposition of the Haynesville.

The Jurassic experienced many global eustatic sea level events, but the general trend up to the early Kimmeridgian was a transgression. Marine facies from the North Sea region show sea level changes independent of regional tectonics and change in sedimentation rates (Hallam 1978). The global rise in sea level during this time is generally linked to an increase in ocean ridge spreading. Evidence for a Middle Oxfordian transgression has been seen off the west coast of Morocco as well as the Gulf of Mexico, and a Kimmeridgian transgression is noted from regions of Ethiopia and Azerbaijan. This trend of transgressions starting in the Early Jurassic and ending in the Kimmeridgian has been shown to be episodic and not a gradual rise (Hallam 1978).

Stratigraphic sequences and lithologies in the Haynesville were greatly influenced by the pre-existing topography in the basin as well as sediment supply

(Cicero et al. 2010). This topography originated from the Smackover carbonates build-up and appears to be most influential along the north side of the basin. The pre-Haynesville paleogeography also impacted the organic richness of the formation. The transgressive-regressive duality of the Haynesville complicates defining stratigraphy as you move away from the deepest part of the basin. Retrogradation occurred in the western part of the basin as carbonates on the East Texas Salt Basin backstepped throughout the Kimmeridgian. Prograding on the eastern part of the basin came from the influx of clastics via the Ancestral Mississippi River (Cicero et al. 2010). A maximum flooding surface (mfs) is interpreted to have occurred in between Haynesville and Bossier time (Figure 1B), which correlates to an observed time of sea level regression. Prograding conditions at this time resulted in an increase in deltaic siliciclastics. The East Texas Salt Basin has Haynesville carbonates that indicate a pattern of reef growth in a coarsening upward profile. The shale facies from the central part of the basin also show a coarsening upward profile in many areas (Cicero et al. 2010). The Gilmer Ridge, trending N-S, separates the East Texas Salt Basin and the Haynesville basin. The ridge is difficult to interpret stratigraphically due to the transgressive-regressive nature of the system. Along its western border the ridge has shelf carbonate build-up and time equivalent shale was deposited along the eastern border (Cicero et al. 2010).

One seismic stratigraphic interpretation indicates the Haynesville timelines to have cut through structural highs in the region instead of truncating against the highs (Cicero et al. 2010). Some local structural highs were likely present to restrict the flow within the basin but at this time the exact basin structure is unknown (Cicero et

al. 2010). Sequence stratigraphy in the basin becomes increasingly complex as you move outward from the central deepest part of the basin. The backstepping carbonates to the west and prograding siliciclastics to the east create opposing stacking sequence patterns and thus diachronous maximum flooding surfaces. Stratigraphically the Haynesville is divided into Lower and Upper sections (Cicero et al. 2010). Also included is the Lower Bossier subdivision because historically the Bossier Shale included most all of what is now called the Haynesville Shale (Figure 1B).

Lower Haynesville

The ancestral Mississippi River was increasing in competence during the deposition of the Smackover and this trend continued into the Lower Haynesville. Deep basin subsidence was minimal and the effusive nature of the river created progradational sequences. A maximum flooding surface for the Lower Haynesville may lie on top of Smackover carbonates (Cicero et al. 2010). The Lower Haynesville shows the clearest distinction in the basin between the carbonates and the clastics due to their division by structural highs. Geochemical studies have shown that the Lower Haynesville was formed in the most anoxic conditions compared to the Upper Haynesville and Bossier Shales (Buller and Dix 2009; Dix et al. 2010).

Upper Haynesville

As an overall transgression continues, the amount of shallow marine carbonates increased and evaporites decreased as marine waters cover arid areas along the basin's rim (Cicero et al. 2010). The east portion of the basin is mainly carbonates grading into shales, while the Ancestral Mississippi continued to bring

more clastics into the basin. Multiple structural highs were continuing to restrict flow into the basin, including a few now subaqueous island complexes (Cicero et al. 2010; personal correspondence Dr. Sommer). The top of the Upper Haynesville marks a major flooding surface switching from a Transgressive Systems Tract to a Highstand Systems Tract (Figure 1B).

Lower Bossier

The progradational deposits from the HST during the Lower Bossier show a pattern of shale coarsening up to sand with carbonates at the top (Goldhammer and Johnson 2001; Norwood and Britton 2001). This progradational pattern continued into the deposition of the Cotton Valley sands that overlie the Haynesville/Bossier shales. As influx from the Ancestral Mississippi increased during this time the transition zone from clastics to carbonates moved farther west as clastic input prograded into the basin. Although shale is widespread during the Lower Bossier deposition, the TOC shows a decreasing pattern perhaps because effluent of clastics was so high during this time (Cicero et al. 2010).

2.1 Black Shale Diagenesis

The study of black shale diagenesis and their economic value is not a new venture. Tourtelot (1979) pointed out "increasing attention will be given to this possibility as demands increase and supplies from conventional sources dwindle". It is important to note that the geologic setting is not the biggest factor in the preservation of organic-rich shale. Amount of oxygen, sedimentation rates, and organic productivity are more critical controlling factors (Tourtelot 1979).

Diagenetically some key factors for organic preservation include sulphate-rich waters, organically rich sediment at the sediment/water interface, and sedimentation rates that are not too slow but not too fast (Curtis 1980). The Haynesville Shale falls into the model Tourtelot calls the 'restricted circulation model', where there is a lack of circulation in the water column creating an anoxic environment. Organic rich shales can be deposited in an 'open ocean model' in which sedimentation rates of organic matter are so rapid that they escape the photic zone and reach bottom waters without complete oxidation occurring. Figure 1 shows a paleogeographic map of the Ancient Gulf of Mexico where local highs effectively block major ocean circulation from occurring and oxidizing organic matter.

Tourtelot (1979) and Curtis (1980) both presented models of diagenetic zones of alteration (Figure 2). The amount of time sediment and organic matter reside in each zone plays a large role in the ultimate preservation of organic-rich sediment. Tourtelot presents a general equation showing how diagenesis impacts this preservation (Figure 3).

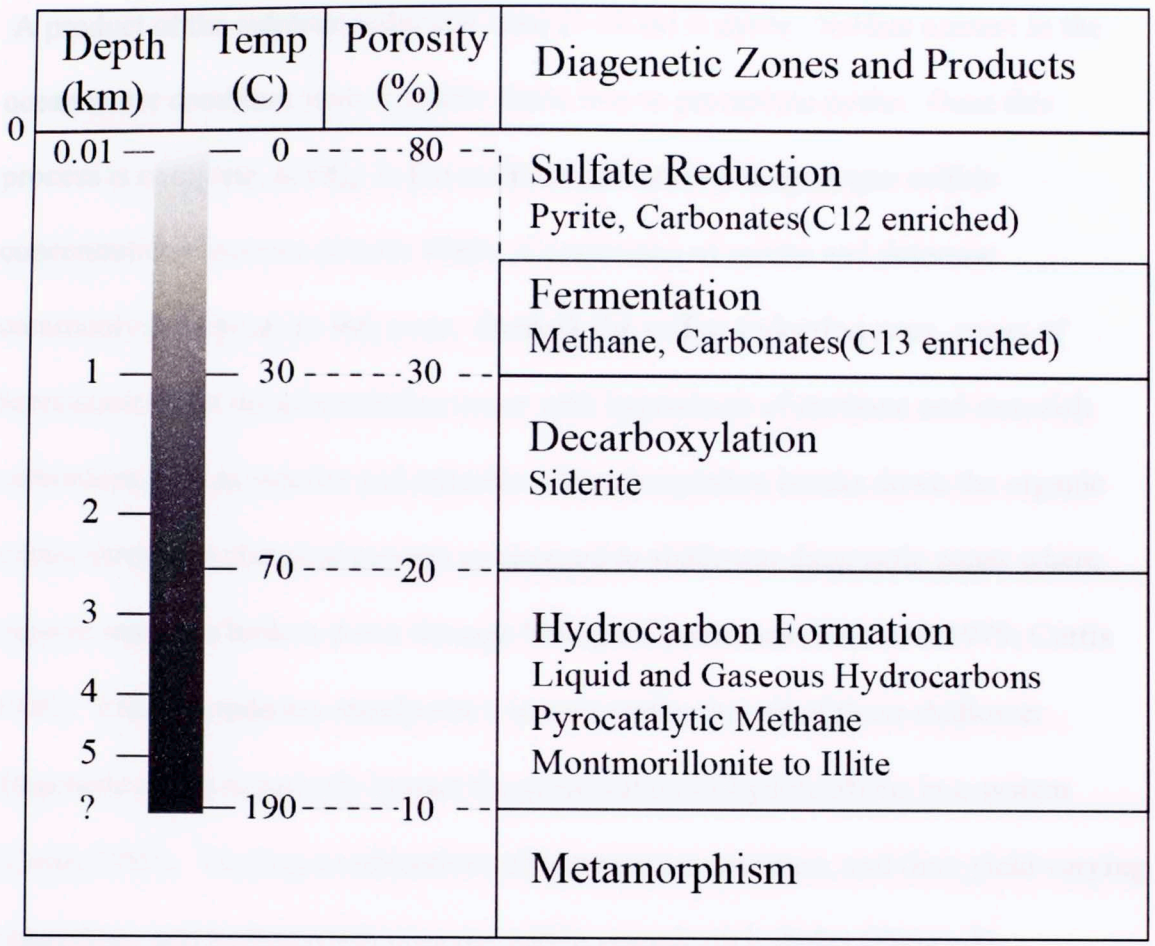

Figure 2: Common zones of diagenesis within organic rich shales from shallow burial to the zone of metamorphism. Modified from Tourtelot's diagenetic zones (1979).

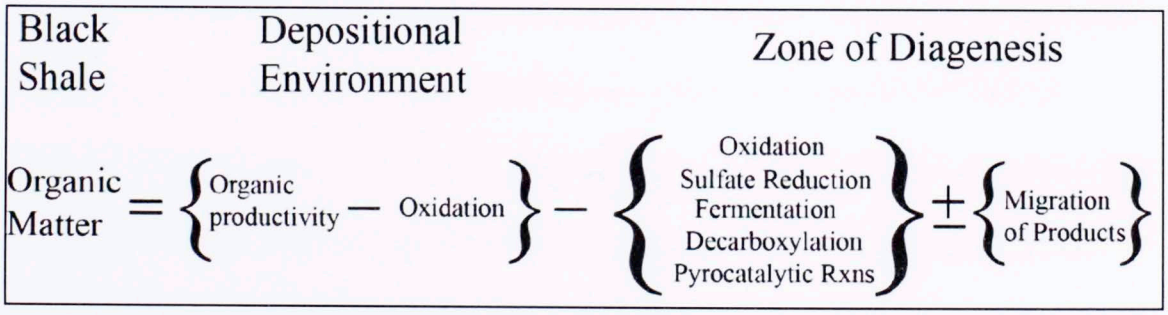

Figure 3: Generalized equation showing how depositional environment and diagenesis either positively or negatively effect amount of preserved organic matter in black shales. Modified from Tourtelot's equation (1979).

A product of the sulphate reduction zone (1-10 m) is pyrite. Sulfate content in the ocean water combines with available ferric iron to precipitate pyrite. Once this process is complete, acidity in the sediment increases and hydrogen sulfide concentrations increase (Curtis 1980). Concretions of calcite and dolomite commonly precipitate in this zone. Beneath the sulfate reduction zone, zones of fermentation and decarboxylation occur with byproducts of methane and iron-rich carbonates such as siderite and ankerite. Decarboxylation breaks down the organic matter through a chemical process as opposed to shallower diagenetic zones where organic matter is broken down through biological processes (Tourtelot 1979; Curtis 1980). From an industry standpoint it is noteworthy that all of these shallower diagenetic zones negatively impact the preservation of hydrocarbons in a system (Curtis 1980). Varying combinations of temperature, pressure, and time yield varying mineralogy and hydrocarbon reserves within organic-rich shales (Figure 3).

3. Methods

3.1 Petrographic Procedures

The unoriented Coleman Gas Unit 1-6 core was described noting the facies, lithologies, structures, and diagenetic features (Appendix A). Because the Snider A1-H core is highly fractured and rubbled a generalized core description was pieced together relying solely on thin sections and core photos (Appendix B). The Snider A1-H core is a 369.4 ft. interval and the Coleman Gas Unit 1-6 core is 318.5 ft. in length. Dunham's (1962) classification was used to differentiate the facies within the Haynesville.

Thin sections from each core were described using a Nikon Optiphot-Pol polarizing light microscope at the University of Oklahoma. Two criteria were used in selecting samples for thin sections - general facies within the core and samples with veins (vertical and horizontal) and breccias. The veined and/or brecciated zones were targeted to look for diagenetic features. Individual paragenetic sequences were completed on thin sections based on textural relationships between phases. Thirty-nine thin sections were analyzed from the Snider A1-H core. Of the thirty-nine, nine thin sections were sampled to analyze facies and thirty were sampled to look at diagenetic features from veins and one brecciated zone. From the Coleman Gas Unit 1-6, thirty-six thin sections were created with eight chosen for facies analysis and twenty-eight selected for analyzing veins and one breccia. Thin sections with opaques were examined using a Nikon Labophot2-Pol with MKII Fiber Optic Light reflected light microscope to identify mineralogy. Specific samples were selected and

stained with alizarin red to differentiate between calcite and dolomite within veined and brecciated zones.

Nine thin sections from the cores were analyzed using a FEI Quanta 200 environmental scanning electron microprobe equipped with an Oxford Instruments X-act using Energy Dispersive Spectroscopy system at the University of Oklahoma in the Mewbourne College of Earth and Energy IC^3 laboratory. These were selected in order to look for key diagenetic features, to determine exact mineralogy in veins, and to look for the magnetic carrier mineral. Energy dispersive x-ray analysis (EDXA) was used for qualitative elemental analysis on unknown minerals. All petrographic procedures were utilized in interpreting a paragenetic sequence of each core and to interpret the paragenesis of the Haynesville Shale in Harrison County.

3.2 Paleomagnetic Procedures

Standard 1" diameter plugs were taken from each core and used for paleomagnetic analyses. A five-foot spacing interval was used for sampling except where highly veined or brecciated zones were present. In these veined/brecciated zones plugs were sampled from within the zone and also above and below in order to test if remagnetizing fluids were associated with a specific interval and fluid event. A high-density sampling was also taken from a known productive (gas) interval in the Snider A1-H core. From the total 369.4 ft. core interval of the Snider A1-H core, eighty-four plugs were drilled. Twenty of these plugs were drilled at the Oklahoma Petroleum Information Center (OPIC) using a water-cooled, variable speed drill press with a non-magnetic bit in Norman, OK; the rest were drilled at Sarkeys Energy

Center at the University of Oklahoma. All sixty-one plugs sampled from the Coleman Gas Unit 1-6 were drilled at the University of Oklahoma.

Plugs were drilled from the side of the 'butt' of each core enabling the extraction of longer plugs and multiple specimens from one depth (Figure 4). Each plug was then cut down to a standard 2.2 cm length specimen to be used for paleomagnetic and rock magnetic analyses. Cutting was done using an ASC Scientific dual blade saw.

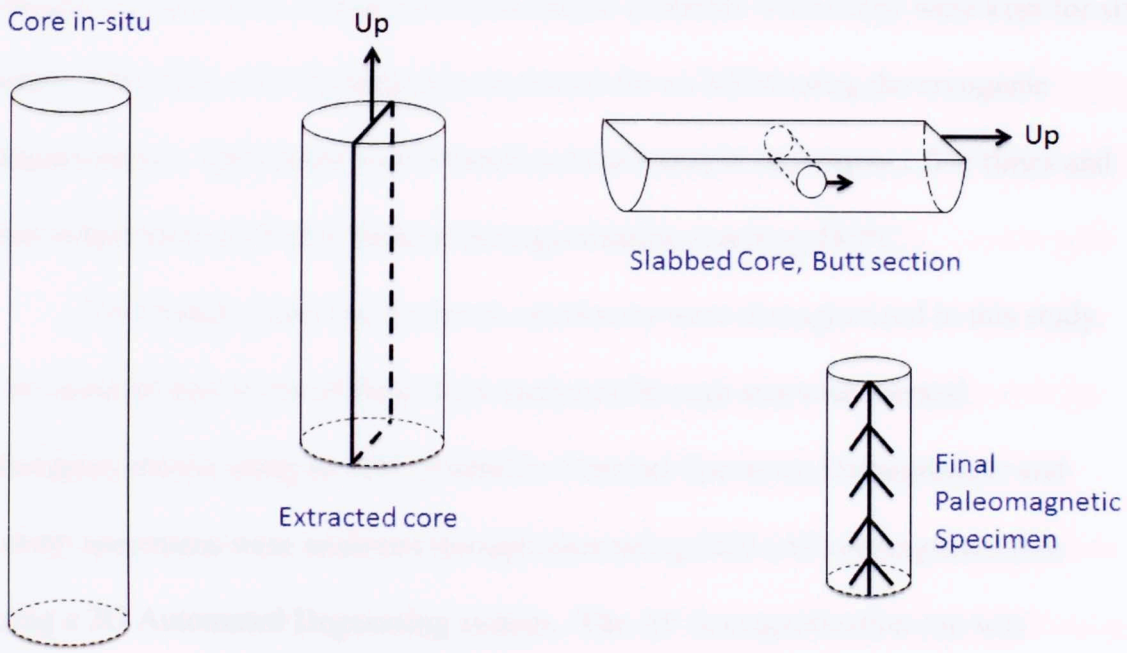

Figure 4: Paleomagnetic plug sampling method used on Snider A1-H and Coleman Gas Unit 1-6 cores. Diagram starts with core extraction (left), on to slabbing and finally plug extraction performed at the University of Oklahoma. Arrows on final paleomagnetic specimen drawn coming out of core and the line was drawn on the 'Up' direction of the plug.

Once samples were cut to standard lengths they were weighed and an Agico Multi-function Kappabridge mass magnetic susceptibility meter was used to attain bulk susceptibility. A 2G-Enterprise cryogenic magnetometer with DC squids was used to measure the natural remanent magentizations (NRM) in the specimens. The measurements were completed in a magnetically shielded paleomagnetic laboratory at the University of Oklahoma.

Low-temperature demagnetization (LTD) was completed on 52 specimens from the Snider A1-H core. This was done using 'B' specimens (specimens which had a matching depth specimen) to analyze if LTD had an impact on VRM and ChRM components (Dunlap and Argyle 1991). Specimens were submerged in liquid nitrogen and placed in a triple-shield mu-metal container where they were kept for six hours. Then they were immediately measured for an NRM using the cryogenic magnetometer. Specimens were treated and measured in this manner five times and then subjected to a 23-step thermal demagnetization reaching 480°C.

Two hundred and twenty-seven specimens were demagnetized in this study. Two hundred and seven of these were analyzed through stepwise thermal demagnetizations using an ASC Scientific Thermal Specimen Demagnetizer and twenty specimens were analyzed through alternating field (AF) demagnetization using a 2G Automated Degaussing system. The AF demagnetization run was performed by exposing samples up to a 100 mT (millitesla) alternating field (5 mT steps to 40 mT and then 10 mT steps to 100 mT) and then measuring their magnetizations with the cryogenic magnetometer. Stepwise thermal demagnetization was done initially in 18 steps from 100°C to 520°C. After one run was completed

more steps were added to refine a potential viscous remanent magnetization (VRM) and stepwise thermal demagnetization was performed in 23 steps from 40°C to 480°C.

Super IAPD2000 software was used to analyze all demagnetization data. Remanent magnetization components were picked where four linear points with a mean angle deviation (MAD) less than 15° were present. Fisher (1953) statistics were utilized once components had been picked.

The purpose in acquiring a VRM (low-temperature component) from the cores was to attempt to orient each core. Orientation of a core can be done by rotating stable VRM components to the modern day magnetic declination for Harrison County (e.g., Van der Voo and Watts 1978; Suk et al. 1990; Van Alstine and Butterworth 2002; Dennie et al. 2012). Having an oriented core is necessary to determine the age of the magnetizations using the characteristic remanent magnetizations (ChRM). The poles corresponding to the ChRM are then plotted on an apparent polar wander path (APWP).

Isothermal remanent magnetization (IRM) acquisition was completed in the paleomagnetics laboratory at the University of Oklahoma. This technique was utilized to acquire bulk magnetic mineralogy in the specimens. Five specimens were chosen from each core for analysis. Specimens were exposed to a 120mT-alternating field using a 2G Automated Degaussing system and measured; then they were given an IRM through 25 steps ranging from 10-2500mT using an ASC Scientific Impulse Magnetizer. Three perpendicular (x,y,z) IRMs were then set at 120mT, 500mT, and 2500mT respectively. After IRMs were imparted a stepwise thermal demagnetization

was completed on the specimens. IRM data acquired were analyzed using coercivity spectrum analysis to determine magnetic mineralogy present (Heslop et al. 2004; Kruiver et al. 2001).

3.3 Geochemical Procedures

Six samples were selected and prepared for strontium isotope ($^{87}Sr/^{86}Sr$) analysis, to aid in determining if fluids originated within the system or were derived from external sources. Samples were chosen based upon key veined and brecciated zones from each core. Five of the samples were from the Snider A1-H core with one sample coming from the brecciated zone in the Coleman Gas Unit 1-6 core. Veins were drilled and powdered (minimum 0.1 grams) at the University of Oklahoma and sent to the University of Texas in Austin for analysis. Powders were first rinsed in 0.5M ammonium acetate and then dissolved in acetic acid (4%) for ten minutes. Redissolving powders in nitric acid then destroyed acetic acid prior to isolating strontium in 3 N nitric acid. Strontium was then further isolated by ion exchange chromatography using Sr SPEC resin. Samples were then loaded onto Re filaments with tantalum oxide slurry and phosphoric acid and run on a Triton TIMS. The NIST SRM for experiments was 0.710276 ± 0.000013 (n=160).

4. Results and Interpretations

4.1 Facies

Facies within both cores were identified through visual inspection of the core slabs, thin section analysis, and SEM analysis. The cores can be split into five facies- a siliceous mudstone, a laminated siliceous mudstone, a carbonate-rich mudstone, a burrowed mudstone, and a dolostone. Distinguishing between the siliceous and the carbonate-rich mudstones was done relying upon thin section analysis, thus facies changes in core descriptions are noted only in places where thin sections confirmed this change. XRD analysis (Core Lab via GMXR) on the Snider A1-H core yields an average mineralogical breakdown of the Haynesville as 37% quartz, 26% clays, 8% plagioclase, 12% calcite, 9% dolomite, and 2% pyrite.

Siliceous Mudstone

The most prevalent within both cores, this facies consists of clays, silica grains, and minor allochems commonly filled with calcite. Calcite cementation of mudstones throughout the Haynesville is prevalent (Hammes et al. 2011) and is found in the Snider A1-H and Coleman Gas Unit 1-6 mudstones. In the Coleman core small silica filled veins are commonly associated with this facies as are shell fragments replaced by calcite. This facies in the Snider A1-H core contain healed fractures (Figure 5A) composed of dolomite and calcite.

Laminated Siliceous Mudstone

Compositionally the laminated siliceous mudstone is identical to the siliceous mudstone facies (clays, silica grains, and minor allochems), its variance is in its higher fissility alone. The laminated facies was identified through core description

and then subsequently called siliceous based upon thin section analysis. An interval in the Coleman Gas Unit 1-6 core from ~11,066 to 11,090 fits this facies description but also has a large number of burrows present and could be classified as a highly laminated burrowed siliceous mudstone. Only a very small interval within the Snider A1-H core is laminated although some horizontally filled fractures may have formed along fissile bedding planes. These were not described as laminated.

Carbonate-rich Mudstone

The carbonate-rich mudstone facies is composed of clays, carbonate grains, allochems and in some areas minor detrital quartz grains (Figure 5B). Carbonate-rich mudstones within the Haynesville may be associated with proximity to Smackover carbonate platforms (Hammes et al. 2011); carbonate grains are interpreted as detrital. Compositionally the carbonate-rich mudstone in the Coleman Gas Unit 1-6 core has similar clay percentages to the siliceous mudstone facies. This facies is only seen in the Coleman core as detrital carbonate and in the Snider core is only seen in a few thin sections. This may suggest that the Coleman Gas Unit 1-6 was more proximal to a carbonate platform during deposition. Bivalve shell fragments and intact brachiopods were seen in thin section associated in this facies. SEM analysis revealed the presence of barite and albite in a breccia (Figure 5C) within this facies. Very few healed fractures are associated with this facies.

Burrowed Mudstone

The burrowed mudstone facies is composed of clays and varying amounts detrital quartz and carbonate grains with the burrows filled with micrite. This facies grades into the other facies and is difficult to pinpoint when it begins and where it

ends due to its identification being tied to thin section analysis. Thin sections from the Coleman core represent its largest interval going from approximately 11,060' to 11,114'. Small horizontal silica veins are common within the matrix and burrows are filled with micrite (Figure 5D). Sphalerite, dolomite, calcite, and pyrite have all been identified within vertical veins of the facies. Sphalerite, calcite, and pyrite also are observed to replace shell fragments. A few thin sections show dark lenticular lenses than run along bedding planes. These are also interpreted as burrows although they may be clay flocculation clasts (Boggs 1987).

Dolostone

This facies is only present as a small one-foot bed within the Snider A1-H core. Double terminating quartz grains are present within the facies and are readily visible in thin section. Apatite and leucoxene were also observed in SEM analysis (Figure 5E).

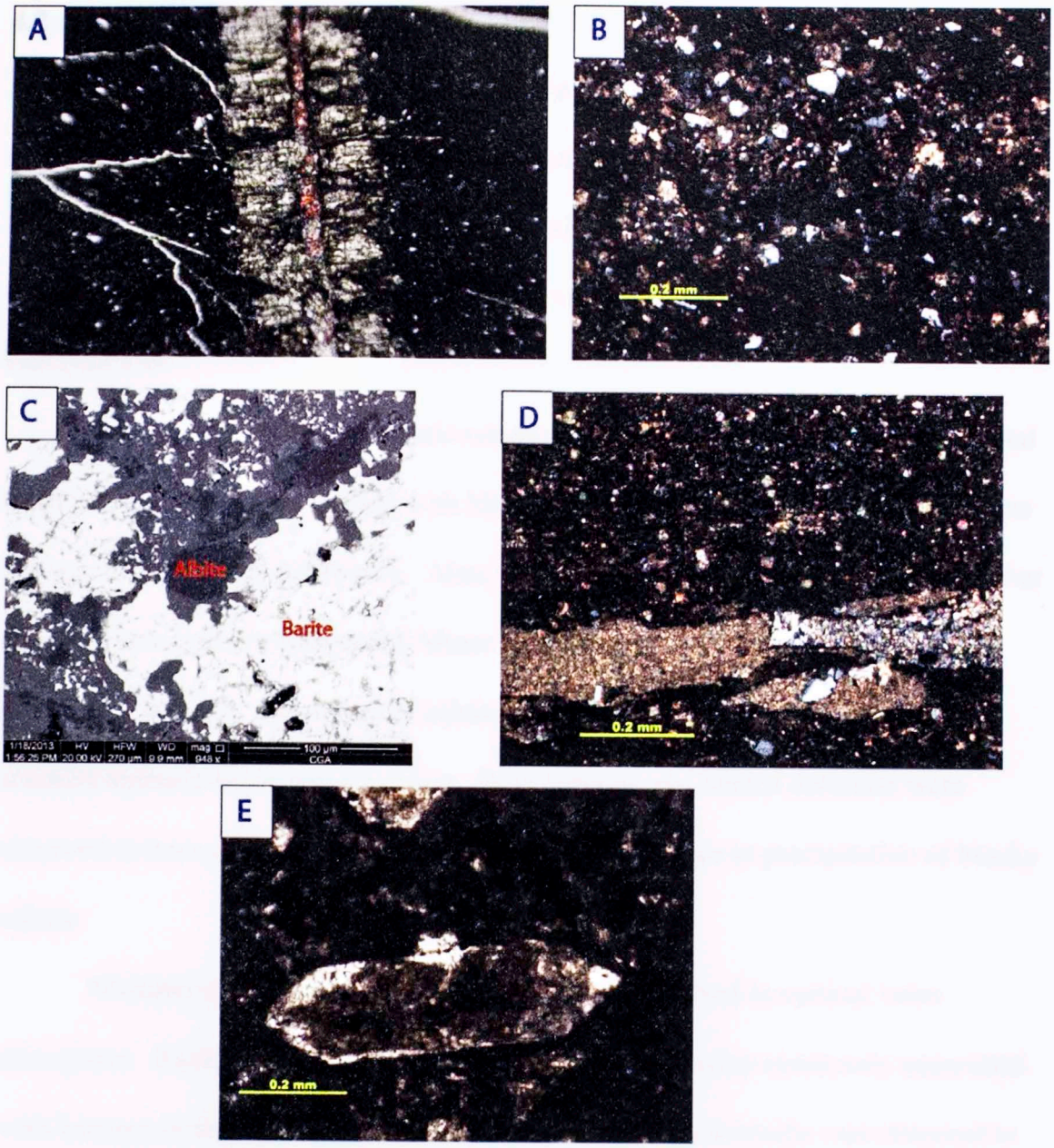

Figure 5: (A) Vertical vein in siliceous mudstone facies. Stained with alizarin red to show calcite versus dolomite. (B) Mudstone facies showing both quartz and calcite detrital grains. (C) SEM backscatter electron image from a breccia in the carbonate-rich mudstone facies in Coleman core where barite and albite were identified through electron dispersive x-ray analysis (EDXA). (D) Burrowed mudstone facies in Snider core. Burrow filled with micrite and partially replaced by blockier calcite. (E) Dolostone facies has double terminated quartz grains present.

4.2 Diagenesis and Paragenesis

Micritization was found in burrows alone and is, thus, interpreted as an early diagenetic event. Two stages of pyritization are identified; the early stage has pyrite forming within the matrix of the mudstones while the later occurs as a replacement of calcite and dolomite in veins (horizontal and vertical) as well as shells in the Coleman Gas Unit 1-6.

Two cross-cutting vein relationships were observed in both cores. Horizontal lenticular veins commonly filled with bladed dolomite are cross-cut by vertical veins throughout the Snider A1-H core. Also, small silica healed veins cross-cut both other common vein types in both cores. Mineralization within horizontal veins is interpreted as early. Two types of calcite replacement occurred in allochems as solution reprecipitation and inversion. Both baroque and bladed dolomite were observed to have occurred after these calcite types but prior to precipitation of blocky calcite.

Multiple stages of calcite precipitation were observed in vertical veins throughout. Radial calcite was observed on the edges of veins commonly associated with baroque dolomite in the middle of the veins. Bladed dolomite was observed to have precipitated after baroque dolomite but prior to a sparry calcite (Figure 5A). Sulfate and sulfide minerals were also observed in vertical veins under transmitted and scanning electron microscopy (Figure 6A and B). Barite and anhydrite are present in the middle of veins with calcite on the rims. Sphalerite occurs both outside and inside of veins and as a replacement for calcite within shell fragments (Figure 6C and D). Plagioclase laths were discovered under the SEM and are interpreted to have

occurred after dolomite precipitation and either prior to or contemporaneously with the last stage of calcite precipitation within the vertical veins (Figure 6E).

Diagenetic events relating to allochem replacement cannot be compared to veins in the cores due to a lack of cross-cutting relationships. One common link between veins and allochems is radial calcite; this alone does not provide a strong enough relationship to merit placing precipitation of all replaced allochem minerals in the same window as precipitation of radial calcite within the veins. This is due to interpretation that the Haynesville had multiple precipitation events of radial calcite (Figure 7A). Three stages of calcite were observed within allochems in the Coleman Gas Unit 1-6 core. Radial calcite occurred on edges of allochems while a drusy mosaic calcite, common to burial diagenesis, or an impunctate structural calcite is found in the middle of allochems.

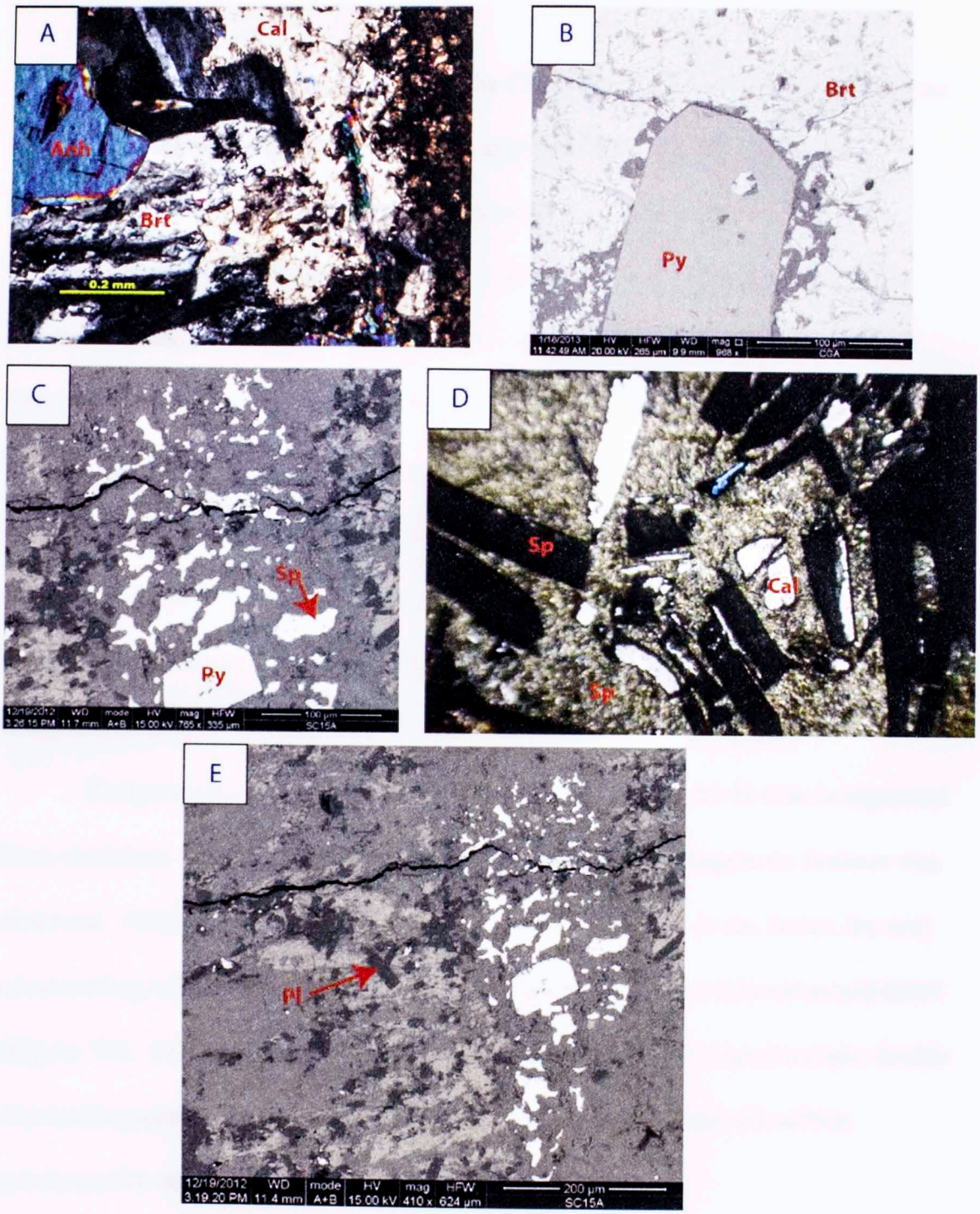

Figure 6: (A) Transmitting microscope photo in CPO showing brecciated zone and presence of calcite, barite and anhydrite. (B) SEM backscatter electron image showing barite, calcite and pyrite in Coleman breccia. (C) SEM backscatter image showing sulfur rich minerals within a calcite vertical healed fracture. (D) Transmitting microscope photo showing sphalerite replacement of allochems that had been precipitated with calcite. (E) SEM backscatter electron image from same vein as 'C', arrow points to plagioclase found within dolomite rich edge of fracture.

Each core has a brecciated zone; the Coleman Gas Unit 1-6 zone is less than half a foot thick while the Snider A1-H is approximately two feet in length. Brecciation is interpreted as a diagenetic process based upon hand specimen identification showing shale clasts within a sulfate rich matrix (Figure 7B). Sub-parallel veining is associated with the Snider A1-H brecciation and is, therefore, interpreted to have occurred contemporaneously with vertical veining. The Coleman brecciation cannot be relatively timed with other diagenetic events and mineralization in the cores. Paragenesis of the Snider A1-H breccia consists of three minerals; anhydrite followed by calcite and lastly celestite. The Coleman Gas Unit 1-6 breccia paragenesis consists of four minerals; first, barite followed by albite and celestite and lastly calcite (Figure 7C and D).

Paragenesis of the dolostone facies within the Snider A1-H core is separated from mudstone facies as no correlation of mineralization or diagenetic features was observed. Although six minerals were identified in the SEM in the facies, the only cross-cutting relationship observed placed dolomite as the first mineral precipitated (Figure 7E). Other minerals observed that cannot be relatively dated include double terminating quartz, apatite, pyrite, leucoxene, and a cooper-iron rich sulfide (chalcopyrite or bornite).

Figure 8 combines all paragenesis of the Snider A1-H and Coleman Gas Unit 1-6 cores from early to late diagenetic stages.

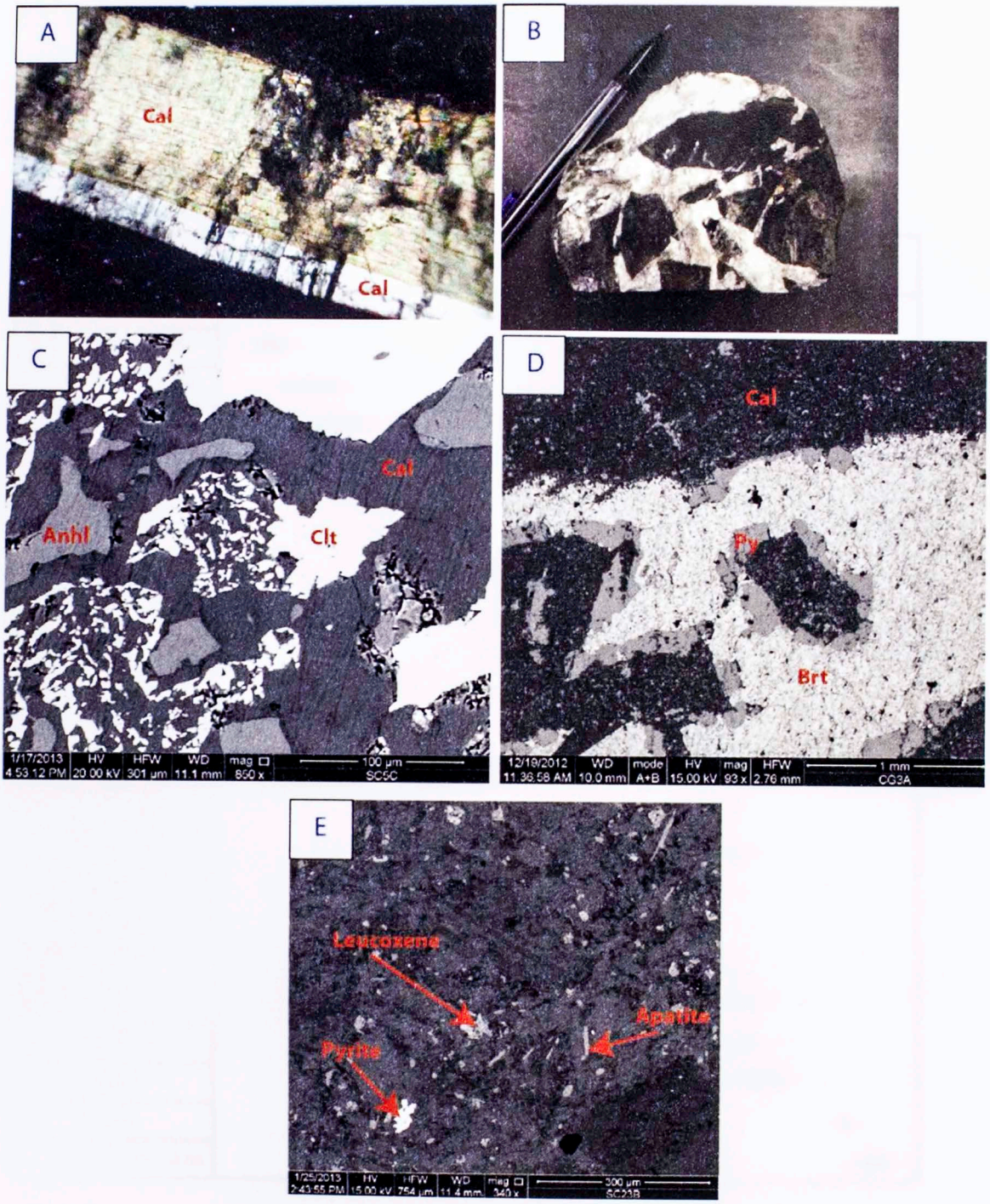

Figure 7: (A) Transmitting microscope photo in CPO showing multiple stages of calcite precipitation. (B) Coleman Gas Unit 1-6 breccia shows complete angular shale clasts held within barite and fracture propagation indicates brecciation from overpressure. (C) SEM backscatter electron image of sulfur rich minerals alongside calcite precipitation from Snider A1-H breccia. (D) SEM backscatter electron image of barite, calcite and pyrite in Coleman brecciated zone. (E) SEM backscatter electron image from dolostone interval in Snider A1-H core with arrows showing presence of apatite, leucoxene and pyrite identified through electron dispersive x-ray analysis (EDXA).

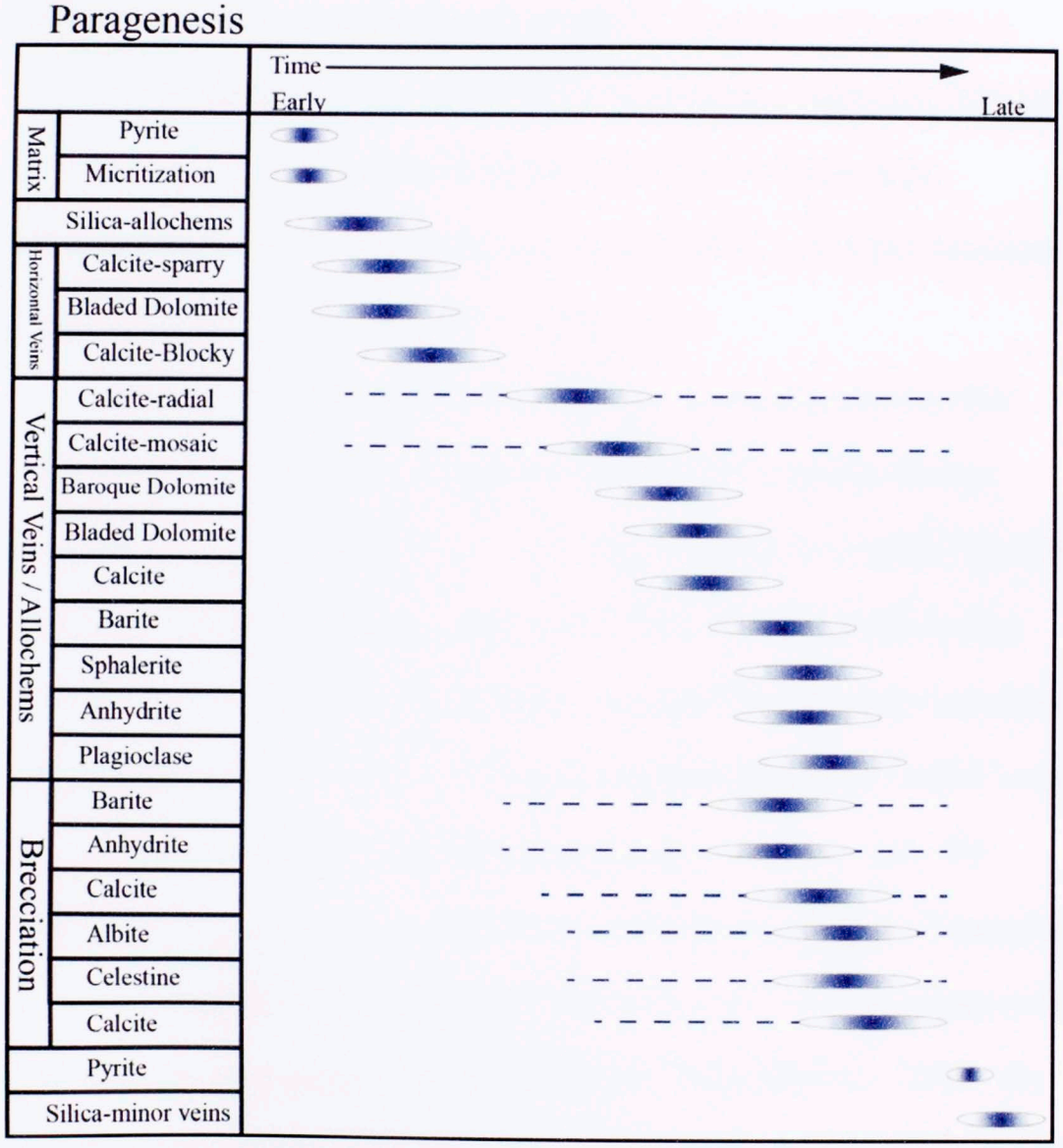

Figure 8: Paragenetic sequence compiled from the Snider A1-H and Coleman Gas Unit 1-6 cores. Figure shows relative timing of mineralization moving from left (early) to right (late). Relative timing of matrix paragenesis, veins and brecciation goes from early (top) to late (bottom). Ellipses represent relative uncertainty moving from the center to edges. Dashed lines indicate uncertainty associated with specific textures or minerals. Brecciation likely occurred as a later stage when considering vertical fracture patterns observed within zone.

4.3 Paleomagnetism

Snider A1-H

Four different paleomagnetic techniques were utilized in testing the Snider A1-H core for stable magnetization(s). In all, 171 specimens were analyzed. Thermal demagnetization was completed on 94 specimens, alternating field (AF) demagnetization was run on 20 specimens, a five-step low-temperature demagnetization (LTD) was performed on 52 specimens, and isothermal remanent magnetization (IRM) was completed on 5 specimens.

Thermal demagnetization of the Snider A1-H samples removed three components, a low temperature component (NRM-100°C), an intermediate temperature component (160-320°C), and a higher temperature ChRM (300-480°C) (Figure 9). The low temperature component, VRM, was only picked in three specimens. The intermediate temperature component has an average inclination of 71° (standard deviation = 16.5; n = 90) and the higher temperature ChRM component has an average inclination of 52°(standard deviation = 16.6; n = 106). The intermediate temperature (IT) and ChRM were observed together in 55 specimens.

LTD treatments (five total steps) were performed to test the impact on the magnetization and to remove any contamination of the ChRM by a VRM. The average intensity change of the 52 specimens after two treatments was an increase of 0.4%. After the fifth treatment the total % change from the initially measured NRM was a decrease of 0.7%. Due to the small change associated with performing low-temperature analysis, this method was only used on these 52 specimens and not on any additional specimens. The LTD treatment did not change the direction of the

ChRM (Figure 10) or intermediate temperature component. Treatments did affect the unblocking temperature of the intermediate temperature component in some specimens, increasing from a maximum temperature of 260°C up to 320°C after LTD.

To test for a drilling-induced remanent magnetization (DIRM), three sites on the Snider A1-H core were subjected to Q-factor analysis (de Wall and Worm 2001). DIRMs commonly have steep inclinations of 70-90° (Burmester 1976; Jackson and Van der Voo 1985). Inner and outer specimens from one plug were cut to standard 2.2 cm length and NRMs and bulk susceptibilities were measured. Q-values (Q=NRM/(k*H)) were then compared, followed by calculating a percent change between inner and outer specimens. A DIRM will result in an elevated, up to 10-fold, measured remanent magnetization at the outer edge of the core (de Wall and Worm 2001). Very little change was recorded in the NRM (mean inner specimens = 10 mA/M, mean outer specimens = 9.9 mA/M) and susceptibility values (mean inner specimens = 1.49×10^{-7}, mean outer specimens = 1.47×10^{-7}) between the outer and inner specimens in the Snider A1-H. The average percent change of Q-values of only 0.63% increase likely rules out the possibility that the intermediate temperature component is a DIRM.

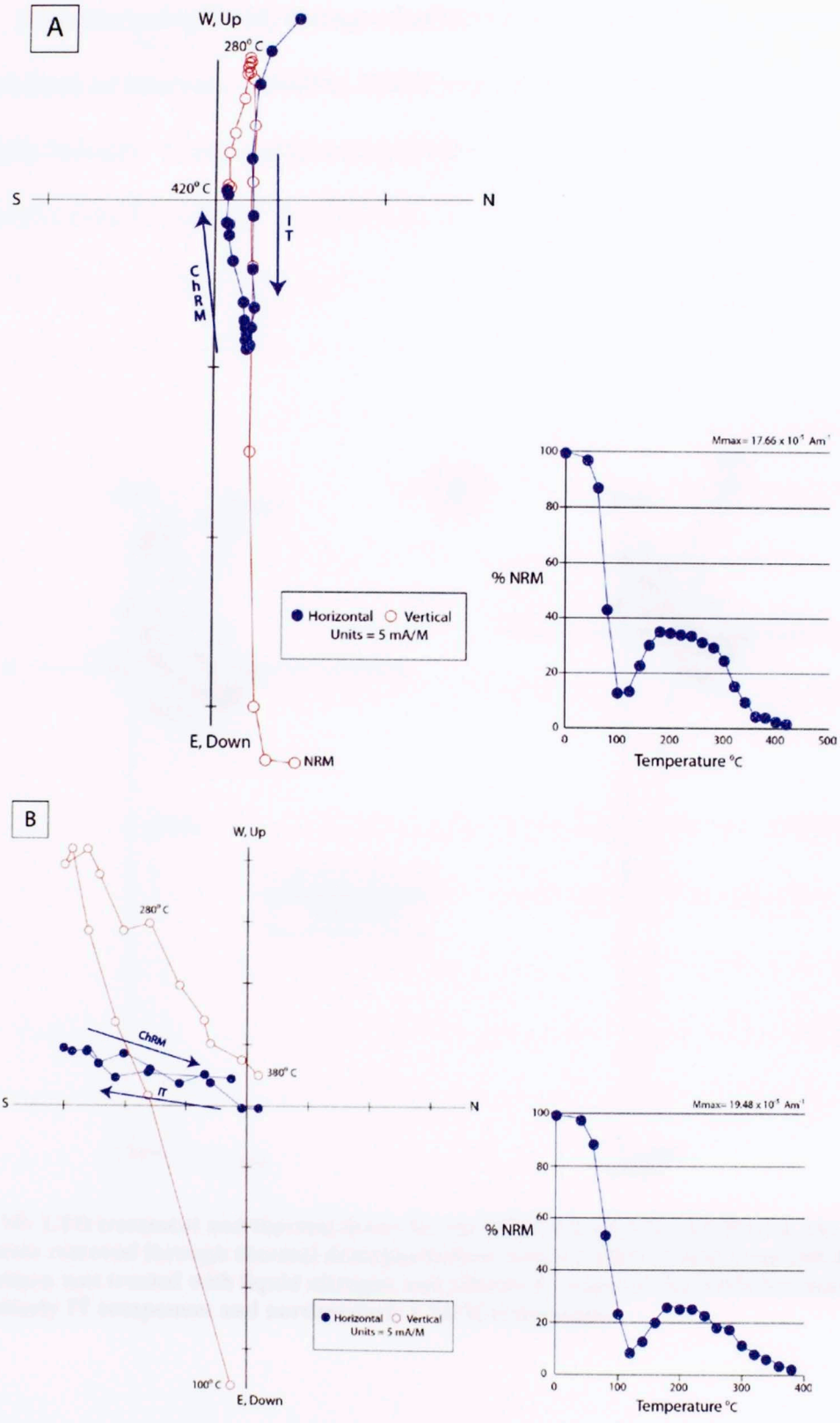

Figure 9: Representative Zijderveld diagrams and thermal decay curves of the Snider A1-H core. Notice that ChRM and IT(intermediate temperature component) vary in direction as picked in IAPD because the core is unoriented. A) Specimen depth = 10.378'6", B) Specimen depth = 10,381'2". Specimens demagnetized ~400°C.

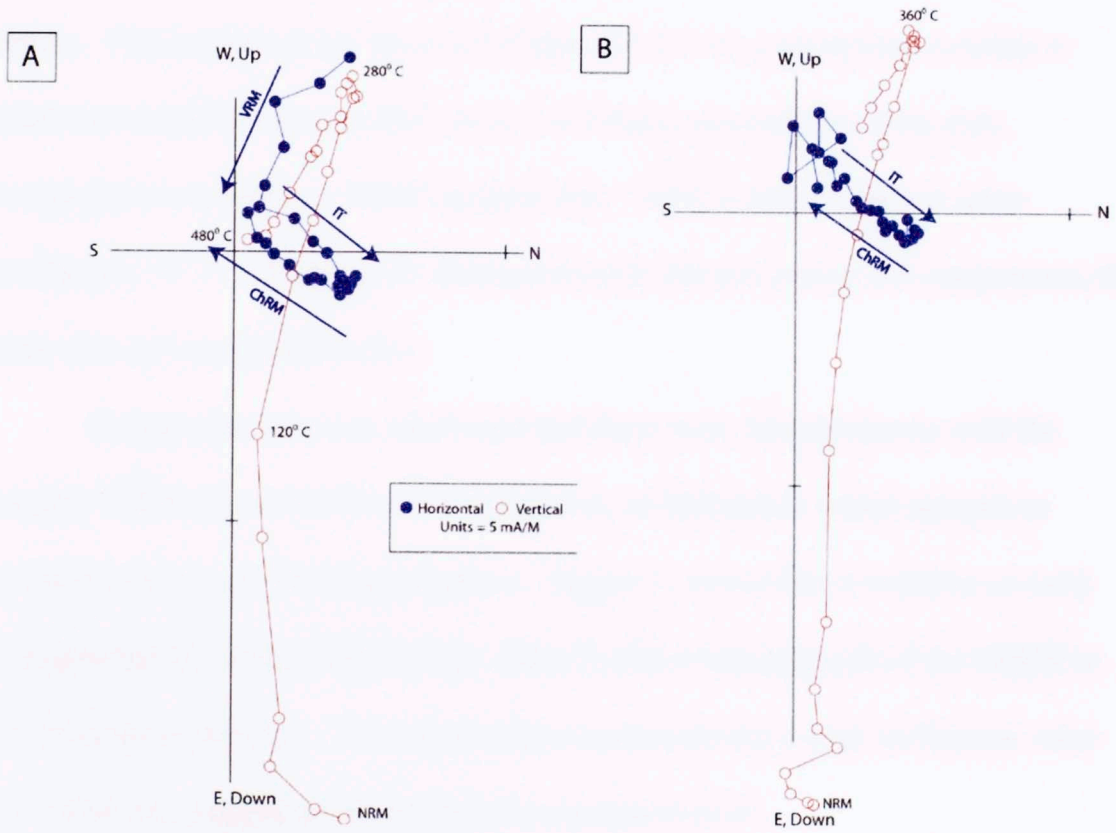

Figure 10: LTD treatment and thermal decay for the NRM from Snider A1-H core. (A) Three components removed through thermal demagnetization with a ChRM picked from 280-480°C. (B) Specimen was treated with liquid nitrogen and effectively removed the VRM but maintained southwesterly IT component and northeasterly ChRM component.

AF (Alternating Field) demagnetization was completed on 20 specimens selected from an interval (~10440 to 10461') that has been a target for horizontal drilling in industry. Components were picked for 19 of the 20 specimens after demagnetization (Figure 11). Curved trajectories on the Zijderveld diagrams indicate vector addition and that each component did not reach complete linear decay. AF demagnetization was not able to distinguish the intermediate and high temperature components observed in thermal demagnetization of specimens from same plug depths. Two groupings are observed (Figure 12) but these groupings correlate to depth and sampling that occurred along a similarly oriented side of the core. Components selected as a VRM (ranging from 25mT to 60 mT) show a steep inclination (77.3°). Because AF demagnetization did not resolve the components, the data were not considered further.

Because the core was unoriented and there were few specimens with the modern VRM, the inclinations were plotted on an inclination versus age plot to determine the age of the magnetizations. Figure 13 shows that it could be an early remagnetization around 150-140 Ma. There is also a reasonable fit of the ChRM to the Paleogene/Neogene. The intermediate component has a high inclination value (71°) that may suggest a Late Cretaceous remagnetization.

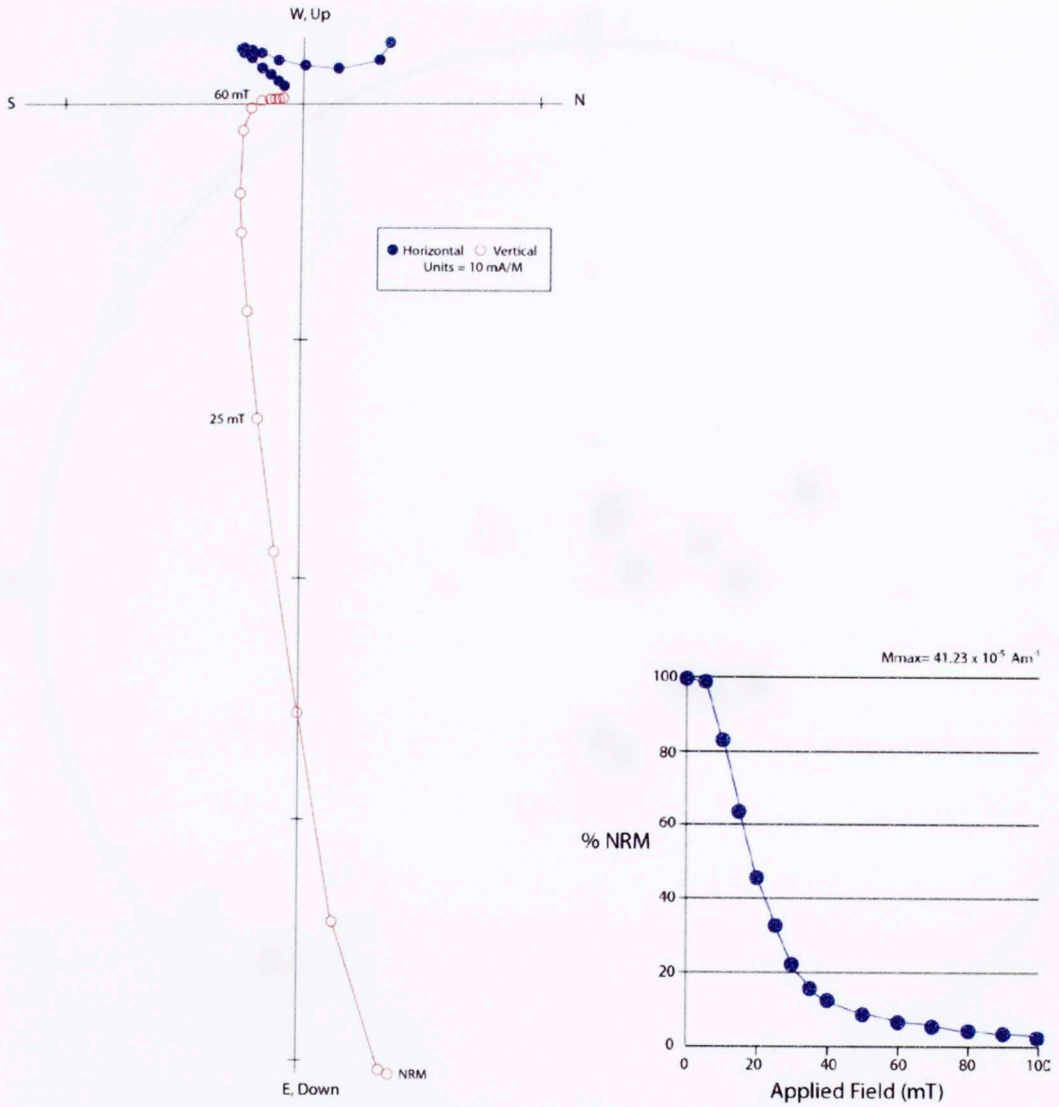

Figure 11: AF demagnetization done on 20 specimens from Snider A1-H core show smooth decay and possibly two components. Curvature associated with inclination may indicate vector addition.

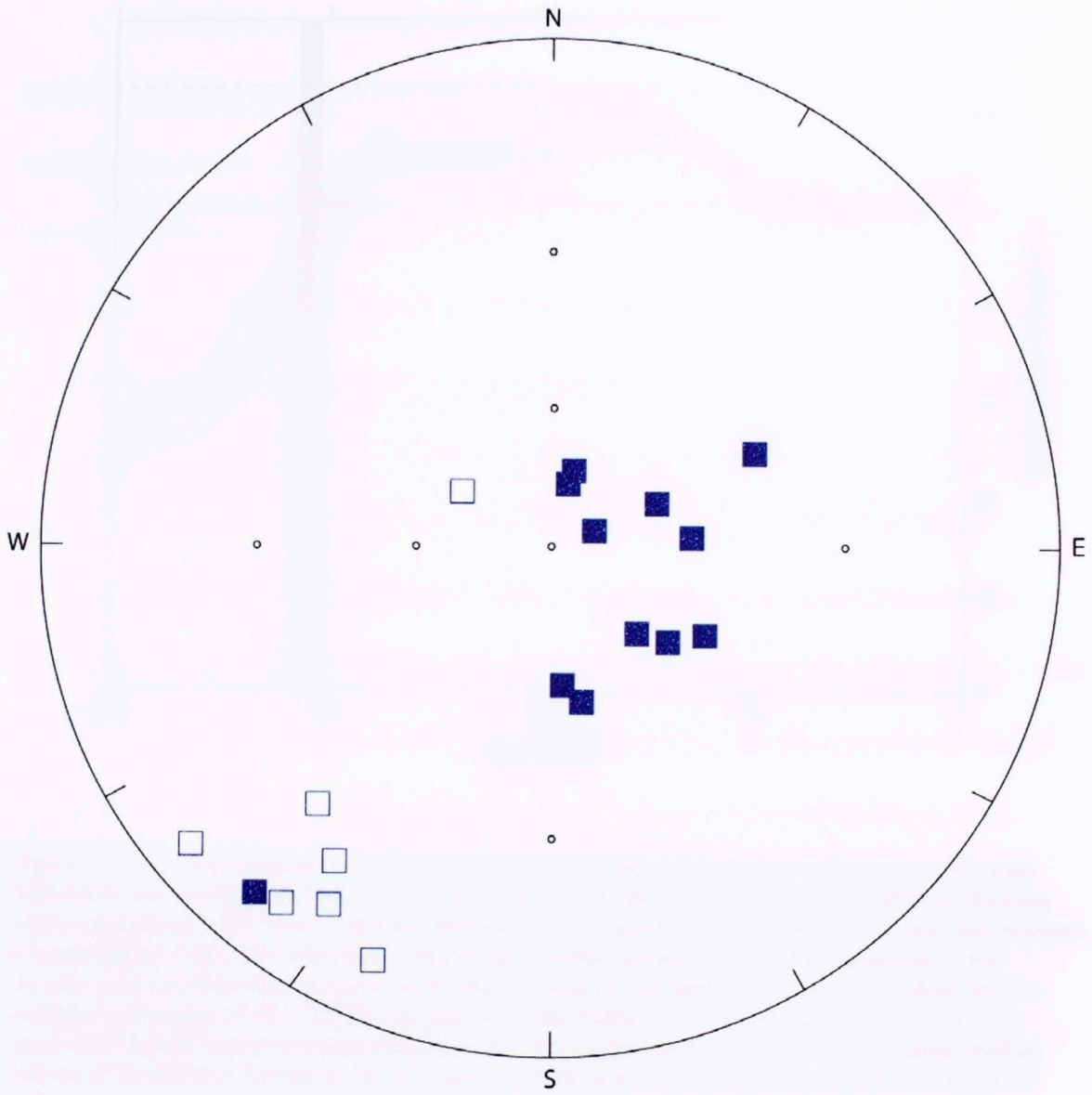

Figure 12: Stereoplot of ChRM components selected from AF demagnetization of the Snider A1-H specimens. Two groupings are observed but are artificial due to tight sampling on an unoriented core. Distinguishing between intermediate and high temperature components was not accomplished through use of AF demagnetization.

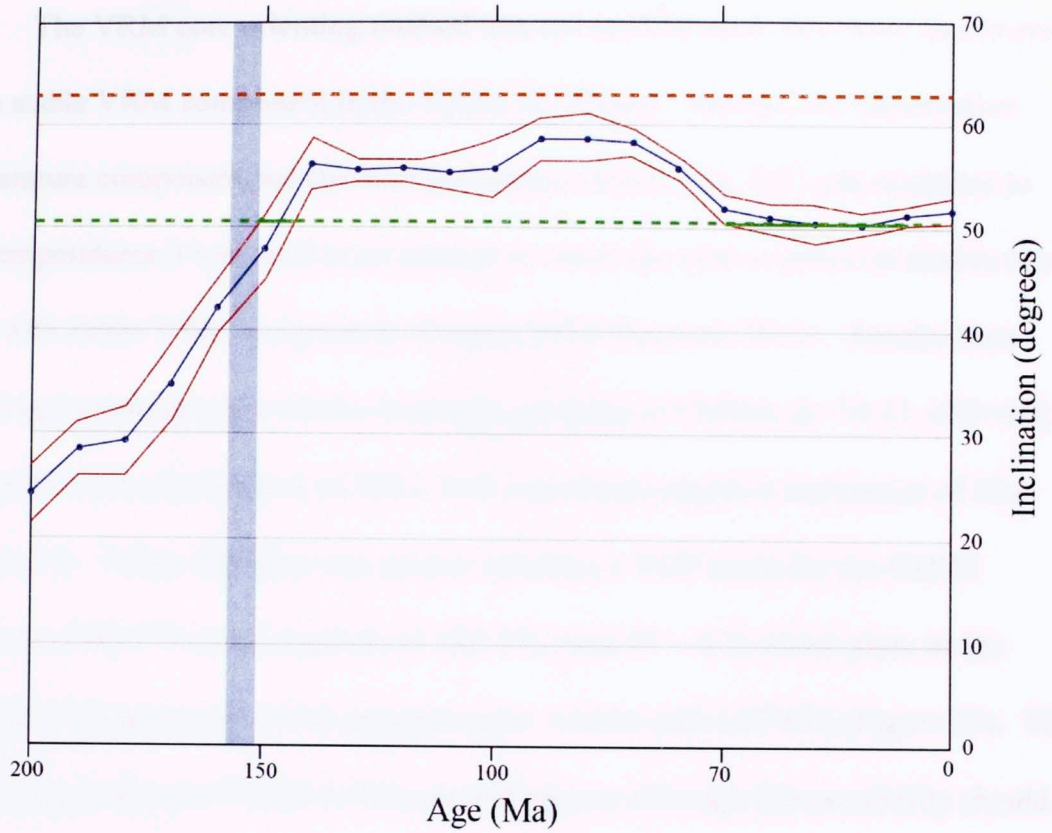

Figure 13: Average inclinations of intermediate and high temperature components. Because both cores are unoriented, this graph was created from Besse and Courtillot (2002) inclination values associated with North America and tied to core location. The transparent blue bar bounds Kimmeridgian time. The blue line is inclination values dating back to the beginning of the Jurassic and red lines are alpha95 error bars. The green dashed line is set at 50.5 degrees (the average inclination of the ChRM component in the Snider A1-H and Coleman Gas Unit 1-6 cores) and is bold where remagnetizations may have potentially occurred. The orange dashed line set at 63 degrees represent the averaged intermediate temperature component from both cores.

The VRM core orienting method was not used because only three specimens had a stable VRM component in the Snider A1-H core. Because the intermediate temperature component has elevated inclination values (avg. 71°) and moderate to low temperatures it was used in an attempt to orient the core as previous studies have done with stable VRM components (Dennie 2010; Farzaneh 2012). Results from orienting components provided a moderate grouping of ChRMs (k=30.33, α95=4.9) that have a mean declination of 168.2 with a moderate negative inclination of 52.6 (Figure 14). Fisher statistics was used to calculate a VGP mean for the ChRM (Latitude of 80.1°N and Longitude of 182.2°E; beta 95 = 5.7) which plots on the Paleogene/Neogene part of the apparent polar wander path (APWP) (Figure 15). This could suggest that the ChRM is Paleogene/Neogene although this possibility should be treated with caution because the intermediate temperature component is not a VRM.

All components (stable and unstable) were plotted on core photos (Appendix C) to look for any correlations between magnetizations and facies or healed fractures. No correlation to facies was observed. In virtually every zone that has vertical fractures stable magnetizations are present. In many other places without vertical fractures there were also stable magnetizations. This does not support a connection between the veins and the remagnetization. However, the limited size of the core makes it impossible to trace the exact path of these vertical fractures and, therefore, the extent and role they play in the preserved magnetization within the Snider A1-H core remains uncertain.

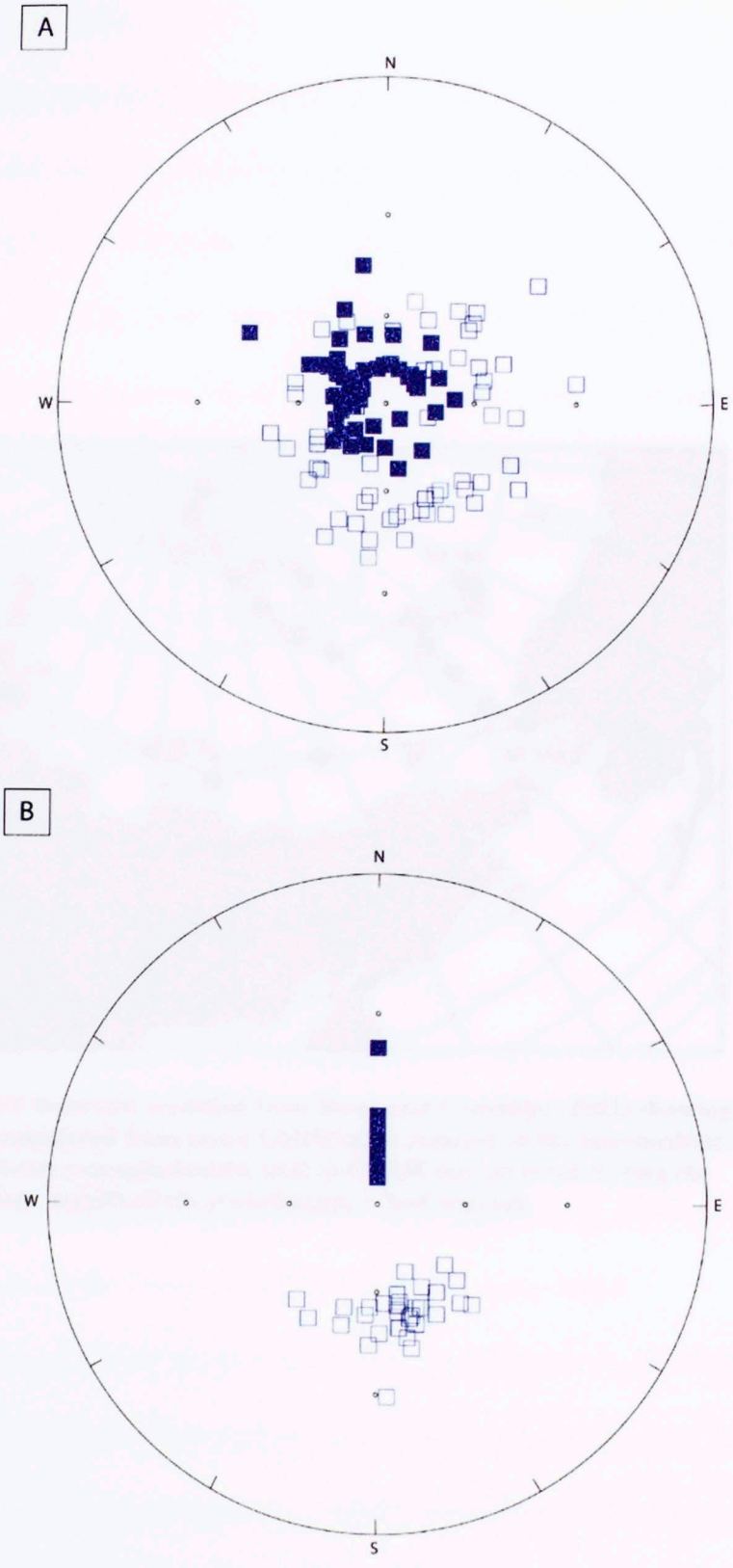

Figure 14: (A) Stereoplot showing intermediate temperature components (closed) and ChRM components (open) from the Snider A1-H core. (B) Stereoplot with intermediate component rotation back to modern declination and resulting grouping of ChRM, which suggests the intermediate temperature component may have been acquired in the Paleogene/Neogene.

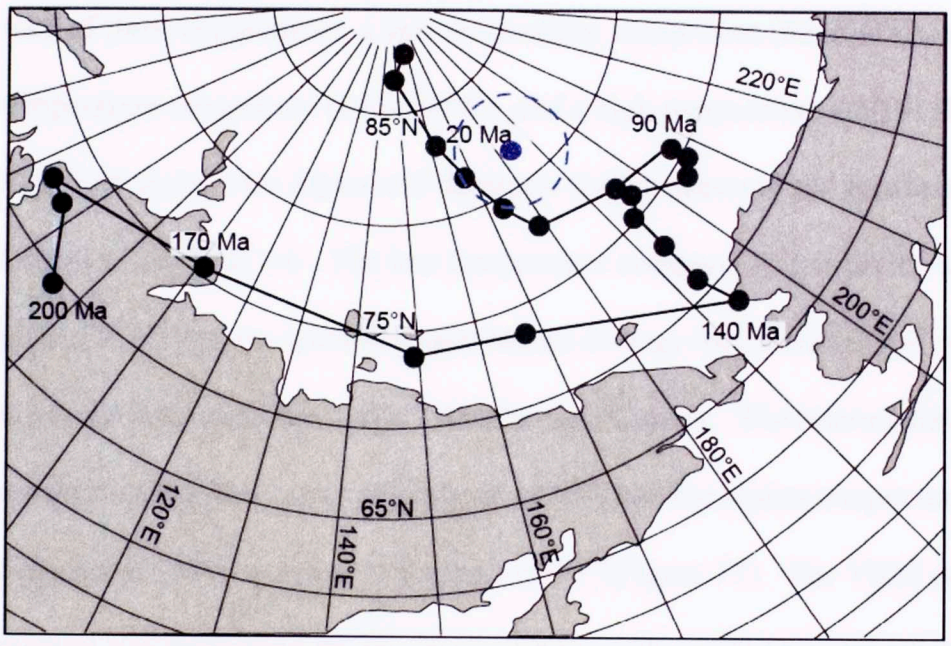

Figure 15: APWP depiction modified from Besse and Courtillot (2002) showing placement of remagnetization calculated from mean ChRM after rotation of the intermediate temperature component and shows remagnetization held in ChRM has occurred during the Paleogene/Neogene. Beta95 circle of confidence = 5.65 degrees.

Coleman Gas Unit 1-6

Sixty-one specimens were analyzed from the Coleman Gas Unit 1-6 core. Twenty-seven specimens had a ChRM and fifteen had an intermediate temperature component. Because LTD treatments did not change components in the Snider A1-H specimens this technique was not performed on the Coleman specimens.

Thermal demagnetization of the Coleman Gas Unit 1-6 samples removed a total of three components, a low temperature component (80-160°C), a moderate temperature component (140-240°C), and a high temperature ChRM (260-340°C). Figure 16 shows two Zijderveld diagrams from representative specimens from the Coleman Gas Unit 1-6. The low temperature component, interpreted as a VRM, was picked in twenty-six specimens and has an average inclination of 64° which is close to the modern inclination of 61° for Harrison County. The intermediate temperature component has an average inclination of 55°, and the higher temperature ChRM component has an average inclination of 49° (Figure 17). The VRM orienting method was performed for the 26 specimens with a VRM but did not produce good grouping of the intermediate or high temperature components. Six of the specimens have shallow ChRM associated with curved demagnetization paths on the Zijderveld diagram that may be the result of vector addition (Figure 16B).

Because core orientation could not be accomplished for the Coleman Gas Unit 1-6 both intermediate and high temperature ChRM components were plotted on the inclination versus age plot (Figure 13). High temperature ChRM inclination values (49°) are similar to Snider A1-H specimens (52°) and show a Late Jurassic/Early Cretaceous (150-140 Ma) remagnetization or a Cenozoic remagnetization.

Intermediate temperature ChRM inclination values (55°) coincide with remagnetization occurring in the Cretaceous.

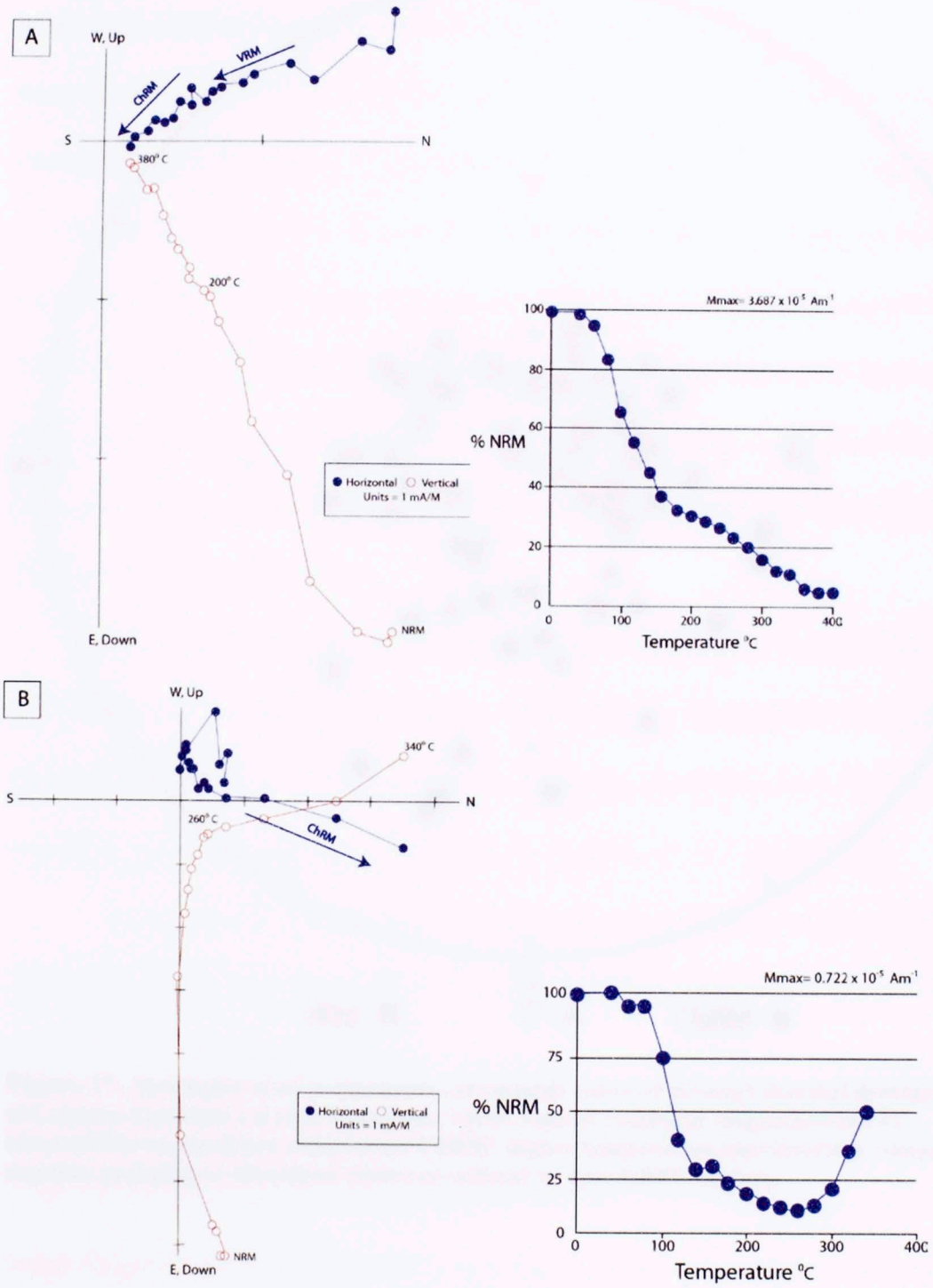

Figure 16: Representative Zijderveld diagrams from the Coleman Gas Unit 1-6 specimens. (A) VRM and ChRM removed through thermal demagnetization up to 380°C with a moderate inclination and northwesterly direction. (B) Specimen where only ChRM removed. Note curvature of inclination that may suggest vector addition. Coleman specimens less distinct in their magnetic carriers than Snider specimens.

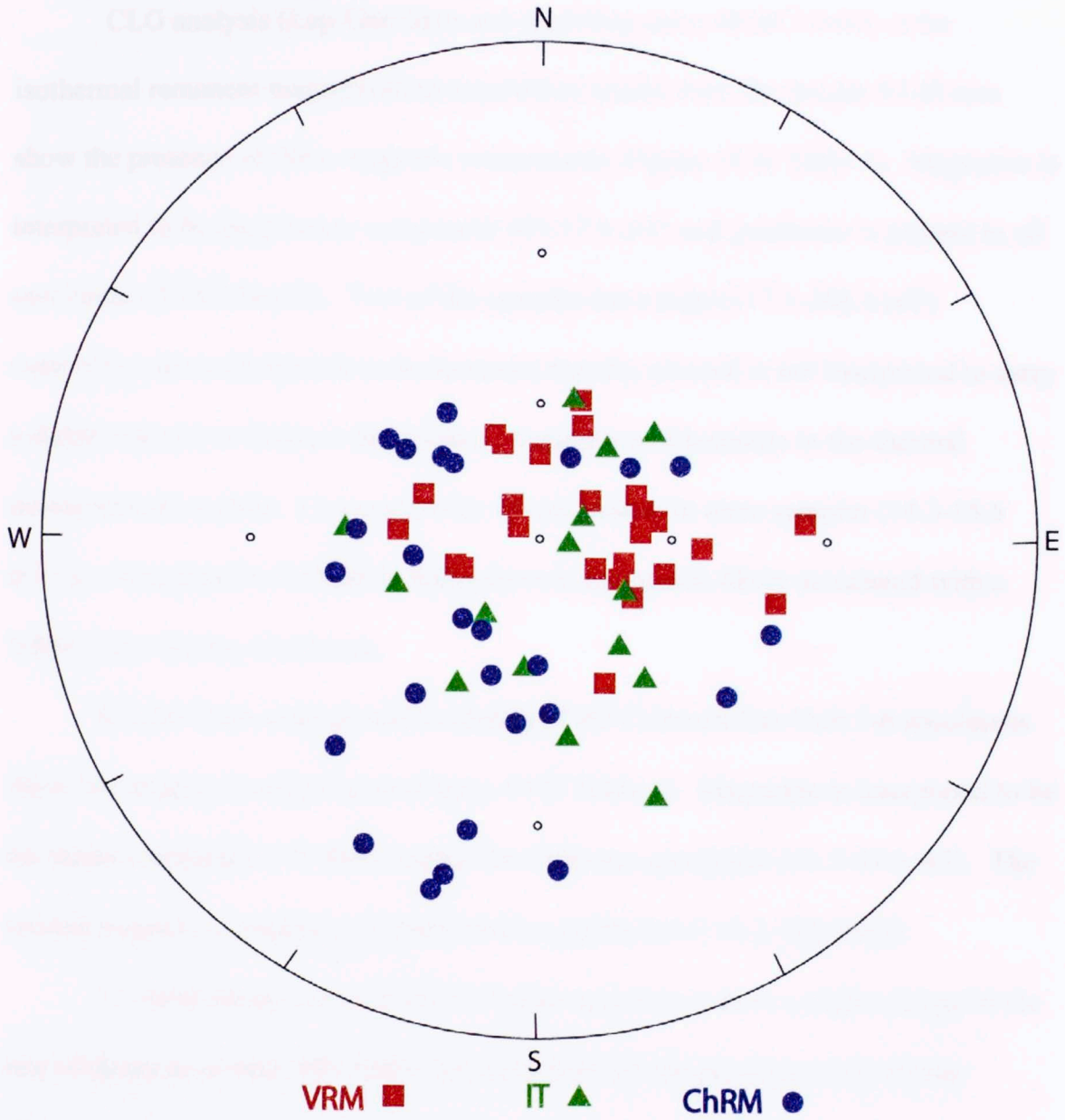

Figure 17: Stereoplot of all components (unrotated) removed through thermal demagnetization of Coleman Gas Unit 1-6 core specimens. VRM- viscous remanent magnetization; IT- intermediate temperature component; ChRM- higher temperature characteristic component. No common grouping or directions observed without or with VRM rotation.

4.4 Rock Magnetism

CLG analysis (Lap-Gap-Sap) and modeling using IRMUNMIX of the isothermal remanent magnetization acquisition results from the Snider A1-H core show the presence of three magnetic components (Figure 18 & Table 1). Magnetite is interpreted to be the primary component (49-57.4 mT) and pyrrhotite is present in all specimens (70.6-174 mT). Two of the samples have high (117.1-208.4 mT) coercivity values interpreted to be hematite, but this mineral is not interpreted to carry a stable remanence because there was no suggestion of hematite in the thermal demagnetization plots. Low coercivity values present in three samples (14.3-15.6 mT) are interpreted to be held in multi-domain magnetite, likely associated with a VRM in the Snider A1-H core.

Results from analysis and modeling of the Coleman Gas Unit 1-6 specimens show two magnetic components (Figure 19 & Table 1). Magnetite is interpreted to be the major component (75-86%) within the Coleman specimens (41.5-59.6 mT). The second magnetic component is interpreted as pyrrhotite (112.2-192.3 mT).

Tri-axial decay curves from the Snider specimens show a slight change in the rate of decay at or near 300-320°C that may indicate the presence of pyrrhotite (Figure 20). Specimens reach zero magnetization around 400°C which suggests the presence of magnetite. Decay curves for the Coleman specimens do not provide evidence for pyrrhotite but show decay above 350°C that indicate magnetite as the major magnetic mineral (Figure 21). In order to confirm the presence of magnetite and particularly pyrrhotite in the two cores, rock magnetic studies at the Institute for Rock Magnetism are necessary (e.g. Manning and Elmore 2012).

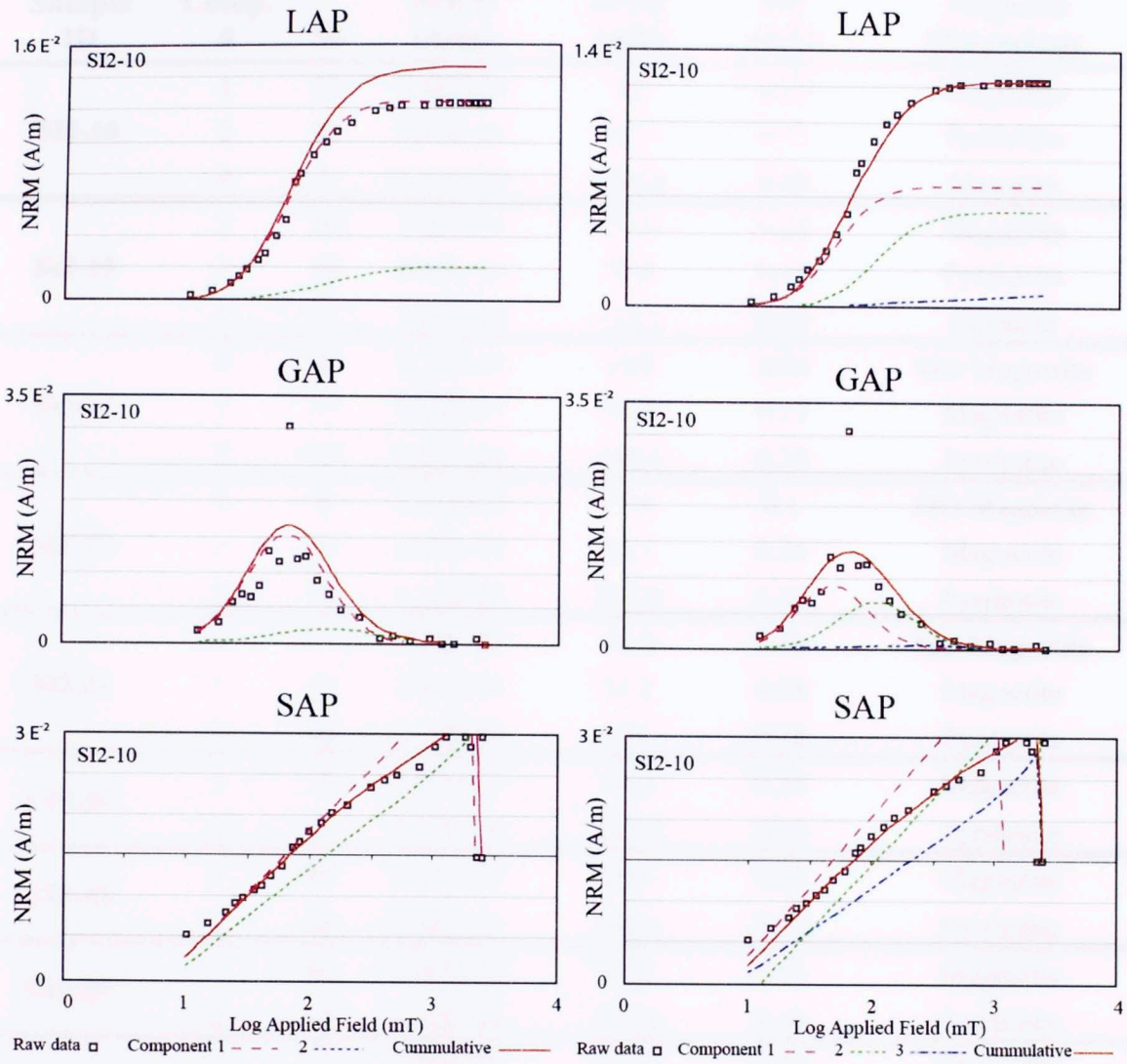

Figure 18: Representative Lap-Gap-Sap acquisition curves for the Snider A1-H specimens. Analysis shows a best fit for three components (right) as compared to two components (left). Lap-Linear acquisition plot; Gap- Gradient acquisition plot; Sap- Standardized acquisition plot (Kruvier et al. 2001).

Table 1. CLG analysis of Snider A1-H and Coleman Gas Unit 1-6

Sample ID	Comp. #	%	SIRM (A/m)	B 1/2 (mT)	DP (mT)	Magnetic Mineralogy
SI2-10	1	53	6.60E-03	49	0.29	Magnetite
	2	42	5.19E-03	107.1	0.31	Pyrrhotite
	4	5	6.34E-04	208.4	0.48	Hematite
SI2-15	1	59	2.85E-02	57.4	0.32	Magnetite
	2	19	9.02E-03	70.6	0.13	Pyrrhotite
	4	22	1.04E-02	117.1	0.39	Hematite
SI2-17	3	6	2.22E-04	14.9	0.09	MD Magnetite
	1	71	2.60E-03	55.4	0.27	Magnetite
	2	23	8.62E-04	140.4	0.38	Pyrrhotite
SI2-23	3	6	2.01E-03	15.6	0.1	MD Magnetite
	1	63	2.25E-02	55.1	0.26	Magnetite
	2	31	1.12E-02	127.3	0.35	Pyrrhotite
SI2-31	3	5	1.23E-03	14.3	0.41	MD Magnetite
	1	61	1.60E-04	51.2	0.08	Magnetite
	2	35	2.15E-03	174	0.28	Pyrrhotite
CI1-16	1	79	3.27E-03	54.2	0.33	Magnetite
	2	21	8.69E-04	181.6	0.39	Pyrrhotite
CI1-18	1	80	6.19E-03	58.9	0.32	Magnetite
	2	20	1.52E-03	166.3	0.39	Pyrrhotite
CI1-29	1	86	4.06E-03	45.2	0.31	Magnetite
	2	14	6.70E-04	172.6	0.46	Pyrrhotite
CI2-12	1	75	3.88E-03	41.5	0.29	Magnetite
	2	25	1.32E-03	112.2	0.41	Pyrrhotite
CI2-18	1	78	1.06E-03	59.6	0.32	Magnetite
	2	22	2.99E-04	192.3	0.34	Pyrrhotite

Table 1: Results from CLG analysis of specimens from the Snider A1-H and Coleman Gas Unit 1-6. Modeling on Snider specimens showed the presence of four magnetic minerals while modeling on Coleman showed the presence of two magnetic minerals. Mineralogy interpretations based upon Peters & Dekkers (2003) magnetic parameters.

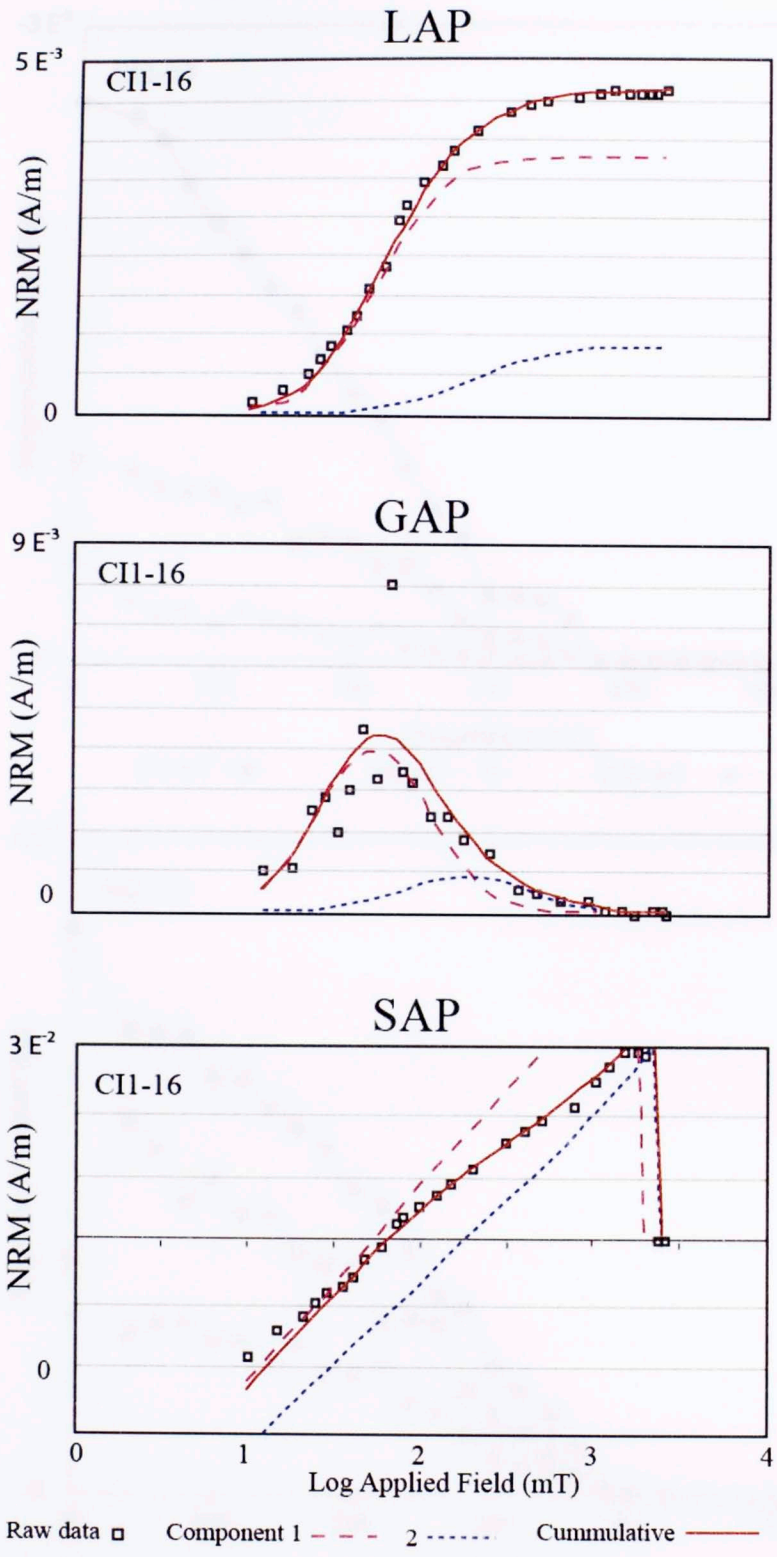

Figure 19: Representative Lap-Gap-Sap acquisition curves for the Coleman specimens. Two magnetic minerals modeled to be present within the Coleman Gas Unit 1-6 specimens, the primary of which is magnetite (41.5-59.6 mT). Table 1. shows magnetite contribution in the Coleman specimens to range from 75-86%.

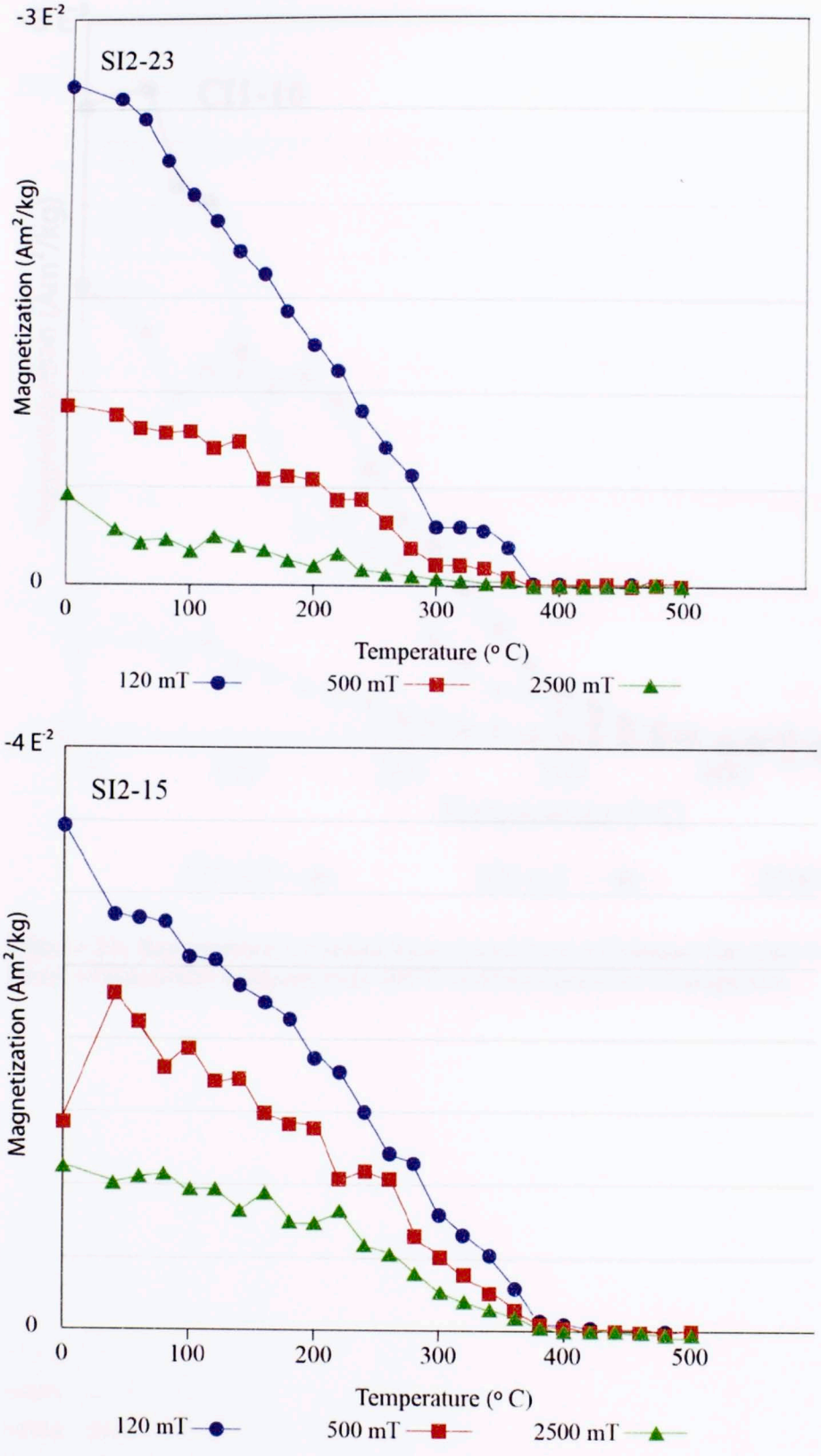

Figure 20: **Representative triaxial decay curves from Snider A1-H IRM specimens. Decay on specimens complete near 400°C indicating presence of magnetite. Note- incongruities in both curves near 300-320°C that may indicate the presence of pyrrhotite.**

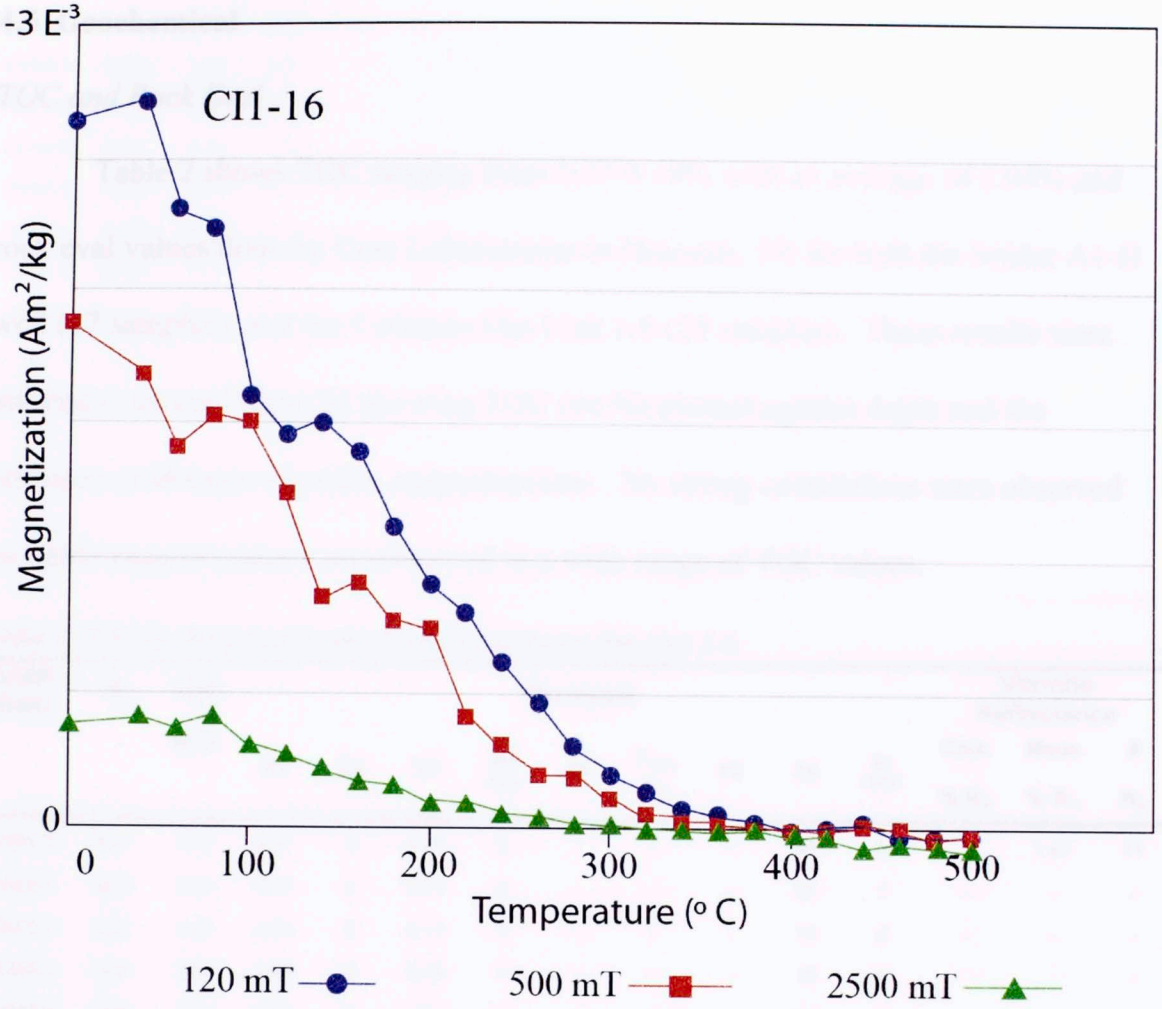

Figure 21: Representative triaxial decay curve from a Coleman Gas Unit 1-6 IRM specimen. Decay of specimens complete near 400°C indicates presence of magnetite.

4.5 Geochemical

TOC and Rock Eval

Table 2 shows TOC ranging from 0.37-4.19% with an average of 2.04% and rock eval values done by Core Laboratories in Houston, TX for both the Snider A1-H well (37 samples), and the Coleman Gas Unit 1-6 (25 samples). These results were utilized to create Figure 22 showing TOC (wt %) plotted against depth and the presence or absence of stable magnetizations. No strong correlations were observed as stable magnetizations are observed in a wide range of TOC values.

Table 2. TOC and Rock Eval Snider A1-H and Coleman Gas Unit 1-6

Depth (feet)	ID	TOC	Pyrolysis									Vitrinite Reflectance		
		wt%	S1	S2	S3	S2 /S3	PI	T_{max} (°C)	HI	OI	S1 /TOC	Calc % R_o	Meas % R_o	# R_o
10324.5	SC1	0.37	0.01	0	0.25	0	-	-	-	68	3	-	1.41	11
10335.5	SC2	0.59	0.04	0	0.17	0	-	-	-	29	7	-	-	-
10345.5	SC3	1.43	0.13	0	0.14	0	-	-	-	10	9	-	-	-
10355.5	SC4	0.98	0.05	0	0.16	0	-	-	-	16	5	-	-	-
10366.0	SC5	1.07	0.02	0	0.2	0	-	-	-	19	2	-	-	-
10375.0	SC6	1.54	0.08	0	0.13	0	-	-	-	8	5	-	1.47	8
10385.0	SC7	2.08	0.24	0	0.11	0	-	-	-	5	12	-	-	-
10395.5	SC8	1.53	0.15	0	0.19	0	-	-	-	12	10	-	-	-
10405.5	SC9	2.55	0.11	0	0.12	0	-	-	-	5	4	-	-	-
10415.5	SC10	2.56	0.3	0	0.14	0	-	-	-	5	12	-	-	-
10424.0	SC11	1.43	0.04	0	0.04	0	-	-	-	3	3	-	1.46	5
10435.0	SC12	2.75	0.08	0.02	0.2	0.1	0.8	419	1	7	3	0.38	-	-
10445.0	SC13	2.02	0.13	0	0.18	0	-	-	-	9	6	-	-	-
10454.0	SC14	1.99	0.05	0	0.63	0	-	-	-	32	3	-	-	-
10460.5	SC15	1.86	0.36	0	0.23	0	-	-	-	12	19	-	-	-
10475.5	SC16	1.52	0.08	0	0.31	0	-	-	-	20	5	-	1.52	3
10485.5	SC17	2.34	0.38	0	0.27	0	-	-	-	12	16	-	-	-
10495.0	SC18	1.8	0.3	0	0.18	0	-	-	-	10	17	-	-	-
10505.0	SC19	2.3	0.06	0	0.31	0	-	-	-	13	3	-	-	-
10515.0	SC20	1.74	0.05	0	0.27	0	-	-	-	16	3	-	-	-
10525.0	SC21	1.91	0.03	0	0.37	0	-	-	-	19	2	-	1.58	9
10535.0	SC22	1.95	0.18	0	0.21	0	-	-	-	11	9	-	-	-
10546.0	SC23	1.97	0.04	0	0.28	0	-	-	-	14	2	-	-	-

10555.0	SC24	2.14	0.26	0	0.11	0	-	-	-	5	12	-	-	-
10565.5	SC25	1.97	0.03	0	0.19	0	-	-	-	10	2	-	-	-
10575.0	SC26	2.58	0.04	0	0.72	0	-	-	-	28	2	-	1.63	11
10585.0	SC27	2.54	0.2	0	0.17	0	-	-	-	7	8	-	-	-
10595.5	SC28	1.74	0.17	0	0.36	0	-	-	-	21	10	-	-	-
10605.5	SC29	2.12	0.03	0	0.32	0	-	-	-	15	1	-	-	-
10615.5	SC30	2.81	0.16	0	0.24	0	-	-	-	9	6	-	-	-
10625.0	SC31	1.62	0.2	0	0.12	0	-	-	-	7	12	-	1.65	6
10635.0	SC32	2.18	0.3	0	0.28	0	-	-	-	13	14	-	-	-
10645.5	SC33	2.2	0.21	0	0.41	0	-	-	-	19	10	-	-	-
10655.5	SC34	1.48	0.14	0	0.23	0	-	-	-	16	9	-	-	-
10665.0	SC35	2.32	0.16	0	0.28	0	-	-	-	12	7	-	-	-
10675.0	SC36	1.91	0.23	0	0.27	0	-	-	-	14	12	-	1.68	15
10685.5	SC37	1.62	0.24	0	0.53	0	-	-	-	33	15	-	-	-
10808.5	CG1	1.6	0.21	0.49	0.15	3.27	0.3	445	31	9	13	0.85	-	-
10824.5	CG2	1.88	0.23	0.25	0.16	1.56	0.48	437	13	9	12	0.71	-	-
10828.0	CG3	1.43	0.18	0.4	0.17	2.35	0.31	433	28	12	13	0.63	-	-
10836.0	CG4	1.74	0.13	0.29	0.16	1.81	0.31	426	17	9	7	0.51	-	-
10848.0	CG5	1.75	0.1	0.35	0.11	3.18	0.22	521	20	6	6	2.22	-	-
10862.5	CG6	1.62	0.08	0.23	0.07	3.29	0.26	500	14	4	5	1.84	-	-
10887.0	CG7	2.55	0.27	0.54	0.17	3.18	0.33	524	21	7	11	2.27	-	-
10894.5	CG8	2.44	0.13	0.46	0.09	5.11	0.22	514	19	4	5	2.09	-	-
10898.0	CG9	2.27	0.18	0.3	0.09	3.33	0.38	515	13	4	8	2.11	-	-
10930.5	CG10	2.01	0.12	0.36	0.09	4	0.25	460	18	4	6	1.12	-	-
10935.5	CG11	2.24	0.12	0.47	0.09	5.22	0.2	462	21	4	5	1.16	-	-
10954.5	CG12	2.4	0.11	0.47	0.12	3.92	0.19	521	20	5	5	2.22	-	-
10978.0	CG13	2.82	0.09	0.38	0.07	5.43	0.19	529	13	2	3	2.36	-	-
10990.5	CG14	2.56	0.1	0.44	0.12	3.67	0.19	527	17	5	4	2.33	-	-
11009.5	CG15	1.88	0.12	0.18	0.12	1.5	0.4	450	10	6	6	0.94	-	-
11013.0	CG16	1.9	0.15	0.29	0.09	3.22	0.34	455	15	5	8	1.03	-	-
11029.0	CG17	2.79	0.14	0.42	0.11	3.82	0.25	527	15	4	5	2.33	-	-
11038.5	CG18	2.09	0.07	0.32	0.08	4	0.18	491	15	4	3	1.68	-	-
11047.5	CG19	2.27	0.27	0.39	0.09	4.33	0.41	512	17	4	12	2.06	-	-
11059.5	CG20	1.6	0.19	0.29	0.15	1.93	0.4	537	18	9	12	2.51	-	-
11074.5	CG21	2.8	0.13	0.43	0.09	4.78	0.23	518	15	3	5	2.16	-	-
11082.5	CG22	3.57	0.08	0.53	0.14	3.79	0.13	538	15	4	2	2.523	-	-
11092.5	CG23	3.11	0.06	0.27	0.08	3.38	0.18	533	9	3	2	2.43	-	-
11101.5	CG24	4.19	0.05	0.38	0.09	4.22	0.12	534	9	2	1	2.45	-	-
11114.0	CG25	1.74	0.17	0.2	0.13	1.54	0.46	513	11	7	10	2.07	-	-

Table 2: TOC and Rock eval values from Snider A1-H (SC samples) and Coleman Gas Unit 1-6 (CG samples). Modified from Core Lab provided by GMXR and Samson Energy.

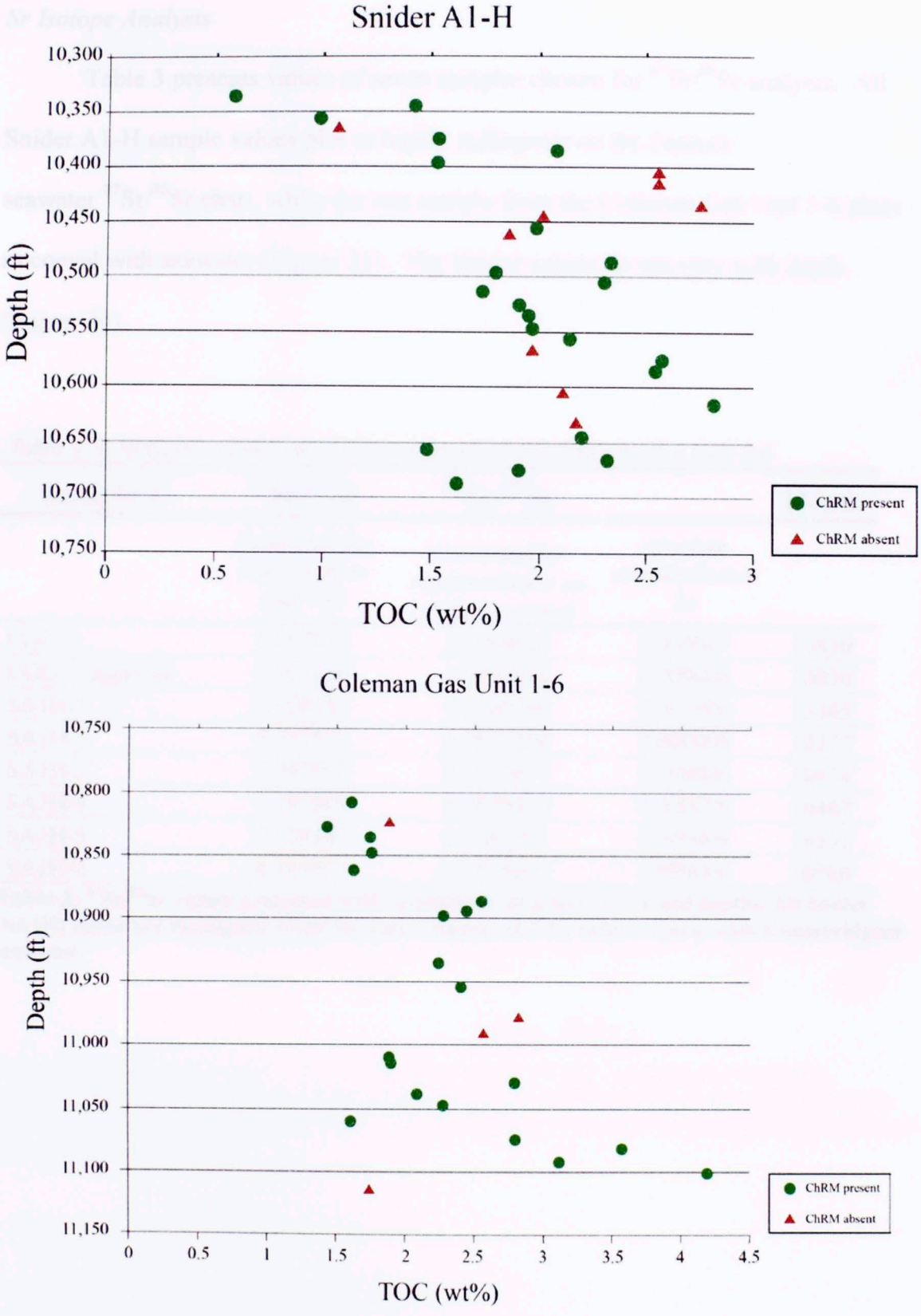

Figure 22: TOC (wt%) data plotted against depth. Used as a proxy for presence/absence test when associating magnetization timing with maturation of organics in the Haynesville. Stable magnetizations associated with productive TOC values may indicate acquisition of ChRM to be contemporaneous with maturation of organic matter.

Sr Isotope Analysis

Table 3 presents values of seven samples chosen for $^{87}Sr/^{86}Sr$ analysis. All Snider A1-H sample values plot as highly radiogenic on the Jurassic seawater $^{87}Sr/^{86}Sr$ chart, while the one sample from the Coleman Gas Unit 1-6 plots as coeval with seawater (Figure 23). The Snider values do not vary with depth (Figure 24).

Table 3. Sr isotope analysis results for Snider A1-H and Coleman Gas Unit 1-6

Sample #	$^{87}Sr/^{86}Sr$	$^{87}Sr/^{86}Sr$		Depth
	Corrected for fractionation and ^{87}Rb	*Corrected for representation on seawater curve*	*Absolute standard error 2σ*	
CGU-1	0.707015	0.7069905	0.000007	10830'
CGU-1 duplicate	0.707016	0.7069916	0.000006	10830'
SA1H-1	0.708103	0.7080790	0.000006	10365'
SA1H-2	0.707974	0.7079498	0.000006	10377'
SA1H-3	0.707992	0.7079677	0.000006	10454'
SA1H-4	0.707869	0.7078450	0.000006	10482'
SA1H-5	0.708183	0.7081591	0.000006	10551'
SA1H-6	0.707933	0.7079093	0.000006	10560'

Table 3: $^{87}Sr/^{86}Sr$ values presented with corrections, absolute errors and depths. All Snider (SA1H) ratios are radiogenic while the lone Coleman (CGU) ratio is coeval with Kimmeridgian seawater.

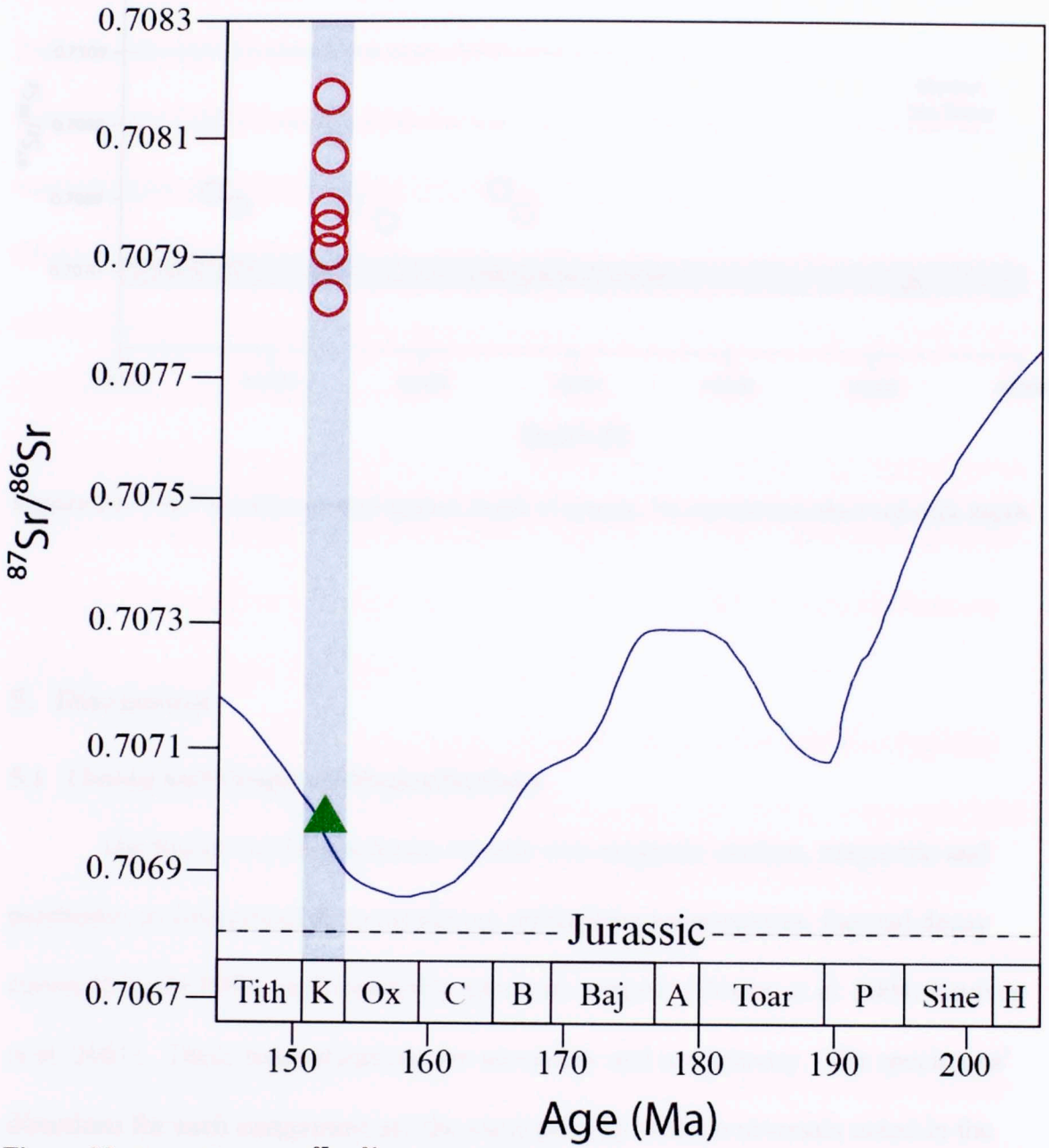

Figure 23: Coeval seawater $^{87}Sr/^{86}Sr$ ratios plotted versus age represented by blue line. Transparent blue bar outlines Kimmeridgian. Red open circles are Snider A1-H samples and green triangle is Coleman Gas Unit 1-6 sample. All Snider ratios plot as radiogenic and Coleman sample plots as coeval.

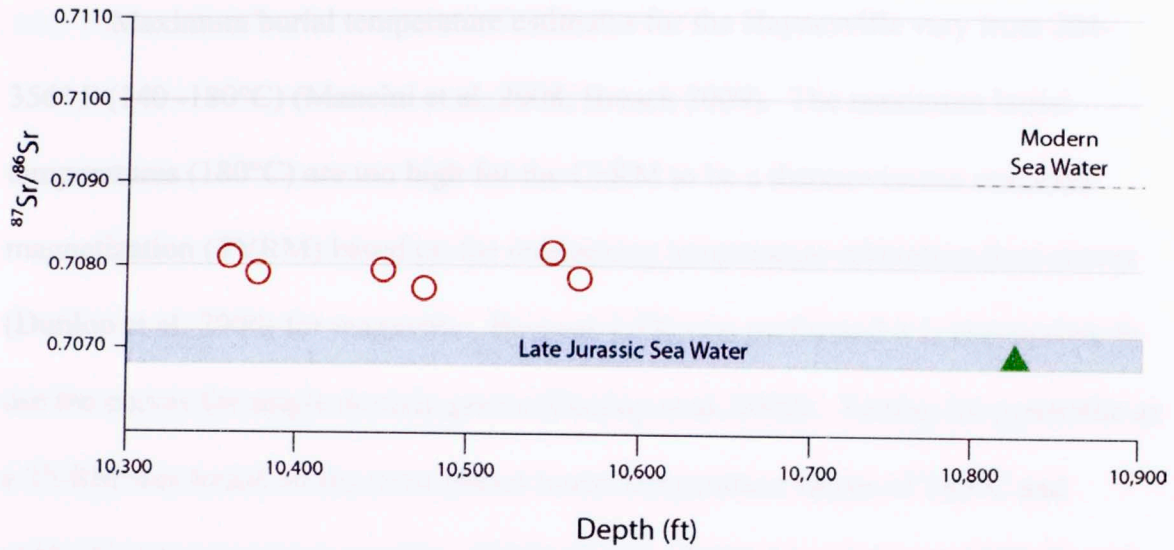

Figure 24: $^{87}Sr/^{86}Sr$ ratios plotted against depth of sample. No correlation observed with depth.

5. Discussion

5.1 Timing and Origin of Magnetizations

The Snider A1-H specimens contain two magnetic carriers, magnetite and pyrrhotite, as interpreted from maximum unblocking temperatures, thermal decay curves (Lowrie 1990), and coercivity spectrum analysis (Heslop et al. 2004; Kruiver et al. 2001). These magnetizations are secondary and not primary. The specimens' directions for each component are the same polarity with no reversals noted in the cores. If magnetization were primary one would expect to 'discover' multiple reversals as the Kimmeridgian underwent numerous reversals (Cande and Dent 1995). It is interesting to note however that the polarities for the ChRM are different in the two cores (reversed in the Snider and normal in the Coleman). This indicates that the ChRM was not acquired at exactly the same time in both cores.

Maximum burial temperature estimates for the Haynesville vary from 284-356° F (140 -180°C) (Mancini et al. 2008; Bresch 2009). The maximum burial temperatures (180°C) are too high for the ChRM to be a thermoviscous remanent magnetization (TVRM) based on the unblocking temperature-relaxation time curves (Dunlop et al. 2000) for magnetite. Because LTD was performed it is appropriate to use the curves for single domain grains (Dunlop et al. 2000). Testing for pyrrhotite as a TVRM was based on the most liberal burial temperature values of 180°C and unblocking temperatures reaching 320°C (Dunlop 2000; Mancini et al. 2008; Bresch 2009). The unblocking temperatures are too high for a TVRM. Both the ChRM in magnetite and pyrrhotite components are interpreted as CRMs (chemical remanent magnetization) within the Snider A1-H specimens.

Coleman Gas Unit 1-6 specimens are also interpreted to hold two magnetic components, a ChRM in magnetite and an intermediate temperature component held in pyrrhotite. The intermediate temperature component is less distinct than in the Snider specimens. These components are also interpreted as CRMs based upon same criterion for the Snider A1-H specimens.

Two distinct possibilities exist for interpretation of timing of CRMs held in magnetite. Based upon inclination values (Figure 13), either an early remagnetization (150-140 Ma) or a late remagnetization (70-20 Ma) are viable interpretations.

Vein testing on the Snider A1-H did not show a relationship between the CRMs and the veins. Both veined and unveined rock contained the CRM. The Coleman contains fewer veins but also holds the CRMs. These results suggest that a remagnetization event caused by fluids in veins is unlikely. The remagnetizations

may be associated with a burial process (see below). An important caveat with this interpretation is that the cores only provide a small amount of rock, and veins could be present in the shale but were not cored.

Core rotation results (Figure 14) show good grouping of CRM specimens in the Snider A1-H and plot near the Paleogene/Neogene part of the APWP (Figure 15). This suggests that a late (Paleogene/Neogene) remagnetization of the magnetite component is a viable interpretation.

Anomalously steep inclination values for the intermediate temperature component within the Snider A1-H indicate a remagnetization occurring anywhere from the Late Cretaceous to the Paleogene/Neogene. Inclination values plotting closest to the Late Cretaceous suggests this to be the most likely timing of remagnetization held within pyrrhotite. The Q-test indicates that steep inclination values are not caused by a DIRM.

5.2 Origin and Mechanism of Remagnetization

As previously mentioned, burial diagenetic processes may be the best explanation for the origin of the magnetite CRM. Previous studies have established a relationship between maturation of organic matter and precipitation of authigenic magnetite and pyrrhotite (e.g. Elmore et al. 1987; Reynolds et al. 1993; Brothers et al. 1996; Banjeree et al. 1997; Aldana et al. 2003). The TOC values in both the Snider and Coleman specimens are moderate (~2-4%) and are associated with the CRMs. The organic matter matured around 140 Ma (Torsch 2012) and this is one of the possible times for magnetite CRM acquisition based on the inclination values (Figure

13). Authigenic magnetite may also be associated with dissolution-reprecipitation of pyrite (Brothers et al. 1996) or iron (Fe) being released during smectite to illite transformation (Hirt et al. 1993; Katz et al. 1998).

Remagnetization by late fluid alteration is also possible for the magnetite CRM. Many paleomagnetic studies have related hydrothermal and basinal fluids to CRMs in authigenic magnetic minerals (e.g. Elmore et al. 2012; Zechmeister et al. 2012; Dennie et al. 2012) and some studies have tied these CRMs to dolomitization (Symons et al. 1999; Cioppa et al. 2000). Salt tectonic activity associated with the Louann Formation may be a possible trigger for activation for the movement of basinal fluids within the Haynesville Shale. Arching of the Sabine Uplift in the Cretaceous has been attributed to compressional forces and not igneous intrusions or volcanism (Adams 2009).

Pyrrhotite interpreted as a Late Cretaceous remagnetization is likely associated with thermochemical sulfate reduction (TSR) occurring within the Haynesville perhaps activated by the Saltillo-St. Lawrence Shear System (Adams 2009). Pyrrhotite is a common byproduct during TSR of organic matter (Pierce et al. 1998) and TSR has recently been proposed as a mechanism for a pyrrhotite CRM in the Marcellus Shale (Manning 2011). The presence of byproducts of TSR (Machel 1987) such as sphalerite, cubic pyrite, and saddle dolomite support the interpretation of pyrrhotite remanence occurring during a TSR.

5.3 Diagenesis/Paragenesis

Early stages of paragenesis include pyrite, silica associated with allochems, as well as, primary calcite. A transition from aragonitic seas to calcite-rich seas is documented to have occurred in the Mid-Jurassic (Stanley et al. 2002), and thus the primary carbonate precipitation within the Haynesville Shale was low-magnesium calcite. This is evidenced by radial calcite observed in thin section analysis. Bladed dolomite in healed fractures and allochems are interpreted as replacement of primary marine phreatic calcite (Scholle & Ulmer-Scholle 2003) and its presence in horizontal veins may have occurred during sulfate reduction at shallow burial depths (Curtis 1980).

The heterogeneity in mineralogy of vertical veins and breccias may suggest multiple events of fracture activation and fluid flow. One such event may be related to the transition of maximum principal stress during burial. Activation of vertical fractures may also be timed with the onset of the Laramide Orogeny (Adams 2009). Burial history curves of the basin show uplift (~1,000 ft.) in the Cretaceous likely associated with the Saltillo-St. Lawrence Shear System (Mancini et al. 2008; Adams 2009). Formation of fractures may also be in part due to the over-pressured nature of the reservoir. Breccia features in the Snider A1-H and Coleman Gas Unit 1-6 are interpreted as being created from overpressure of fluids.

The presence of saddle dolomite may help with the relative dating of vertical veins within the Haynesville. Precipitation of saddle dolomite can be associated with hyper-saline brines (Machel 1987). Observed in vertical veins in the Snider A1-H this may suggest vertical veining occurred at shallow burial depths. However,

precipitation of saddle dolomite can occur in sulfate-rich rocks associated with hydrocarbons and at temperatures common to sphalerite precipitation (220°C). In black shales the hydrocarbon window typically opens around 8,000-9,800 ft. (2.5-3 km) in depth (Tourtelot 1979), which would suggest at least some of the vertical veining occurred as a late diagenetic process. The interpretation of a stable remanent magnetization being held in pyrrhotite may indicate that the Haynesville Shale was exposed to thermochemical sulfate reduction (TSR) providing further evidence that saddle dolomite, which can precipitate in TSR conditions, occurred as a late diagenetic event (Machel 1987). Therefore it is most likely that most vertical veining and healing of fractures occurred as a late diagenetic stage. Collecting fluid inclusion data was beyond the scope of this study, but if it could be extracted from these dolomites it would further aid in timing of saddle dolomite precipitation and the timing of vertical fractures in the Haynesville Shale.

Because of rapid deposition of sediments hydrocarbon maturation within portions of the Haynesville began relatively early, approximately 140 Ma. Modeling of hydrocarbon and water migration shows both lateral and vertical migration pathways in the Haynesville Shale (Torsch 2012). Precipitation of sphalerite and saddle dolomite may reasonably be associated with these migration pathways that formed at depth. Thermochemical sulfate reduction (TSR) can be associated with hydrocarbon migration and the generation of hydrogen sulfide (H_2S) in deep reservoirs as well as the precipitation of iron sulfides such as pyrite (Pierce et al. 1998; Machel 1998; Machel & Burton 1991). The abundance of late diagenetic pyrite replacement precipitating within both cores and anhydrite observed in brecciated

intervals suggests a zone of TSR may have occurred (Pierce et al. 1998; Machel 2001).

Sulfur-rich minerals also commonly precipitate within a shallow sulfate reduction zone with burial depths of ~3-30 ft. (1-10 m) in organic rich shales (Curtis 1980). Pyrite observed within the matrix has been interpreted as an early diagenetic stage while pyrite within veins and allochems is interpreted as a late stage diagenetic event. Previous diagenetic studies of the Barnett and Marcellus shales produced similar findings of sulfur-rich minerals such as barite, celestite, and sphalerite within healed fractures and allochems (Dennie et al. 2012; Manning 2011). These findings give credence to the chemical nature of organic rich shales being controlled less by geologic setting and more by geologic processes (Tourtelot 1979).

Of note from this study is the stark difference in vertical fractures present in the Snider A1-H core and absent in the Coleman Gas Unit 1-6 (Appendix A, Coleman Core description and Appendix B, Snider A1-H core description). The presence of natural vertical fractures in the Haynesville Shale has been mostly theoretical from an engineering, modeling, and production standpoint (Hammes et al. 2011; Torsch 2012). The heterogeneity between these two cores and their fractures suggests isolated and geographically restricted diagenetic events to have occurred within the Haynesville Shale.

The impact of diagenetic events, both burial and late, and fluid movements through shales associated with these events have implications for production of hydrocarbons. The precipitation and extent of silica rich minerals (e.g. albite) and veins alongside detrital quartz will yield more favorable conditions in fracturing (both

natural and hydraulic) and positively influence the mechanical behavior of shale. Conversely the extent of certain diagenetic minerals may have a negative impact on production (e.g. anhydrite) and is therefore equally important as it pertains to mechanical behavior of the reservoir during hydraulic fracturing.

Diagenetic and paleomagnetic similarities of the Haynesville Shale with the Barnett and Marcellus Shales (Dennie 2010; Manning 2011) indicate the importance of diagenesis in developing productive gas shales. The results also suggest that externally derived fluids probably did alter the Haynesville Shale. This suggests that the Haynesville Shale was an open system with respect to interactions with hydrothermal fluids.

5.4 Geochemistry and Origin of Fluids

A few possibilities exist in regards to the origin of fluids altering the Haynesville during burial. Strontium isotope values from the Snider A1-H samples indicate the fluids had a radiogenic signature, which suggests evolved externally derived fluids. Dissolution of feldspar associated with the smectite to illite transformation can result in elevated $^{87}Sr/^{86}Sr$ values (Stueber et al. 1984) so the fluids could be internal to the Haynesville Shale. The Louann Salt cannot be ruled out as a possible source of the fluids that altered the Haynesville. Known $^{87}Sr/^{86}Sr$ values for the Louann are comparable to the values attained from carbonates in the Snider A1-H samples (Louann: 0.70838 vs. Snider A1-H mean: 0.7080) (Stueber et al 1984). The coeval strontium ratio attained from the Coleman Gas Unit 1-6 sample suggests that external fluids did not alter the rock. The Coleman sample was taken

from the anhydritic brecciated zone of the core. Underlying the Louann Formation is the Werner Anhydrite (Figure 1B), which has an $^{87}Sr/^{86}Sr$ value of 0.7070. The Coleman $^{87}Sr/^{86}Sr$ value of 0.70699 could also have been sourced by the Werner Anhydrite. The strontium isotopic data is inconclusive in terms of assessing the possibility that evolved externally derived fluids altered the Haynesville shale.

6. Conclusions

Paleomagnetic results from two unoriented Haynesville Shale cores from Harrison County, Texas show the presence of two CRMs held within magnetite and pyrrhotite. Testing for a drilling induced magnetization (DIRM) was performed and results show that it is not likely. LTD did not significantly effect the magnetizations.

Two viable interpretations for magnetite origin and timing are put forth. One model is for an early (Late Jurassic/Early Cretaceous) remagnetization associated with burial processes such as maturation of organic matter, which is consistent with the timing of the beginning of the oil/gas window. A late (Paleogene/Neogene) remagnetization associated with diagenetic basinal fluids is also possible based on the inclination values.

Pyrrhotite formation and remanence is interpreted as being related to TSR occurring within the Haynesville Shale. Inclination values indicate remagnetization to have likely occurred from the Late Cretaceous to Cenozoic. A Late Cretaceous remagnetization may correlate with the Saltillo-St. Lawrence Shear System.

Paragenesis produced from petrographic analysis reveals a complex diagenetic story in the Haynesville Shale. Horizontal veining and precipitation was followed by vertical veining and brecciation events. Heterogeneity in the vertical veins indicates multiple fluid flow events activated at numerous times, ranging from early burial as principal stress direction transitioned to normal and progressing all the way to the Cenozoic. Diagenetic events within the Haynesville are geographically restricted as evidenced by the presence of healed vertical fractures within the Snider A1-H core and the absence of vertical fractures in the Coleman Gas Unit 1-6 core. The presence of saddle dolomite, sphalerite, and cubic pyrite provide mineralogical evidence of TSR occurring in the Haynesville Shale. Precipitation of silica rich minerals and veins together with detrital quartz increase brittleness and, therefore, would benefit mechanical behavior and production of the Haynesville Shale in regards to natural and hydraulic fracturing.

References

Abbink, O., Targarona, J., Brinkhuis, H. & Visscher, H. 2001. Late Jurassic to earliest Cretaceous palaeoclimatic evolution of the southern North Sea. *Global and Planetary Change*, **30**, 231-256.

Adams, R.L. 2009. Basement tectonics and origin of the Sabine Uplift. *Gulf Coast Association of Geological Societies Transactions*, **59**, 3-19.

Aldana, M., Costanzo-Alvarez, V. & Diaz, M. 2003. Magnetic and mineralogical studies to characterize oil reservoirs in Venezuela. *The Leading Edge*, **22**, 526-528.

Banerjee, S., Elmore, R. D. & Engel, M. H. 1997. Chemical remagnetization and burial diagenesis; testing the hypothesis in the Pennsylvanian Belden Formation, Colorado. *Journal of Geophysical Research*, **102**, 24825–24842.

Besse, J. & Courtillot, V. 2002. Apparent and true polar wander and the geometry of the geomagnetic field over the last 200 Myr. *Journal of Geophysical Research*, **107**, doi: 10.1029/2000JB000050.

Bjorlykke, K. & Jahren, J. 2012. Open or closed geochemical systems during diagenesis in sedimentary basins: constraints on mass transfer during diagenesis and the prediction of porosity in sandstone and carbonate reservoirs. *American Association of Petroleum Geologists Bulletin*, **96**(12), 2193-2214.

Bresch, C. & Carpenter J. 2009. Preliminary analytical results: Haynesville shale in northern Panola County, Texas. *Gulf Coast Association of Geological Societies Transactions*, **59**, 121-124.

Blumstein, A. M., Elmore, R. D., Engel, M. H., Elliot, C. & Basu, A. 2004. Paleomagnetic dating of burial diagenesis in Mississippian carbonates, Utah. *Journal of Geophysical Research*, **109**, B04101, doi:10.1029/2003JB002698.

Boggs Jr., S. 1987. Principles of sedimentology and stratigraphy: Columbus, Ohio, Merrill Publishing Company, 45-53.

Brothers, L.A., Engel, M.H. & Elmore, R.D. 1996. A laboratory investigation of the late diagenetic conclusion of pyrite to magnetite by organically complex ferric iron. *Chemical Geology*, **130**, 1-14.

Buller, D. & Dix, M.D. 2009. Petrophysical evaluation of the Haynesville shale in northwest Louisiana and northeast Texas. *Gulf Coast Association of Geological Societies Transactions*, **59**, 127-143.

Burmester, R.F. 1976. Origin and stability of drilling induce remanence. *Geophysics Journal of the Royal Astronomical Society*, **48**, 1-14.

Cande, S.C. & Kent, D.V. 1995. Revised calibration of the geomagnetic polarity timescale for the Late Cretaceous and Cenozoic. *Journal of Geophysical Research*, **100**, 6093–6095.

Cicero, A.D., Steinhoff, I., McClain, T., Koepke, K.A. & Dezelle, J.D. 2010. Sequence stratigraphy of the Upper Jurassic mixed carbonate/siliciclastic Haynesville and Bossier shale depositional systems in east Texas and north Louisiana. *Gulf Coast Association of Geological Societies Transactions*, **60**, 133-148.

Cioppa, M.T., Al-Aasm, I.S., Symons, D.T.A, Lewchuk, M.T. & Gillen, K.P. 2000. Correlating petrologic, geochemical, and magnetic to date diagenetic and fluid flow events in the Moose Reservoir, Alberta, Canada. *Sedimentary Geology*, **131**, 109-129.

Curtis, C.D. 1980. Diagenetic alteration in black shales. *Journal of the Geological Society, London*, **137**, 189-194.

de Wall, H., & Worm, H. U. 2001. Recognition of drilling-induced remanent magnetization by *Q*-factor analysis: a case study from the KTB-drillholes. *Journal of Applied Geophysics*, **46**(1), 55-64.

Deng, J. 2011. An integrated paleomagnetic, geochemical, and diagenetic study of the Mississippian Barnett shale, Fort Worth Basin, Texas [Master's Thesis]. United States—Oklahoma: The University of Oklahoma.

Dennie, D. 2010. An integrated paleomagnetic and diagenetic investigation of the Barnett shale and underlying Ellenburger Group carbonates, Fort Worth Basin, Texas [Ph.D. dissertation]. United States -- Oklahoma: The University of Oklahoma.

Dennie, D., Elmore, R.D., Deng, J., Manning, E.B. & Pannalal, J. 2012. Palaeomagnetism of the Mississippian Barnett shale, Fort Worth Basin, Texas. *Geological Society, London, Special Publications*, **371**, doi: 10.1144/SP371.10

Dix, M.D., Spain, C., Sano, W.J., Casarta, N. & Richardson, A. 2010. Stratigraphy and depositional dynamics of the Haynesville-Bossier sequence: inferences from whole-rock elemental data. *American Association of Petroleum Geologists*, Annual Convention and Exhibition, April 2010, New Orleans, Louisiana.

Dunham, R. J. 1962. Classification of carbonate rocks according to depositional texture *In*: Classification of Carbonate Rocks (Ed. by Ham, W. E.). *American Association of Petroleum Geologists Memoir*, Tulsa, I, 108–121.

Dunlop, D. J. & Argyle, K. S. 1991. Separating Multidomain and Single-Domain-Like Remanences in Pseudo-Single-Domain Magnetites (215-540 nm) by Low-Temperature Demagnetization, *Journal of Geophysical Research*, **96**, 2007–2017.

Dunlop, D. J., Özdemir, Ö., Clark, D. A. & Schmidt, P.W. 2000. Time-temperature relations for the remagnetization of pyrrhotite (Fe_7S_8) and their use in estimating paleotemperatures, *Earth and Planetary Science Letters*, **176**, 107–116.

Elmore, R.D., Engel, M.H., Crawford, L., Nick, K., Imbus, S. & Sofer, Z. 1987. Evidence for a relationship between hydrocarbons and authigenic magnetite. *Nature*, **325**, 428-430.

Elmore, R.D., Muxworthy, A.R. & Aldana, M. 2012. Remagnetization and chemical alteration of sedimentary rocks. *Geological Society, London, Special Publications*, **371**, doi: 10.1144/SP371.15.

Farzaneh, S. 2012. An integrated paleomagnetic and diagenetic study of the Mississippian Limestones in northern Oklahoma [Master's Thesis]. United States—Oklahoma: The University of Oklahoma.

Fisher, R. A. 1953. Dispersion on a sphere. *Proceedings of the Royal Society of London, Series A*, **217**, 295–305.

Goldhammer, R.K. & Johnson, C.A. 2001. Middle Jurassic-Upper Cretaceous paleogeographic evolution and sequence-stratigraphic framework of the northwest Gulf of Mexico rim, *In:* Bartolini, C., Buffler, R.T. & Cantu-Chapa, A., eds. The western Gulf of Mexico Basin: Tectonics, sedimentary basins, and petroleum systems. *American Association of Petroleum Geologists*, Memoir **75**, 45-81.

Hallam, A. 1978. Eustatic Cycles in the Jurassic. *Palaeogeography, Palaeoclimatology, Palaeoecology*, **23**, 1-32.

Hammes, U., Hamlin, H.S. & Ewing, T.E. 2011. Geologic analysis of the Upper Jurassic Haynesville shale in east Texas and west Louisiana. *American Association of Petroleum Geologists Bulletin*, **95**(10), 1643-1666.

Heslop, D., McIntosh, G. & Dekkers, M. J. 2004. Using time- and temperature-dependent Preisach models to investigate the limitations of modeling isothermal remanent magnetization acquisition curves with cumulative log Gaussian functions. *Geophysical Journal International*, **157**, 55–63.

Hesselbo, S.P., Grocke, D.R., Jenkyns, H.C., Bjerrum, C.J., Farrimond, P., Morgans Bell, H.S. & Green, O.R. 2000. Massive dissociation of gas hydrate during Jurassic oceanic anoxic event. *Nature*, **406**, 392-395.

Hirt, A.M., Banin, A. & Gehring, U.A. 1993. Thermal generation of ferromagnetic minerals from iron-enriched smectites. *Geophysical Journal International*, **115**, 1161-1168.

Jackson, M. & Solheid, P. 2010. On the quantitative analysis and evaluation of magnetic hysteresis data. *Geochemistry Geophysics Geosystems*, **11**, Q04Z15, doi:10.1029/2009GC002932.

Jackson, M. & Van der Voo, R. 1985. Drilling-induced remanence in carbonate rocks: occurrence, stability and grain-size dependence. *Geophysics Journal of the Royal Astronomical Society*, **81**, 75-87.

Jenkyns, H.C., Jones, C.E., Grocke, D.R., Hesselbo, S.P. & Parkinson, D.N. 2002. Chemostratigraphy of the Jurassic system: applications, limitations and implications of palaeoceanography. *Journal of the Geological Society, London*, **159**, 351-378.

Katz, B., Elmore, R. D., Cogoini, M. & Ferry, S. 1998. Widespread chemical remagnetization: orogenic fluids or burial diagenesis of clays?, *Geology*, **26**(7), 603–606.

Kruiver, P. K., Dekkers, M. J. & Heslop, D. 2001. Quantification of magnetic coercivity components by the analysis of acquisition curves of isothermal remanent magnetization. *Earth and Planetary Science Letters*, **189**, 269–276.

Land, L.S., Mack, L.E., Milliken, K.L. & Lynch, F.L. 1997. Burial diagenesis of argillaceous sediment, south Texas Gulf of Mexico sedimentary basin: a reexamination. *Geological Society of America Bulletin*, **109**(1), 2-15.

Lowrie, W. 1990. Identification of ferromagnetic minerals in a rock by coercivity an unblocking temperature properties, *Geophysical Research Letters*, **17**, 159–162.

Machel, H. G. 1987. Saddle dolomite as a by-product of chemical compaction and thermochemical sulfate reduction. *Geology,* **15**, 936-940.

Machel, H. G. & Burton, E. A. 1991. Causes and spatial distribution of anomalous magnetization in hydrocarbon seepage environments. *American Association of Petroleum Geologist Bulletin*, **75**(12), 1864–1876.

Machel, H.G. 1998. Gas souring by thermochemical sulfate reduction at 140 C: discussion. *American Association of Petroleum Geologists Bulletin*, **82**, 1870-1873.

Machel, H. G. 2001. Bacterial and thermochemical sulfate reduction in diagenetic settings—old and new insights. *Sedimentary Geology*, **140**, 143–175.

Mancini, E.A., Li, P., Goddard, D.A., Ramirez, V. & Talukdar, S.C. 2008. Mesozoic Upper Jurassic-Lower Cretaceous) deep gas reservoir play, central and eastern Gulf coastal plain. *American Association of Petroleum Geologists Bulletin*, **92**(3), 283-308.

Manning, E.B. & Elmore, R.D. 2012. Rock magnetism and identification of remanence components in the Marcellus Shale, Pennsylvania. *Geological Society, London, Special Publications*, **371**, doi: 10.1144/SP371.9.

Manning, E.B. 2011. An integrated paleomagnetic, rock magnetic, and diagenetic study of the Marcellus shale within the Valley and Ridge Province of Pennsylvania and West Virginia [Master's Thesis]. United States—Oklahoma: The University of Oklahoma.

McArthur, J. M., Howarth, R. J. & Bailey, T. R. 2001. Strontium isotope stratigraphy: LOWESS Version 3; best fit to the marine Sr-isotope curve for 0–509 Ma and accompanying look-up table for deriving numerical age. *Journal of Geology*, **109**(2), 155–170.

Moore, G.T, Sloan, L.C., Hayashida, D.N. & Umrigar, N.P. 1992. Paleoclimate of the Kimmeridgian/Tithonian (Late Jurassic) world: II. Sensitivity tests comparing three different paleotopographic settings. *Palaeogeography, Palaeoclimatology, Palaeoecology*, **95**, 229-252.

Norwood, E.M. & Brinton, L. 2001. Reexamination of Late Jurassic reef building in the East Texas Basin; a maturing gas play. *Gulf Coast Association of Geological Societies Transactions*, **51**, 259-271.

Parker, M., Buller, D., Petre, E. & Dreher, D. 2009. Haynesville shale-petrophysical evaluation. From Society of Petroleum Engineers Rocky Mountain Petroleum Technology Conference. Denver, Colorado, United States. April 14-16 2009.

Peters, C. & Dekkers, M. J. 2003. Selected room temperature magnetic parameters as a function of mineralogy, concentration and grain size. *Physics and Chemistry of the Earth*, **28**, 659–667.

Pierce, J. W., Goussev, S. A., Charters, R. A., Ambercrombie, H. J. & DePaoli, G. R. 1998. Intrasedimentary magnetization by vertical fluid flow and exotic geochemistry. *The Leading Edge*, **17**, 89–92.

Reynolds, R.L., Goldhaber, M.B. & Tuttle, M.L. 1993. Sulfidization and magnetization above hydrocarbon reservoirs. *In:* Aissaoui, D.M. McNeill, D.F. & Hurley, N.F. (eds) *Applications of Paleomagnetism to Sedimentary Geology.* Society Economic Geologists & Mineralogists, Tulsa, Special Publications, **49**, 167-179.

Salvador, A. 1987. Late Triassic-Jurassic paleogeography and origin of Gulf of Mexico Basin. *American Association of Petroleum Geologists Bulletin*, **71**(4), 419-451.

Scholle, P.A & Ulmer-Scholle, D.S. 2003. A color guide to the petrography of carbonate rocks: grains, textures, porosity, diagenesis. *American Association of Petroleum Geologists*, Memoir **77**, 377.

Sellwood, B.W., Valdes, P.J. & Price, G.D. 2000. Geological evaluation of multiple general circulation model simulations of Late Jurassic palaeoclimate. *Palaeogeography, Palaeoclimatology, Palaeoecology*, **156**, 147-160.

Spain, D.R. & Anderson, G.A. 2010. Controls on reservoir quality and productivity in the Haynesville shale, Northwestern Gulf of Mexico Basin. *Gulf Coast Association of Geological Societies Transactions*, **60**, 657-688.

Stanley, S.M., Ries, J.B. & Hardie, L.A. 2002. Low-magnesium calcite produced by coralline algae in seawater of Late Cretaceous composition. *Proceedings of the National Academy of Sciences of the United States of America,* **24**, 15323-15326.

Stueber, A.M., Pushkar, P. & Hetherington, E.A. 1984. A strontium isotopic study of Smackover brines and associated solids, southern Arkansas. *Geochemica et Cosmochemica Acta*, **48**, 1637-1649.

Suk, D., Van der Voo, R. & Peacor, D.R. 1990. Scanning and transmission electron microscope observations of magnetite and other iron phases in Ordovician carbonates from east Tennessee. *Journal Geophysical Research*, **95**, 12327-12336.

Symons, D.T.A., Enkin, R. & Cioppa, M.T. 1999. Paleomagnetism in the Western Canada Sedimentary Basin: dating fluid flow and deformation events. *Bulletin of Canadian Petroleum Geology*, **47**, 534-547.

Torsch, W.C. 2012. Thermal and pore pressure history of the Haynesville shale in north Louisiana: a numerical study of hydrocarbon generation, overpressure, and natural hydraulic fractures [Master's Thesis]. United States—Louisiana. Louisiana State University.

Tourtelot, H.A. 1979. Black shale-its deposition and diagenesis. *Clays and Clay Minerals*, **27**(5), 313-321.

Van Alstine, D.R. & Butterworth, J.E. 2002. Paleomagnetic core-orientation helps determine the sedimentological, paleostress, and fluid-migration history in the Maracaibo Basin, Venezuela. Available at web: http://www.appliedpaleomagnetic.com.

Van Der Voo, R. & Watts, D.R. 1978. Paleomagnetic results from igneous and sedimentary rocks from the Michigan basin borehole. *Journal of Geophysical Research,* **83**, 5844-5848.

Zechmeister, M.S., Pannalal, S. & Elmore, R.D. 2012. A multidisciplinary investigation of multiple remagnetizations within the Southern Canadian Cordillera, SW Alberta and SE British Columbia. *In:* Elmore, R.D., Muxworthy, A.R., Aldana, M. & Mena, M. (eds) *Remagnetization and Chemical Alteration of Sedimentary Rocks.* Geological Society London, Special Publications, **371**, first published online 22 August 2012, http://dx.doi.org/10.1029/2002JB002213

Zijderveld, J.D.A. 1967. A.C. demagnetization of rocks: Analysis of results. *In*: Collinson, D. E., Creer, K. M. & Runcorn, S. K. (eds) 1967. *Methods in Paleomagnetism*, 254–286.

Appendix

A. Coleman Gas Unit 1-6 core description and well log

Legend

Symbol	Meaning
	Few shell fragments
	Shelly zone
	Veins
	Cephalopod/bivalve
	Breccia
	Laminations (minor)
	Laminations (highly fissle)
	Burrows/bioturbation
	Pyrite
	Calcite filled shells
	Concretions
	Silica grains
	Missing section
	Rubble

Gray Scale

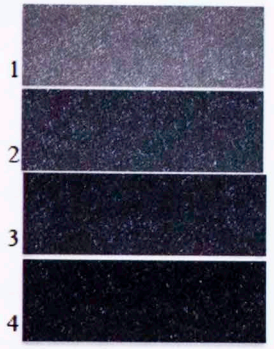

Facies

Nonlaminated Mudstone (varies from siliceous to calcareous)

Laminated Mudstone (varies from siliceous to calcareous)

Burrowed Mudstone (based upon thin section analysis)

Dolostone

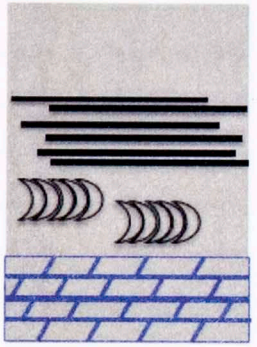

Depth (ft)	Profile	Gray Scale	Facies					Allochems	Comments	Thin Section Analysis
			LSM	NLSM	LCM	NLCM	BM			
10800										
10802						x				
10804						x		Shell fragments present	Detrital carbonate clast with various minerals present(see text for list)	CG-A(10803'3") Shale w/ detrital carbonate and dark lenticular lenses
10806						x				
10808						x		Shell fragments present		CG-1(10807'10")shale with detrital carbonate and minor silica grains
10810						x				
10812						x			Large vein has minor veins w/in(mostly silica filled and minor calcite)	CG-B(10810'4")
10814						x				
10816						x		Shell fragments present		
10818						x				
10820						x				
10822										CG-2 (10822') dolostone
10824						x				
10826						x				
10828						x		Shell fragments present		
10830						x				
10832									Breccia filled with pyrite and barite	CG-3A/B(10830'7")Pyrite along edges, barite main mineral, dolomite also
10834						x				
10836						x		Shell fragments present		
10838						x		Cephalopods present		
10840						x		minor shell frags with calcite precip.		CG-C(10839'8")Shale w/ minor detrital silca and dark lenticular lenses
10842						x		Cephalopods present		
10844						x		Shell fragments present		
10846						x				
10848						x				
10850						x		Cephalopods present		

Depth (ft)	Profile	Gray Scale	Facies					Allochems	Comments	Thin Section Analysis
			LSM	NLSM	LCM	NLCM	BM			
10852	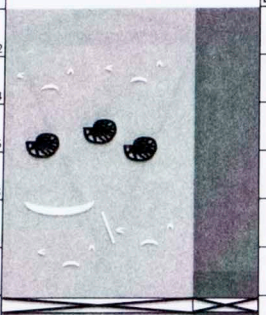					x				
10854						x				
10856						x		Cephalopods present		
10858						x				CG-6(10857')minor shale, detrital carbonate prevalent
10860						x				
10862						x				
10864						x		Cephalopods present		
10866						x				
10868						x		Shell fragments present		
10870						x				
10872	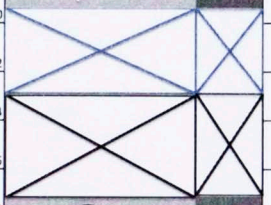									
10874										
10876										
10878	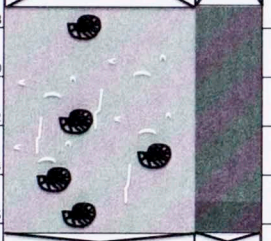					x		Cephalopods present		
10880						x				
10882						x				
10884						x		Cephalopods present		
10886						x		Cephalopods present		
10888						x				
10890	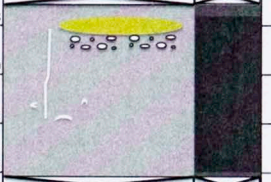					x			Sulfur-rich nodule with silica grains present on base	
10892						x				
10894				x		x				CG-7(10893'7") shale with detrital carbonate and silica grains. Minor burrows
10896	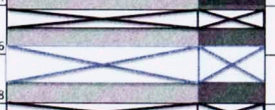									
10898						x				
10900										
10902	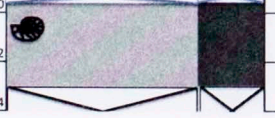					x		Cephalopods present		
10904										

Depth (ft)	Profile	Gray Scale	Facies					Allochems	Comments	Thin Section Analysis
			LSM	NLSM	LCM	NLCM	BM			
10906	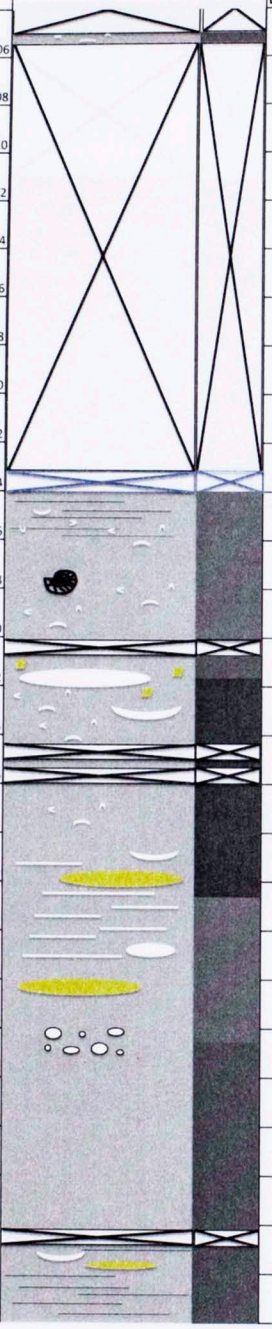									
10908										
10910										
10912										
10914										
10916										
10918										
10920										
10922										
10924										
10926					x					
10928						x		Cephalopods present		
10930						x				
10932				x		x		Large bivalves	Carbonate concretion and cubic pyrite present	CG-8(10933'4") shale with detrital carbonate and silica, minor burrows
10934				x		x		Brachiopods	Shale with detrital carbonate and minor silica. Large shell calcite filled.	CG-9(10934'6")large brachiopod with impunctate structure
10936				x		x				
10938				x		x				
10940					x				Sulfur-rich concretion @ 10940'4" and calcite filled shell lense	
10942					x				Horizontal veins present throughout 4 ft interval. Carbonate concretion	
10944					x					
10946						x			Sulfur-rich concretion	
10948				x					Silica grains visible	
10950				x						
10952						x			Shale with detrital carbonate	CG-10(10951'4") Large pyrite rhombs and a few have flourite replacement
10954						x				
10956				x					Sulfur-rich concretion and calcite filled shell lense. Minor laminations	CG-11(10954'7") Dark shale with silica grains. Minor silica filled veins
10958				x		x			Minor laminations	CG-12(10956'10") Vein has

Depth	Profile	Gray Scale	Facies					Allochems	Comments	Thin Section Analysis
(ft)			LSM	NLSM	LCM	NLCM	BM			
10960	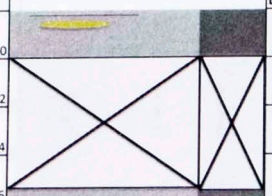					x			Sulfur-rich concretion	large amounts of pyrite. Shale with detrital carbonate and silica
10962										
10964										
10966										
10968						x			Calcite filled lenses and carbonate filled horizontal vein	
10970						x				
10972				x					Silica grains present alongside shell fragments	
10974				x					Calcite filled shell lense ~3cm	CG-13(10973'8") Shale with detrital silica and minor carbonate. Veins have micrite and dolomite
10976				x						
10978				x					Shale with detrital silica grains	CG-14(10975'9") Large bivalves and crinoids present
10980				x					Vertical fracture filled with calcite. Minor laminations	
10982				x					Dark shale with detrital silica and minor carbonate	CG-15(10981'6") Wavy lenses filled with baroque dolomite
10984				x						
10986				x						
10988				x				Calcite filled bivalves	Calcite filled shells and silica grains	
10990				x					Horizontal calcite filled vein	
10992				x						
10994						x		Shelly zone, bivalves and shell fragments		
10996						x				
10998						x				
11000						x				
11002						x		Bivalve lenses	pyrite concretions with carbonate@11002'	
11004				x				Shell has silica on rim and two calcite precipitation events	Minor laminations	CG-16(11003'8") Shale with detrital silica and minor carbonate
11006				x				Shell fragments-calcite and baroque dolomite(impunctate structure)		CG-17(11004'1")Shale with detrital silica and minor carbonate
11008				x				Dense shell interval, bivalves		
11010				x						
11012				x						

Depth (ft)	Profile	Gray Scale	Facies					Allochems	Comments	Thin Section Analysis
			LSM	NLSM	LCM	NLCM	BM			
11014	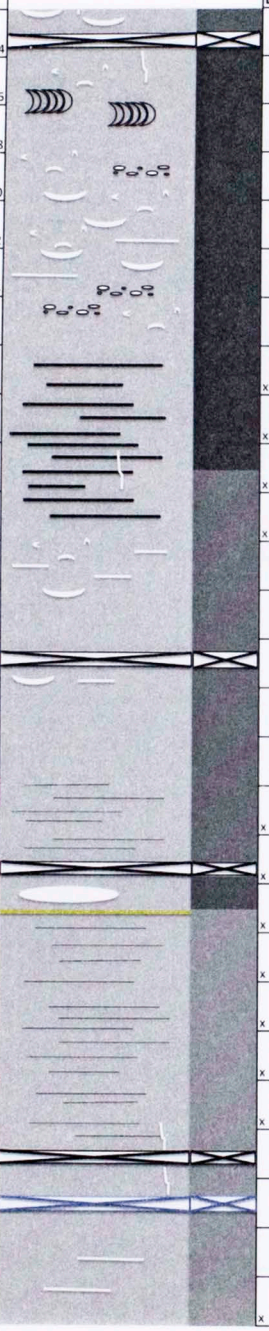			x						
11016							x	bivalve fragments		CG-18(11015') Shale with minor detrital silica and carbonate. Burrows
11018							x			CG-19(11016'6")Shale with detrital carbonate. Burrows throughout
11020						x				
11022						x				
11024						x				
11026				x				Shells have silica rim and calcite and pyrite replacement within	Minor lenticular silica veins	CG-20(11025'7")Shale with detrital silica and minor carbonate
11028			x							
11030			x							CG-21(11029'7")Shale and detrital silica
11032			x							
11034			x							
11036							x			
11038							x			
11040							x	Large fragmented bivalves(calcite, dolomite, pyrite)	Greenish-brown sphalerite present (replacement of pyrite)	CG-22(11039'2") Mudstone, minor detrital silica
11042							x	Shell contains pyrite, sphalerite and baroque dolomite		CG-23(11040'6")
11044							x			
11046			x							
11048			x							
11050			x						carbonate concretion @ 11048' Sulfur-rich vein	
11052			x					Shells with two stages of calcite precip.	Fracturing and pyritization interpreted as occuring syndepositionally. Barite present	CG-24(11050'4") Mudstone with detrital silica
11054			x						minor laminations and few allochems	
11056			x							
11058			x					Shell has fibrous calcite and minor pyrite	minor laminations and few allochems	CG-25(11056'9") Shale with detrital silica
11060				x						
11062				x					large anastomizing vein has visible porosity. Interpreted as post burrowing	CG-26(11060'6") Shale with detrital silica and burrows
11064				x						
11066			x							

Depth	Profile	Gray Scale	Facies					Allochems	Comments	Thin Section Analysis
(ft)			LSM	NLSM	LCM	NLCM	BM			
11068	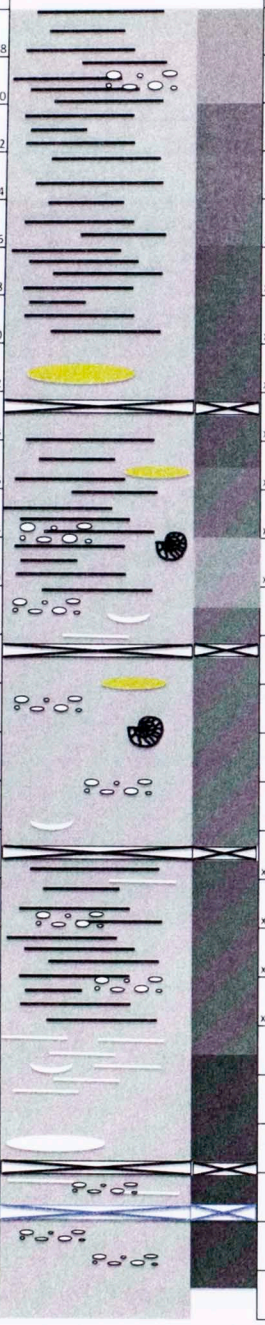		x						Laminated facies begins @11066'	CG-27(11067'7")Shale with micrite filled burrows
11070			x							
11072			x							
11074			x					Shell w/ silica on rim, micrite and calcite. Minor pyrite	dark brown burrows present	CG-28(11073'10")Shale w/ detrital silica and minor carbonate
11076			x							
11078			x					Bivalve frags. w/ blky calcite, one w/pyrite rim and impunctate structure		CG-29(11077'6") Shale w/ detrital silica and micrite filled burrows
11080			x							
11082			x						Sulfur-rich concretion	
11084			x						lenticular features may be burrows or clay flocculation particles	CG-30(11083'6")Shale w/ detrital silica and dark lenticular beds
11086			x						Silica vein cross-cuts sphalerite.Sulfur-rich/pyrite concretion @ 11085'3"	CG-31(11086'2") Shale w/ silica grains and lenticular lenses
11088			x							
11090			x							
11092				x						
11094				x				Shell frag w/ calcite precip. And pyrite on rim	Sulfur-rich concretion has minor calcite grains within	CG-32(11093'11") Shale with silica grains and minor veins
11096				x						
11098				x						
11100				x						
11102			x							
11104			x						Calcite concretion	CG-33(11103') Shale w/ detrital silica
11106			x					Mollusk shells partially replaced by pyrite	Burrows throughout matrix	CG-34(11105'1") organic rich shale w/ detrital silica
11108			x							
11110						x			Veined zone	
11112						x			One vein has silica grains	CG-35(11110'11")Dirty calcite w/ pyrite grading into v. silica-rich detritus
11114						x		One bivalve w/ calcite precip.	carbonate concretion. Burrows throughout matrix, micrite and mud filled	CG-35(11113'8")Shale w/ carbonate grains and minor silica
11116						x				
11118						x				
11120						x				

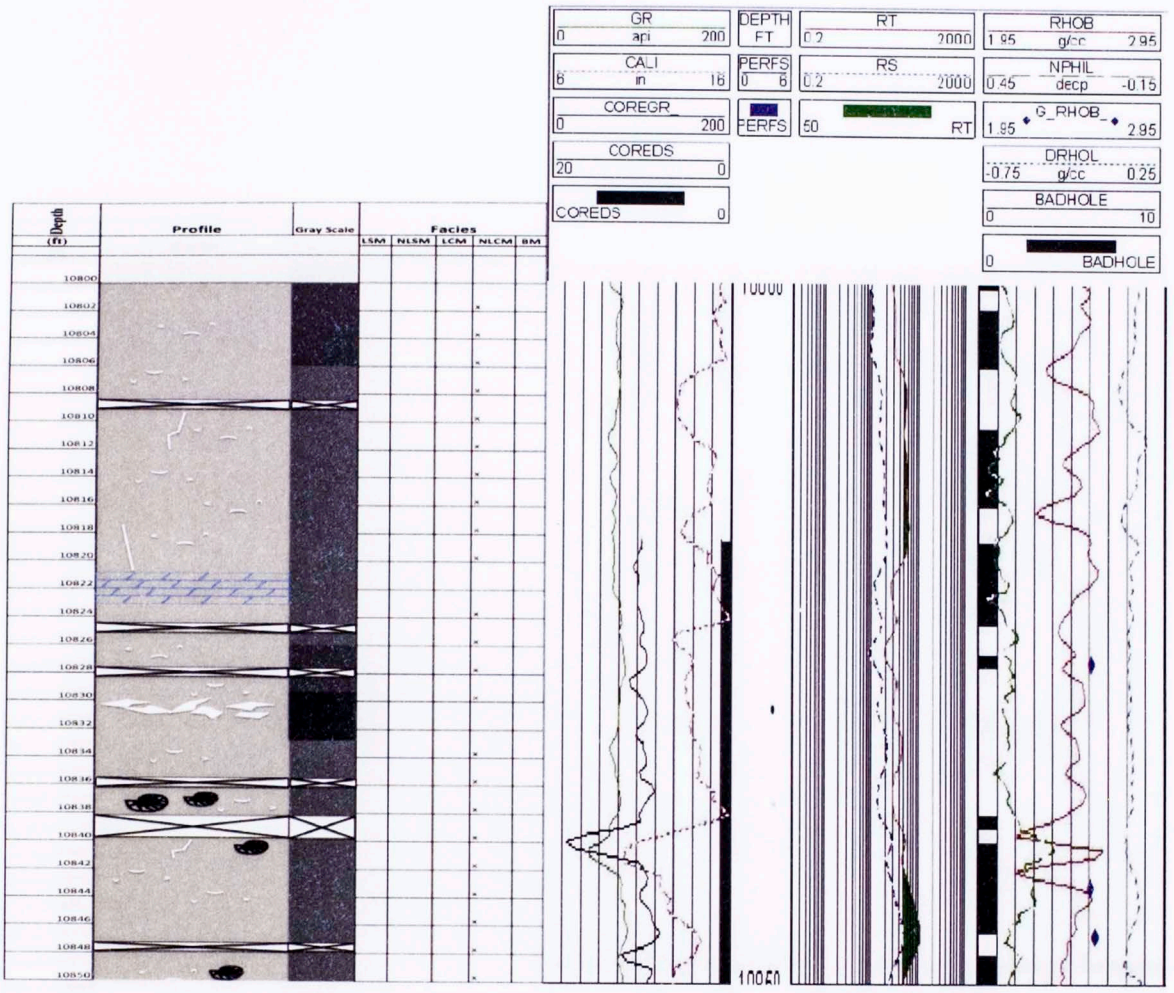
GR
0 api 200
CALI
6 in 16
COREGR
0 200
COREDS
20 0
COREDS 0
DEPTH
FT
PERFS
0 6
PERFS
RT
0.2 2000
RS
0.2 2000
50 RT
RHOB
1.95 g/cc 2.95
NPHIL
0.45 decp -0.15
G_RHOB
1.95 2.95
DRHOL
-0.75 g/cc 0.25
BADHOLE
0 10
0 BADHOLE
Depth (ft)
Profile
Gray Scale
Facies
LSM
NLSM
LCM
NLCM
BM
10800
10802
10804
10806
10808
10810
10812
10814
10816
10818
10820
10822
10824
10826
10828
10830
10832
10834
10836
10838
10840
10842
10844
10846
10848
10850

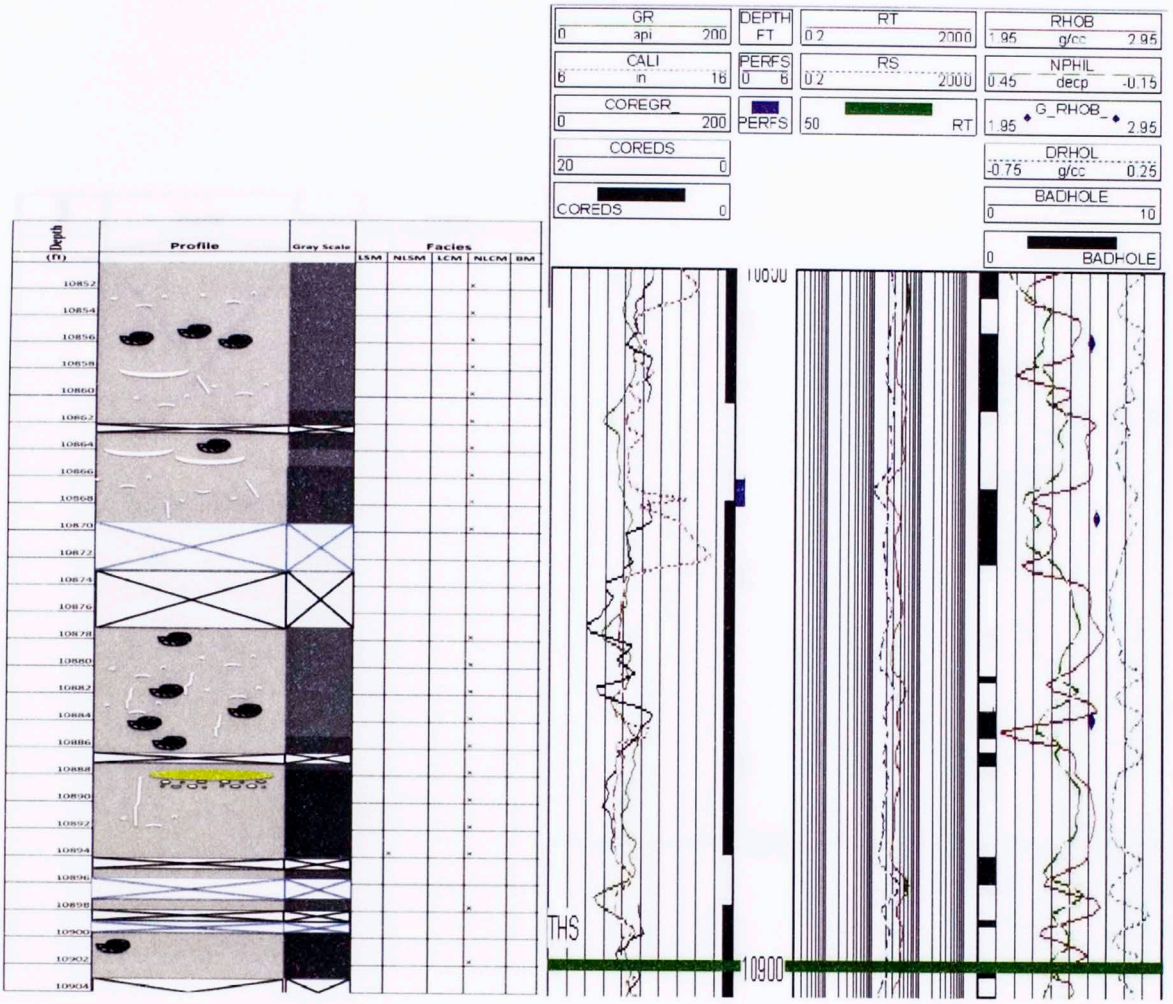
Depth
(ft)
Profile
Gray Scale
Facies
LSM
NLSM
LCM
NLCM
BM
10852
10854
10856
10858
10860
10862
10864
10866
10868
10870
10872
10874
10876
10878
10880
10882
10884
10886
10888
10890
10892
10894
10896
10898
10900
10902
10904
GR
0 api 200
CALI
6 in 16
COREGR_
0 200
COREDS
20 0
COREDS
0
DEPTH
FT
PERFS
0 6
PERFS
RT
0.2 2000
RS
0.2 2000
50 RT
RHOB
1.95 g/cc 2.95
NPHIL
0.45 decp -0.15
G_RHOB_
1.95 2.95
DRHOL
-0.75 g/cc 0.25
BADHOLE
0 10
0 BADHOLE
10900
THS
10900

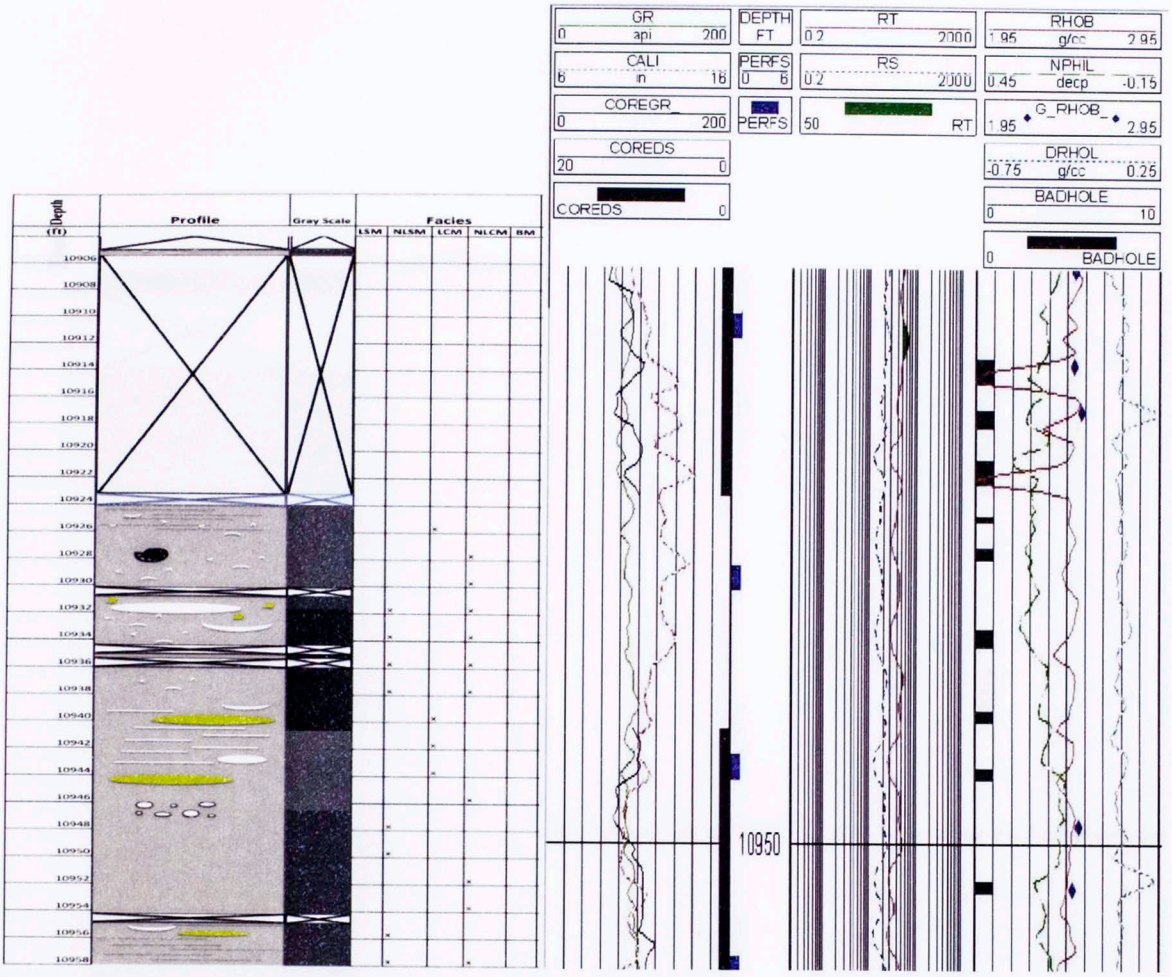
GR
0 api 200
CALI
6 in 16
COREGR
0 200
COREDS
20 0
COREDS 0
DEPTH
FT
PERFS
0 6
PERFS
RT
0.2 2000
RS
0.2 2000
50 RT
RHOB
1.95 g/cc 2.95
NPHIL
0.45 decp -0.15
G_RHOB_
1.95 2.95
DRHOL
-0.75 g/cc 0.25
BADHOLE
0 10
0 BADHOLE
Depth
(ft)
Profile
Gray Scale
Facies
LSM
NLSM
LCM
NLCM
BM
10906
10908
10910
10912
10914
10916
10918
10920
10922
10924
10926
10928
10930
10932
10934
10936
10938
10940
10942
10944
10946
10948
10950
10952
10954
10956
10958

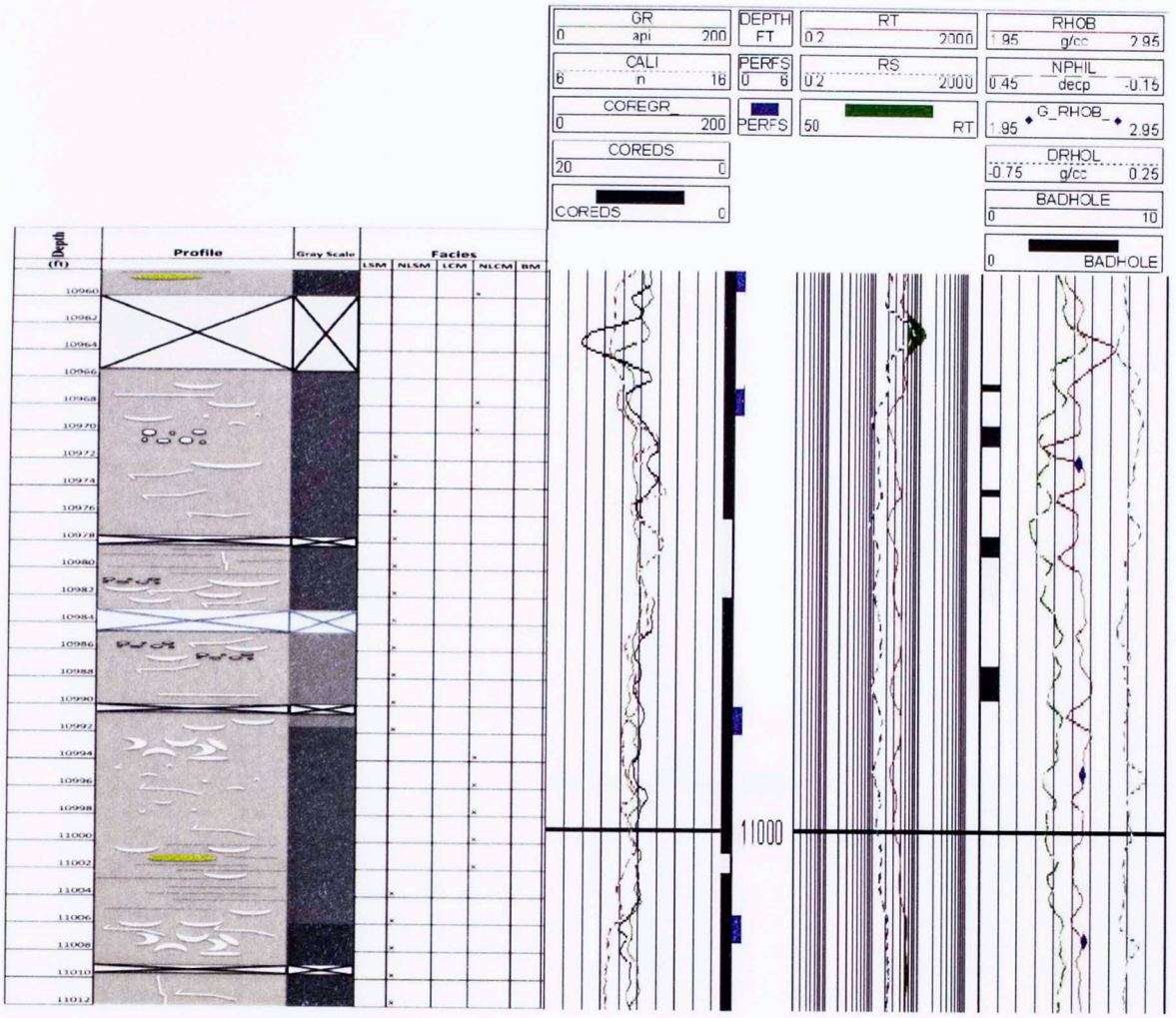
GR
0 api 200
CALI
6 in 16
COREGR
0 200
COREDS
20 0
COREDS 0
DEPTH
FT
PERFS
0 6
PERFS
RT
0.2 2000
RS
0.2 2000
50 RT
RHOB
1.95 g/cc 2.95
NPHIL
0.45 decp -0.15
G_RHOB
1.95 2.95
DRHOL
-0.75 g/cc 0.25
BADHOLE
0 10
0 BADHOLE
Depth
(ft)
Profile
Gray Scale
Facies
LSM
NLSM
LCM
NLCM
BM
10960
10962
10964
10966
10968
10970
10972
10974
10976
10978
10980
10982
10984
10986
10988
10990
10992
10994
10996
10998
11000
11002
11004
11006
11008
11010
11012
11000

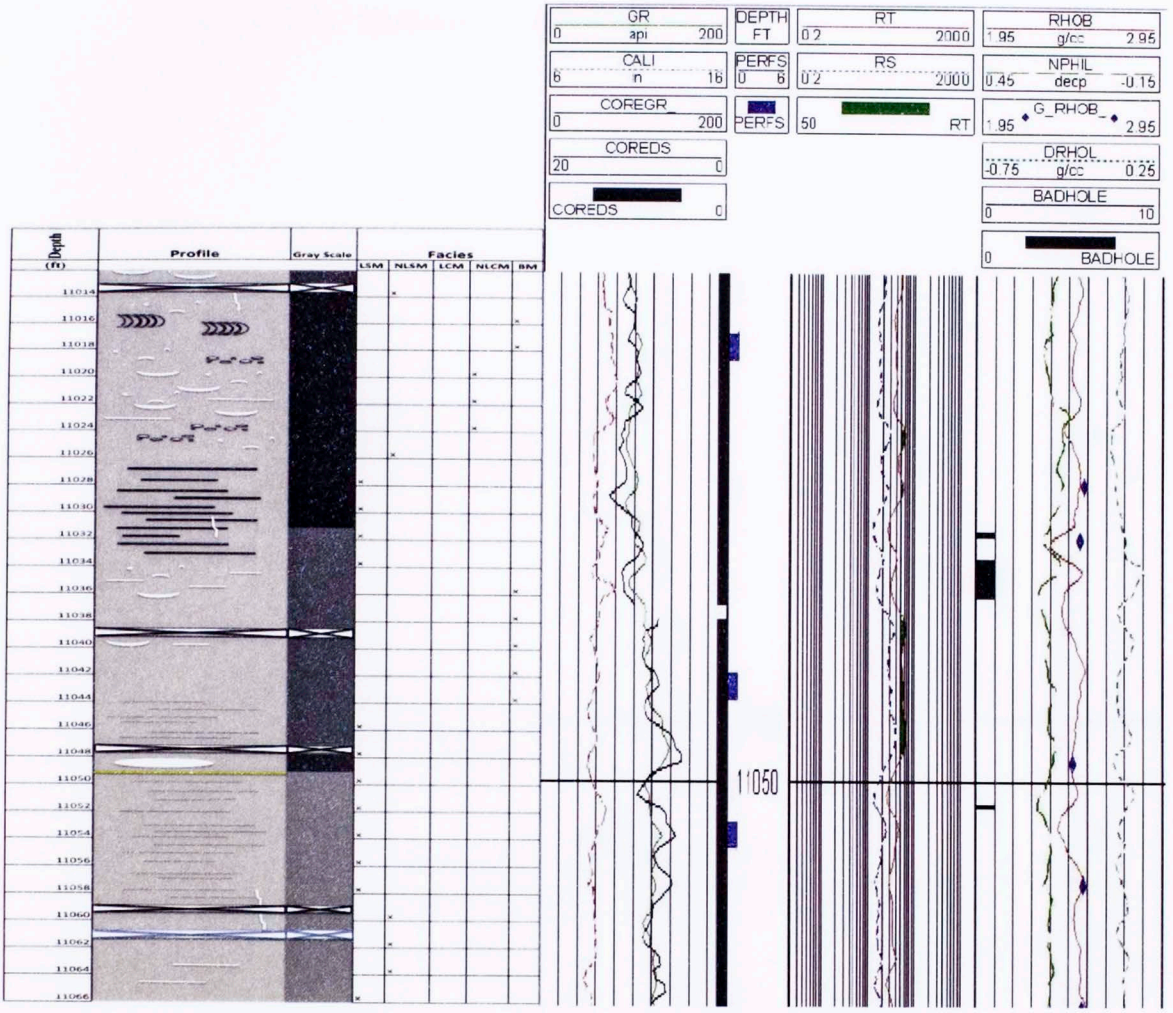
GR
0 api 200
CALI
6 in 16
COREGR
0 200
COREDS
20 0
COREDS 0
DEPTH
FT
PERFS
0 6
PERFS
RT
0.2 2000
RS
0.2 2000
50 RT
RHOB
1.95 g/cc 2.95
NPHIL
0.45 decp -0.15
G_RHOB
1.95 2.95
DRHOL
-0.75 g/cc 0.25
BADHOLE
0 10
0 BADHOLE
Depth
(ft)
Profile
Gray Scale
Facies
LSM
NLSM
LCM
NLCM
BM
11014
11016
11018
11020
11022
11024
11026
11028
11030
11032
11034
11036
11038
11040
11042
11044
11046
11048
11050
11052
11054
11056
11058
11060
11062
11064
11066
11050

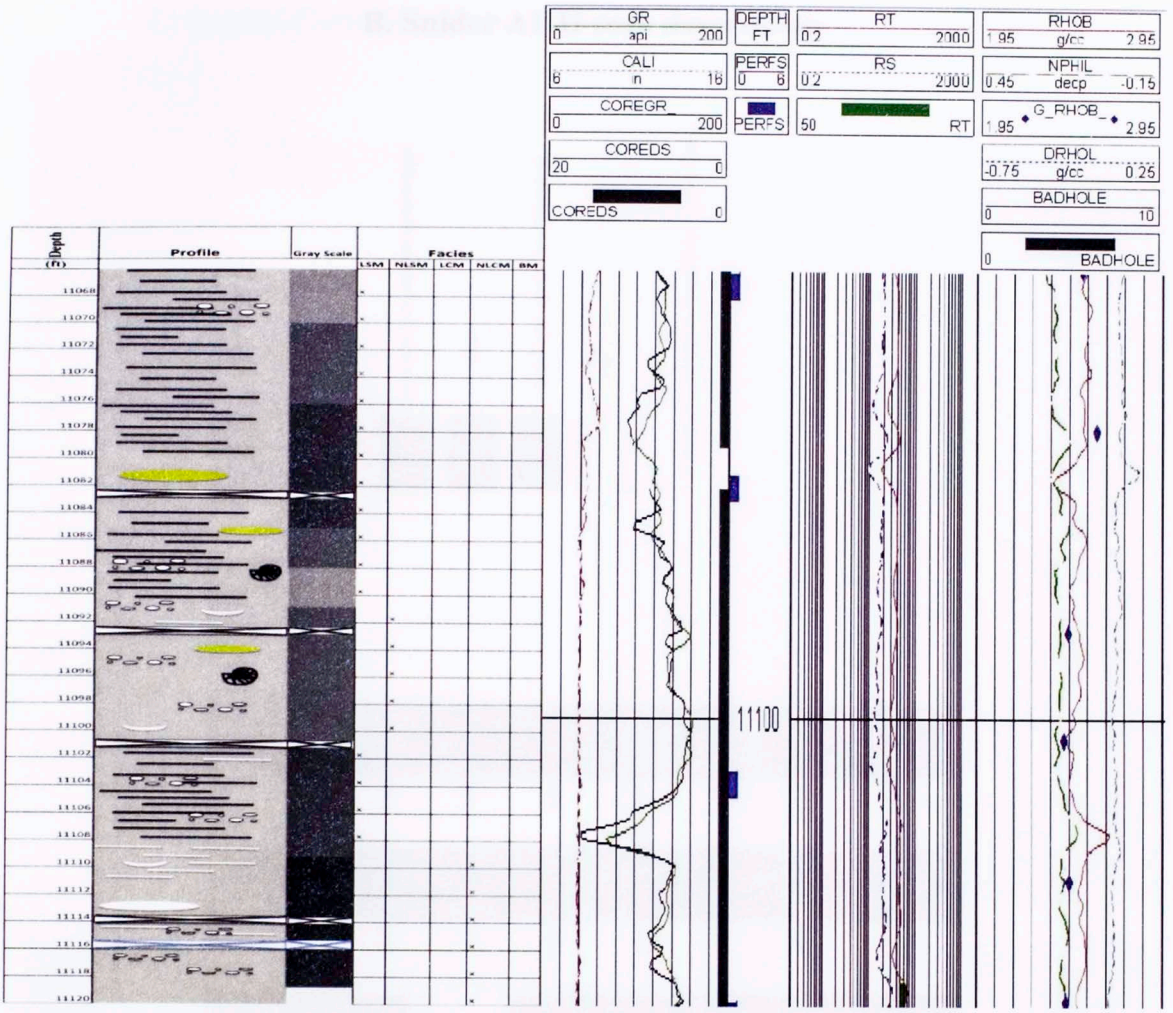
GR
0 api 200
CALI
6 in 16
COREGR
0 200
COREDS
20 0
CORED S 0
DEPTH
FT
PERFS
0 6
PERFS
RT
0.2 2000
RS
0.2 2000
50 RT
RHOB
1.95 g/cc 2.95
NPHIL
0.45 decp -0.15
G_RHOB_
1.95 2.95
DRHOL
-0.75 g/cc 0.25
BADHOLE
0 10
0 BADHOLE
Depth (ft)
Profile
Gray Scale
Facies
LSM
NLSM
LCM
NLCM
BM
11068
11070
11072
11074
11076
11078
11080
11082
11084
11086
11088
11090
11092
11094
11096
11098
11100
11102
11104
11106
11108
11110
11112
11114
11116
11118
11120
11100

B. Snider A1-H core description

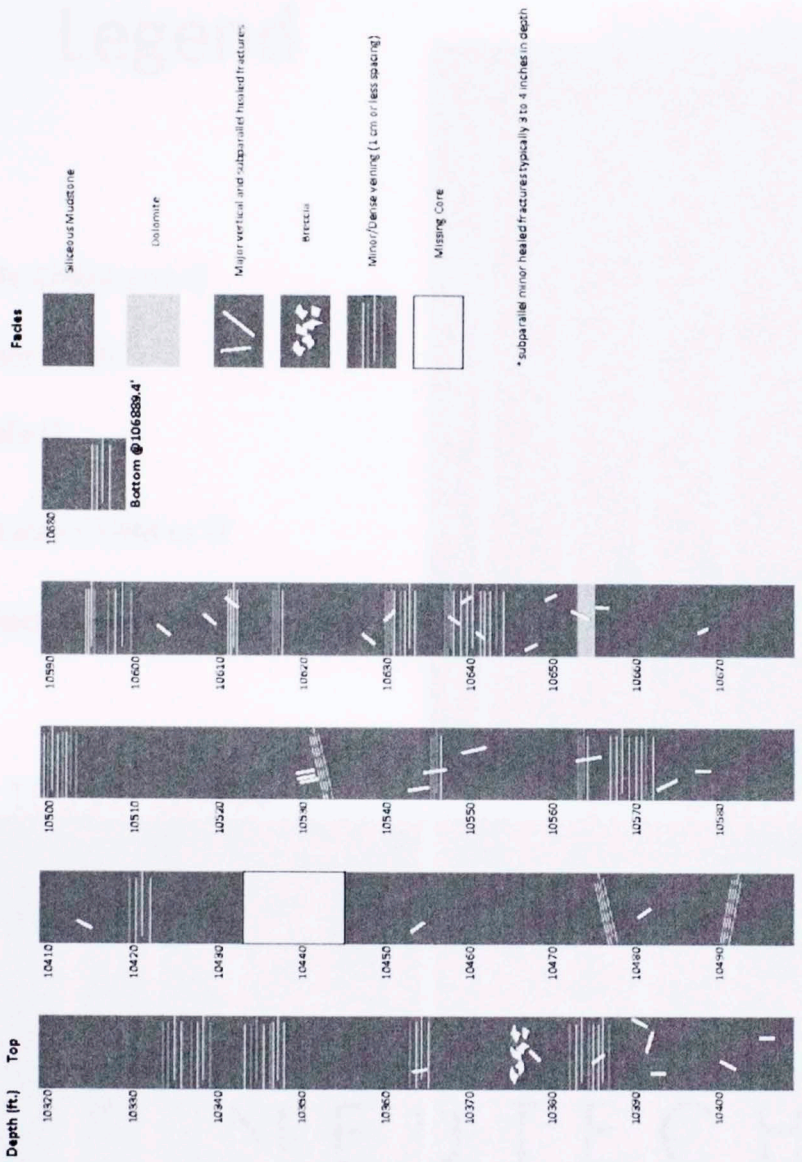

C. Snider Core photos showing magnetism correlation to veins

Legend

- Stable ChRM and IT
- Stable ChRM
- Stable IT
- No stable ChRM or IT

TS Thin Section analysis @ location

10320-10332

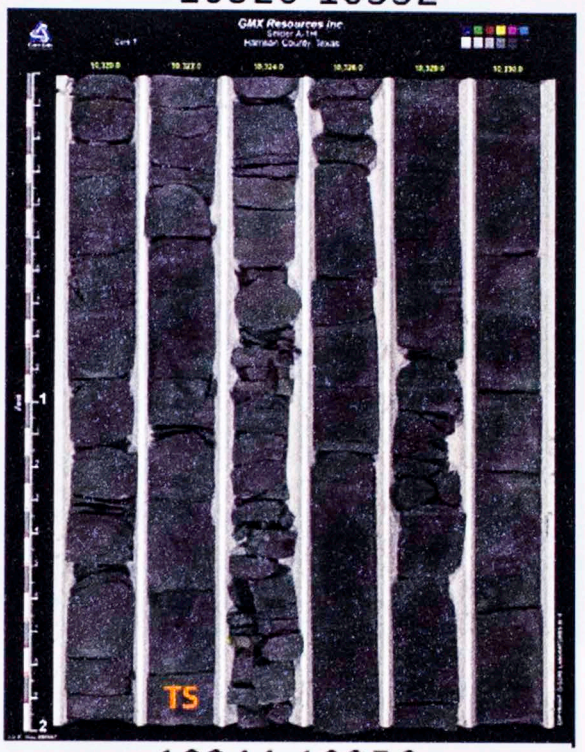

10332-10344

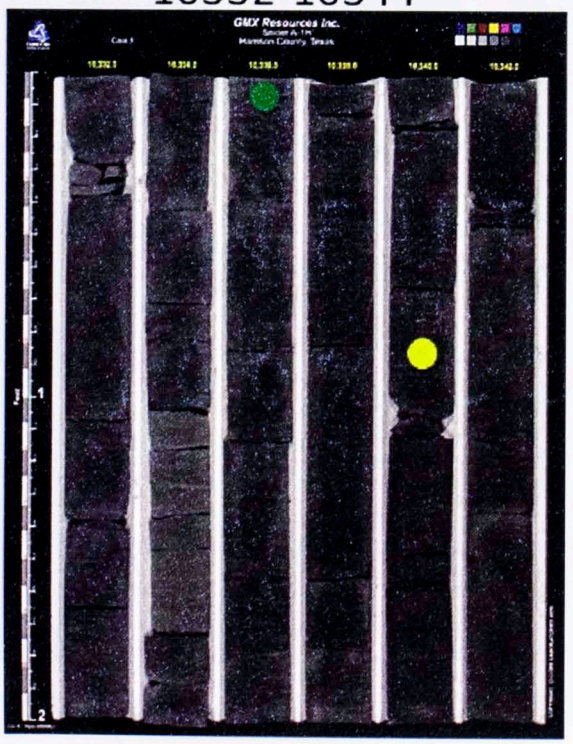

10344-10356

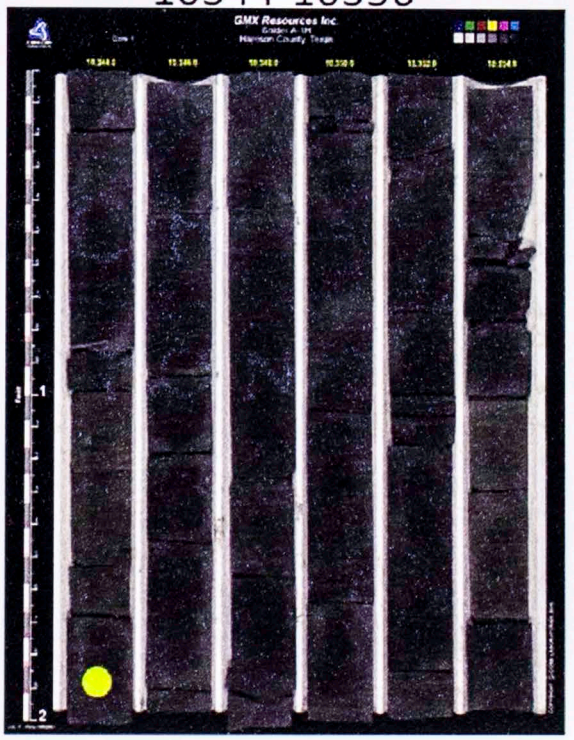

10356-10368

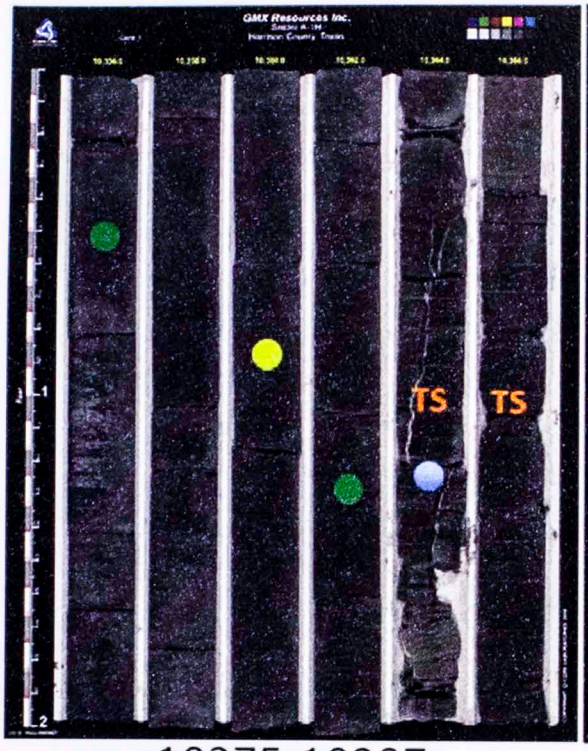

10368-10372

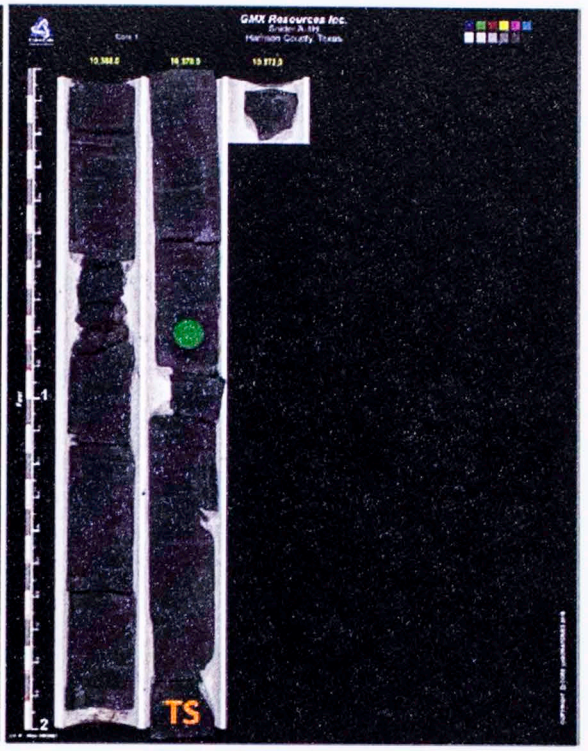

10375-10387

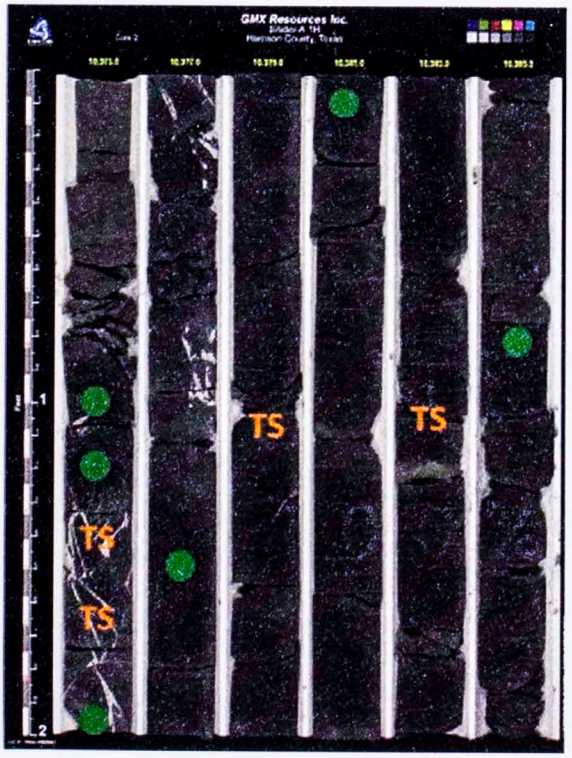

10387-10399

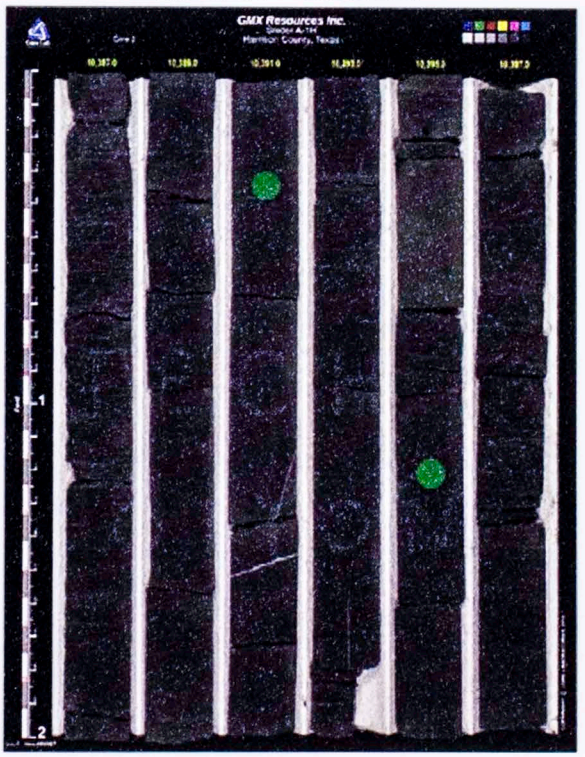

10399-10411

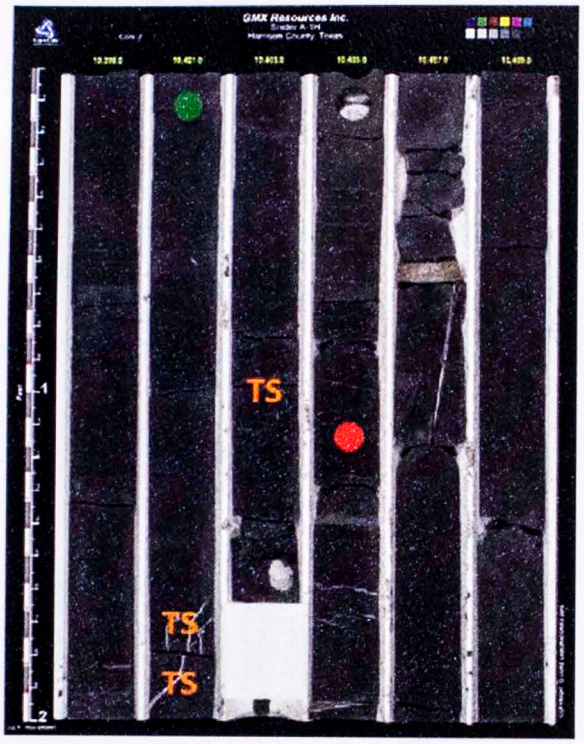

10411-10423

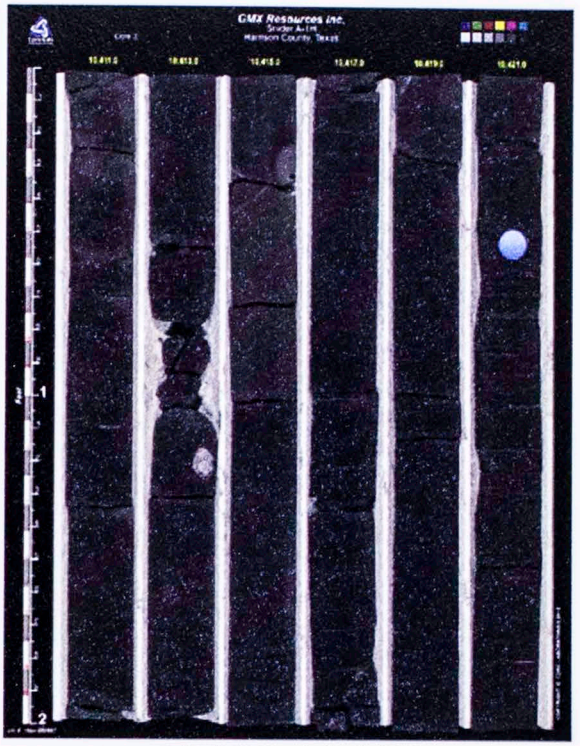

10423-10424.7

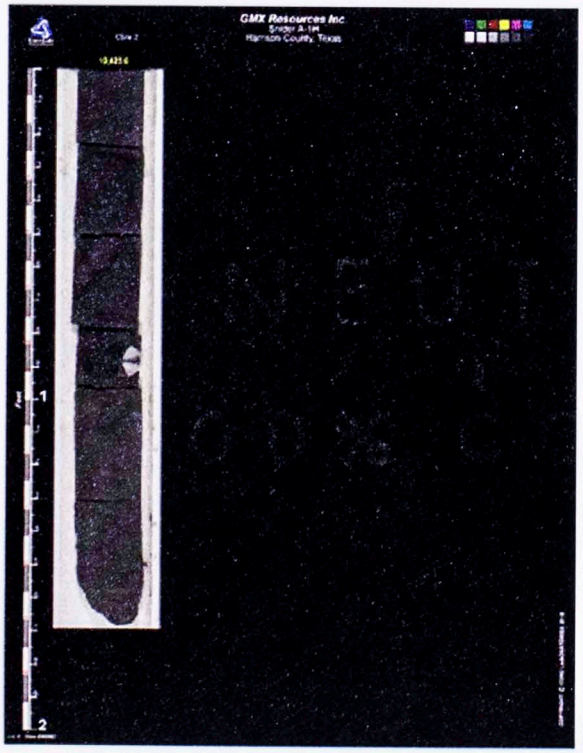

10435-10447

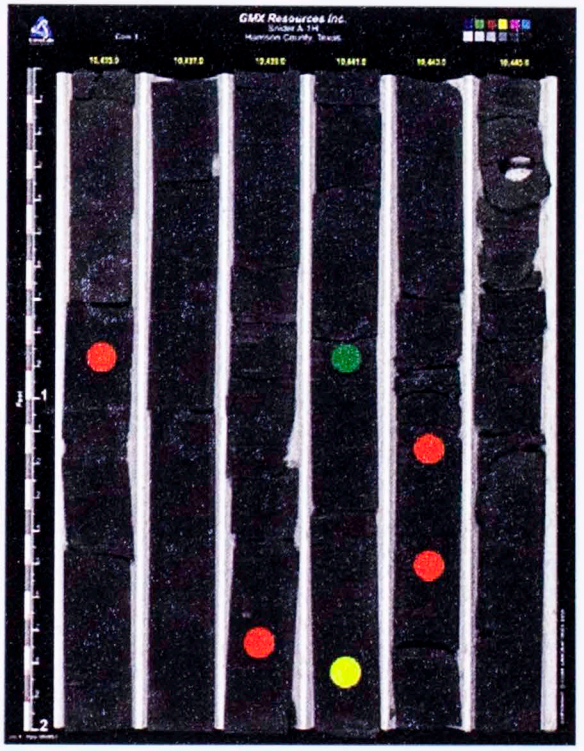

10447-10459

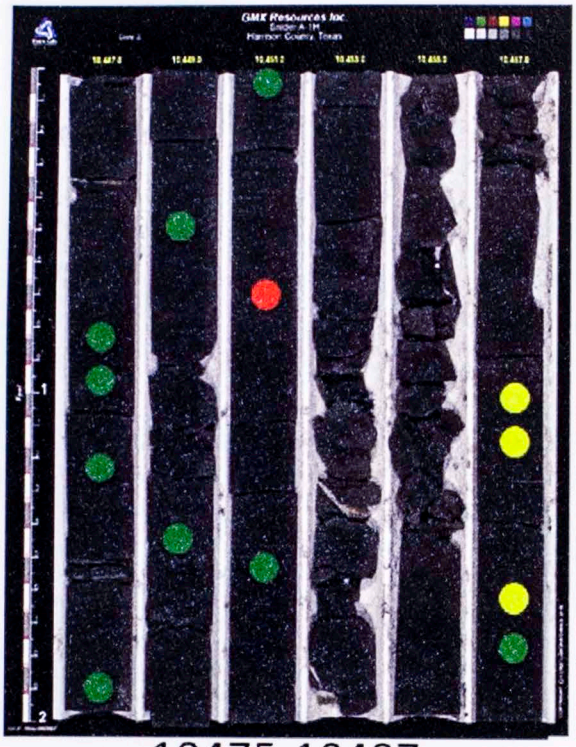

10459-10463.4

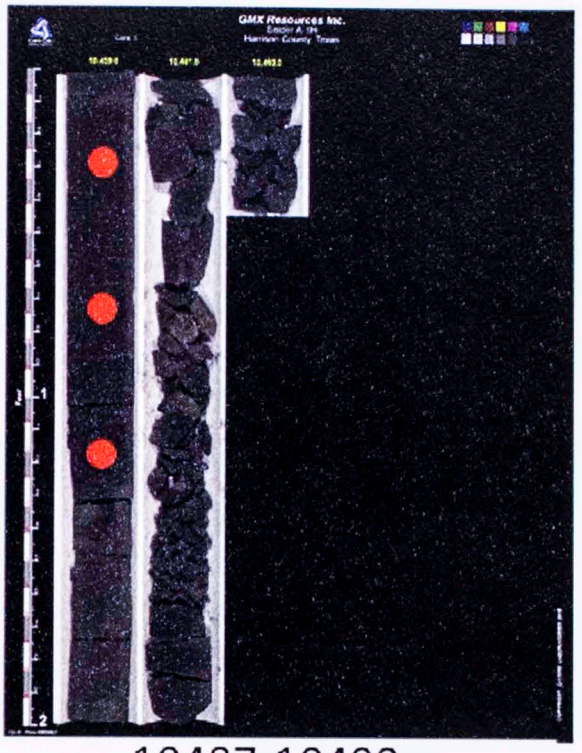

10475-10487

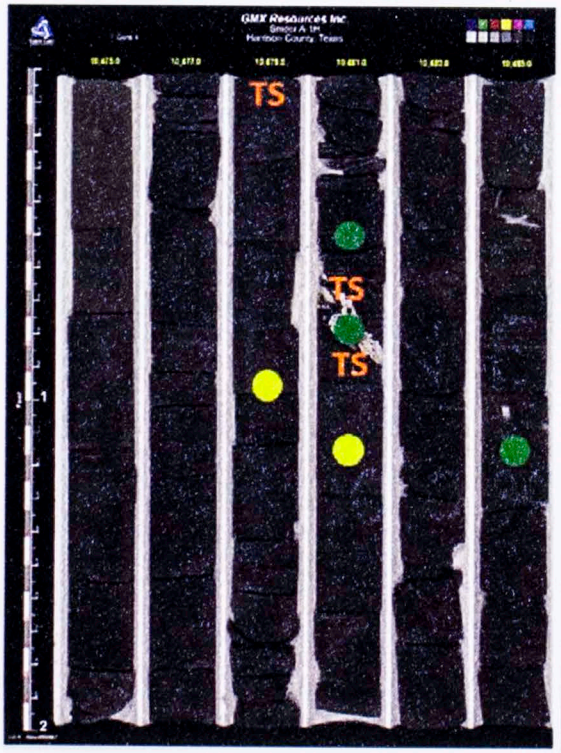

10487-10499

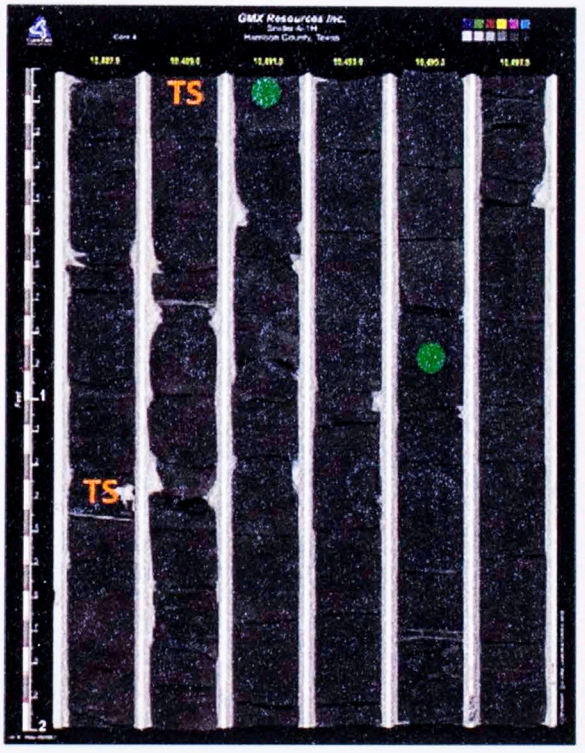

10499-10511

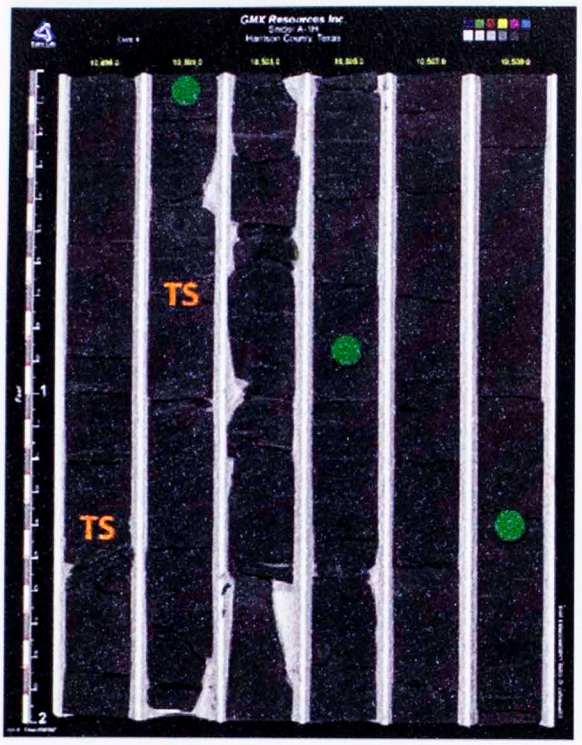

10511-10523

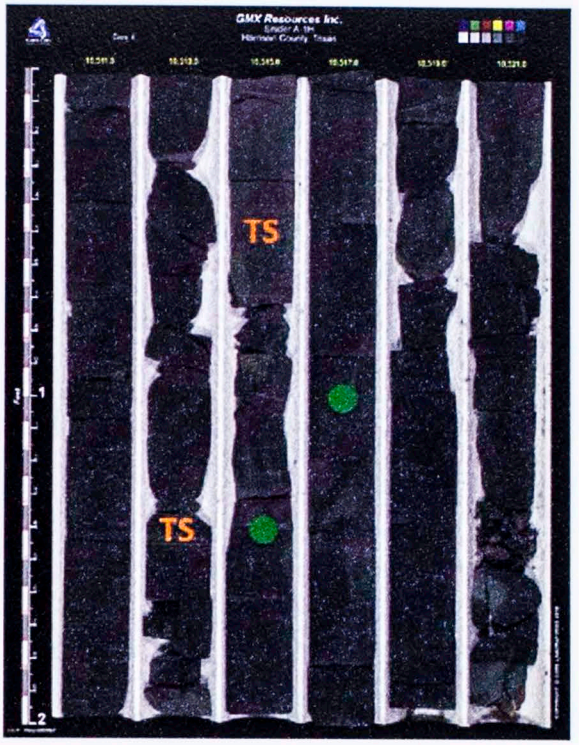

10523-10528.1

10530-10542

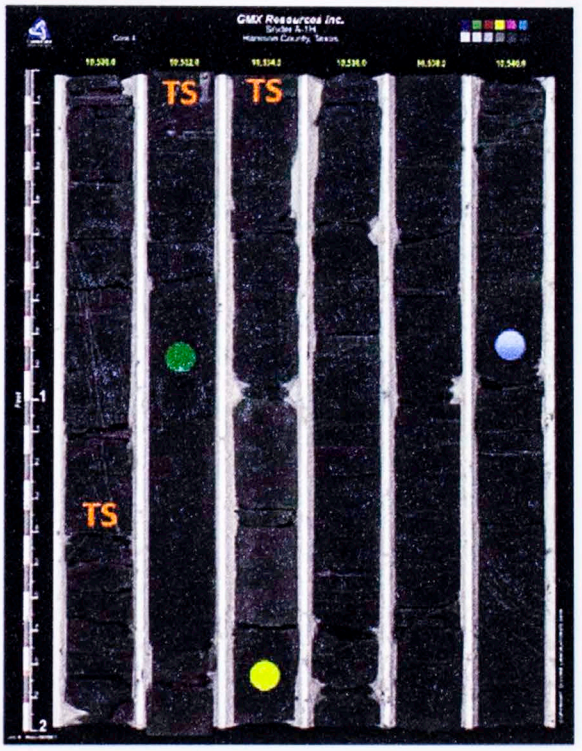

10542-10554

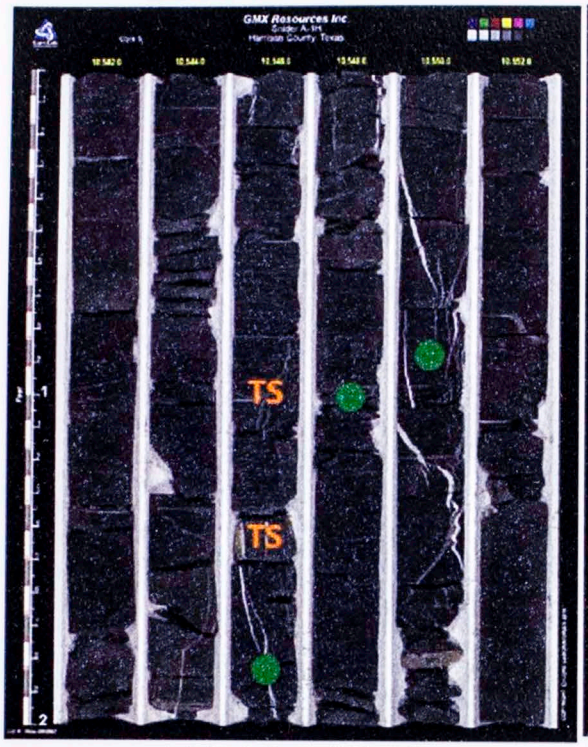

10554-10566

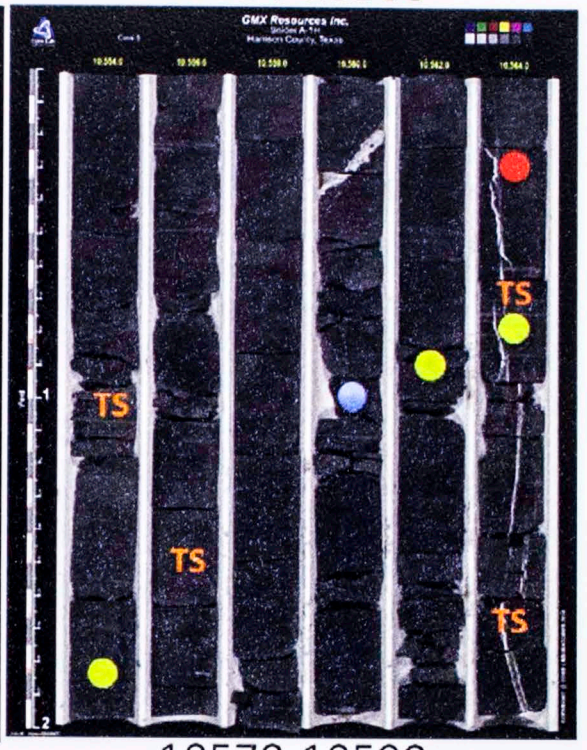

10566-10578

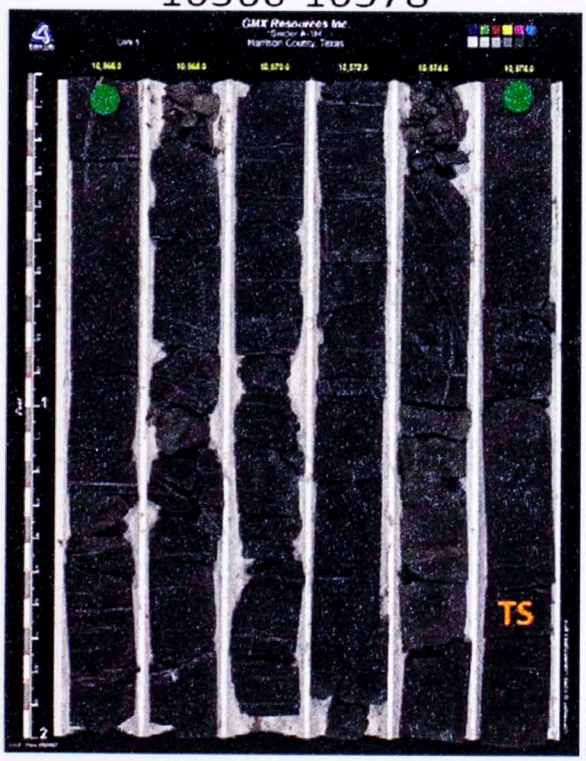

10578-10590

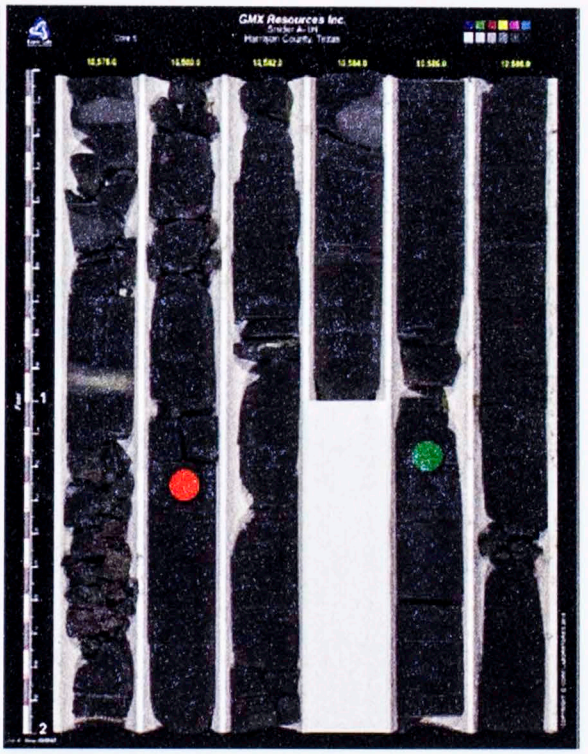

10590-10594.8

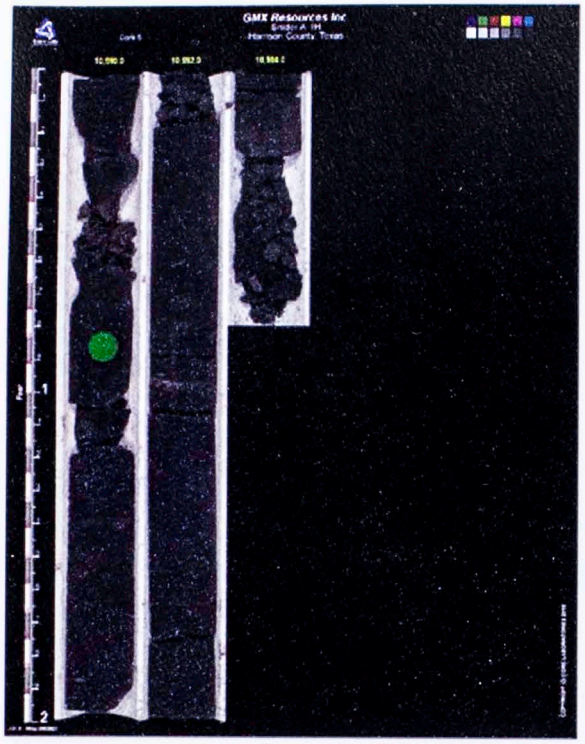

10595-10607

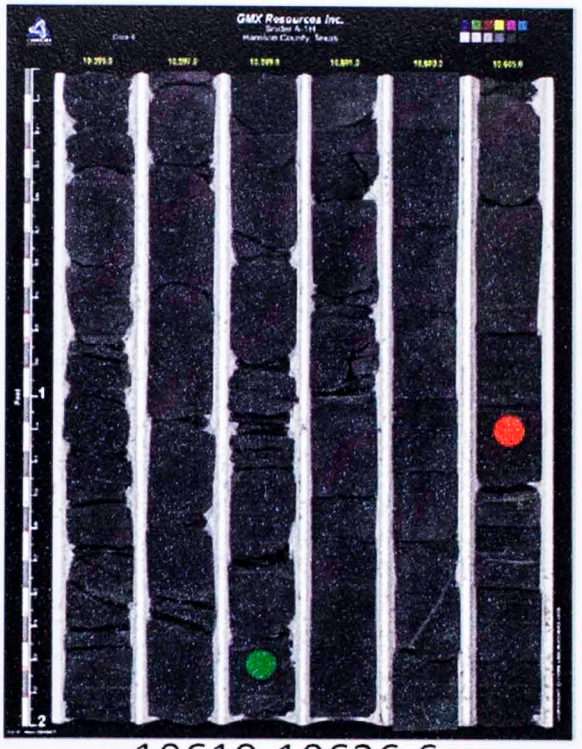

10607-10619

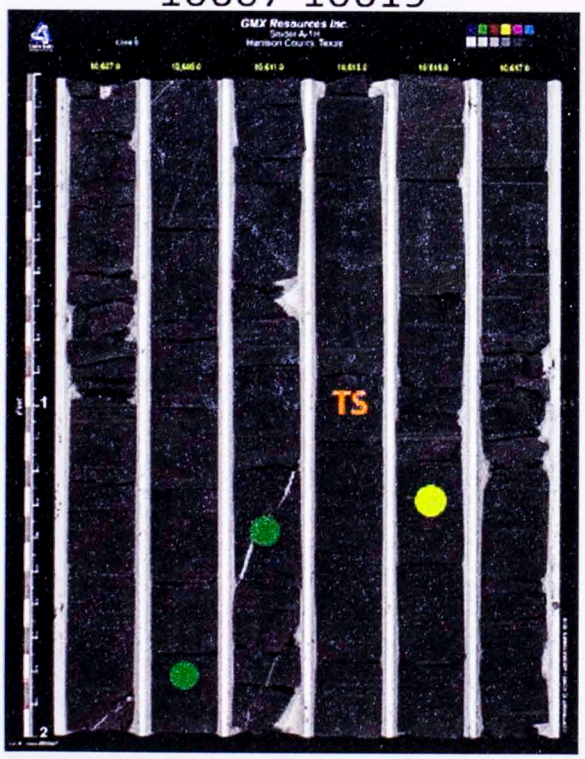

10619-10626.6

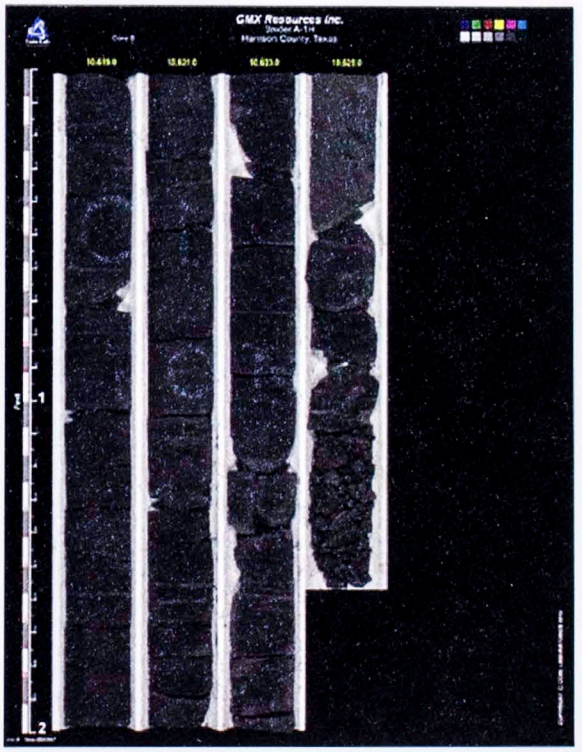

10628-10640

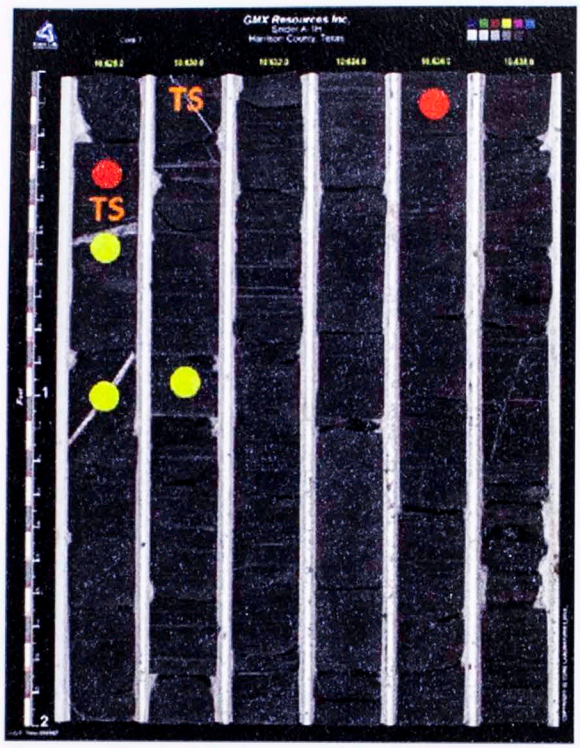

10640-10652

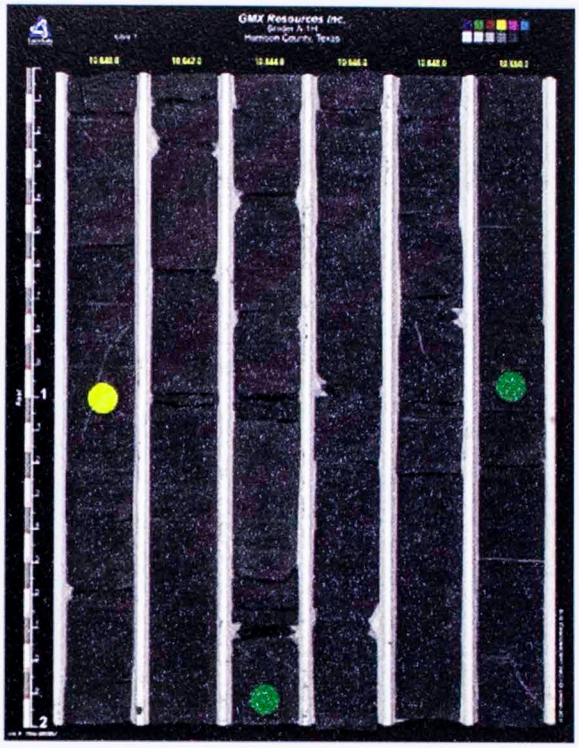

10652-10664

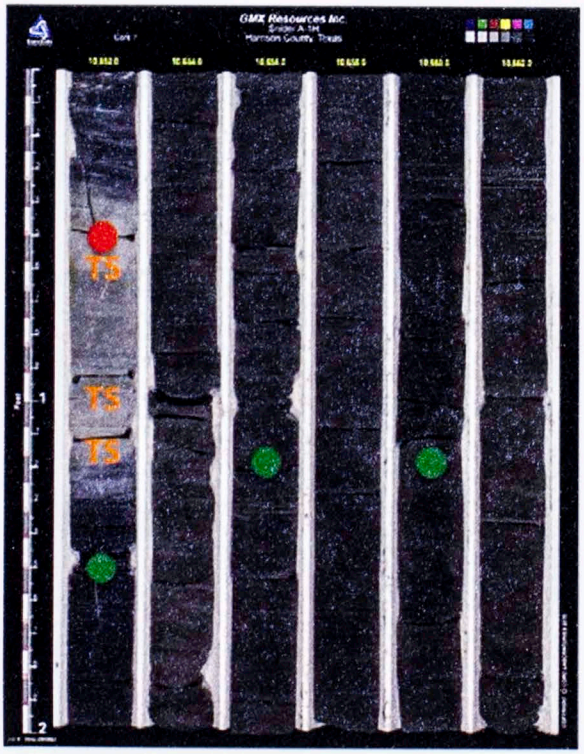

10664-10676

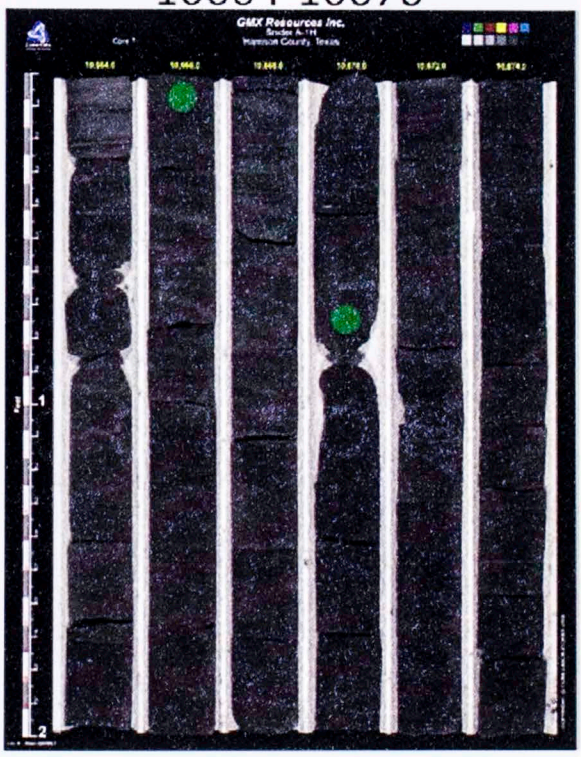

10676-10688

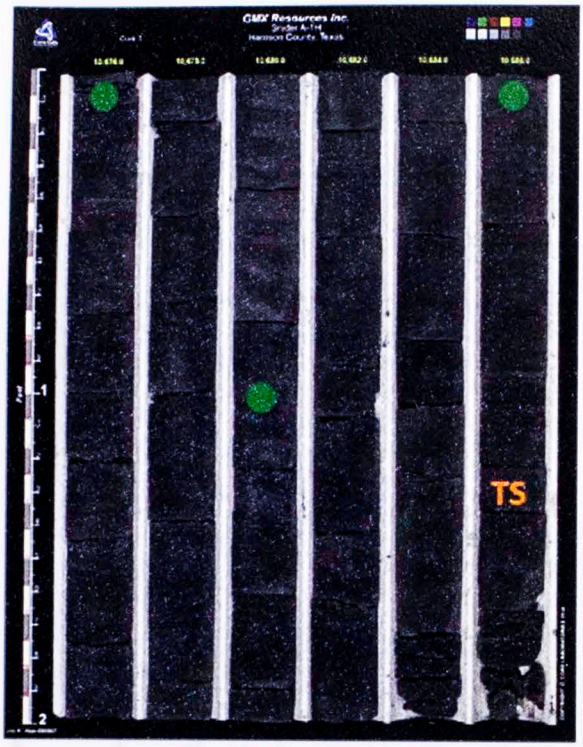

10688-10689.4

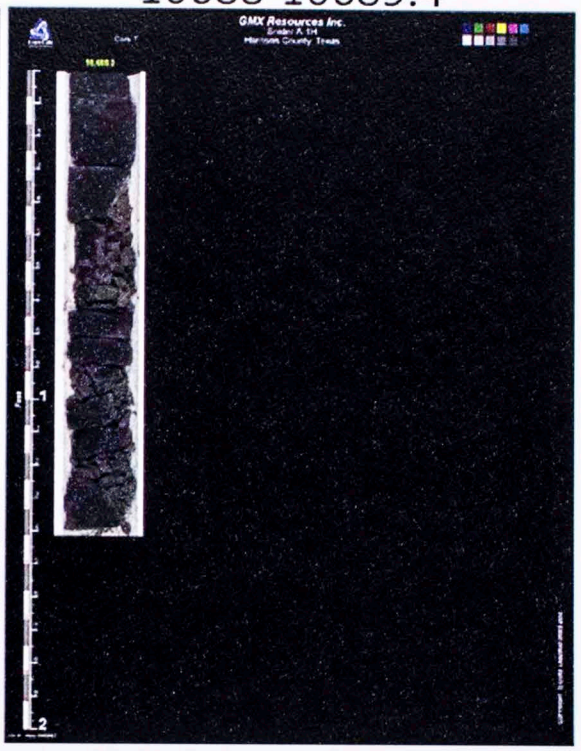

D. Thin section analysis tables for the Snider A1-H and Coleman Gas Unit 1-6 core

Snider A1-H Core Thin Sections	Depth	Abbrev	Classification	Matrix	Veins	Allochems	Misc.	Microscopy
	10324'	**SC-1**	Siliceous Mudstone(burrowed)	shale and quartz grains	calcite- radial, split feature (H)	wavy brachiopod or clam	Dark lenticular clasts in matrix (burrows or detrital clumps of clay)	
	10365'	**SC-2**	Siliceous Mudstone	shale and quartz grains	Saddle Dolomite undulous extinction (V)		dark 'clasts' inside of vein-sulphate rich(not pyrite	REFLECTED LIGHT and Alizarin Red
	10367'	**SC-3**	Siliceous Mudstone	shale and quartz grains	saddle dolomite, more lenticular(H)		early concretions?	
	10372'	**SC-4**	Siliceous Mudstone	shale, quartz and calcite grains	calcite, saddle dolomite in middle(H)			
	10376.5'	**SC-5 a**		detrital carbonate predominant	anhydrite , calcite on edge			
	10376.5'	**SC-5b**		detrital carbonate predominant	some porosity			
		SC-5c		detrital carbonate predominant	anhydrite and celestine:calcite clasts within breccia, anh cross cut by small silica vein			SEM
	10380'	**SC-6**	Siliceous Mudstone	shale and quartz grains	lenticular (split), fossil-dolomite(H)			Alizarin red
	10384'	**SC-7**	burrowed mudstone	burrows			large pyrite concretion	
	10402.5'	**SC-8**	Siliceous Mudstone	shale and quartz grains (coarser)	one large vein, drousy mosaic calcite(V)	brachiopod		Alizarin red
	10402'10"	**SC-8a**	Siliceous Mudstone	shale and quartz with minor detrital carbonate	Drusy mosaic calcite. A few matrix clasts within(V)	bryozoan (calicite replacement)		
	10404'	**SC-9**	Siliceous Mudstone	shale and quartz, calcite grains	none		detrital carbonate?	
	10479'	**SC-10**	Siliceous Mudstone	shale and quartz grains	none			REFLECTED LIGHT
	10481'9"	**SC-11**	Siliceous Mudstone	shale and quartz grains	dolomite vein or fossil cross cut by large vein. Large vein (calcite and dolomite on rim with barite dominant in middle)(V)			REFLECTED LIGHT
	10481'11"	**SC-11a**	Siliceous Mudstone	shale and quartz with minor detrital carbonate	thinner veins: sparry calcite(H). Large vein: blocky calcite, good porosity(V)			

Snider A1-H Core Thin Sections	Depth	Abbrev	Classification	Matrix	Veins	Allochems	Misc.	Microscopy
	10488'4"	**SC-12**	Siliceous Mudstone	shale and quartz grains	small veins-lenticular dolomite filled(H). Large vein-blocky minerals (calcite on edge and dolomite)(V)			CATHOD
	10489'	**SC-12a**	Carbonate-rich mudstone	detrital carbonate predominant	large vein-dolomite and calcite(V)	lenticular and dolomite filled		
	10500.5'	**SC-13**	Siliceous Mudstone	shale and quartz grains	two large veins, calcite(split feature)(H)		hollowed out allochem? Concretion? Has sweeping extiniction	SEM and Cathod
	10501'7"	**SC-13a**	Carbonate-rich mudstone	detrital carbonate predominant	large vein, split parallel by yellower calcite(H)		yellow' (in PPO) terminates in points facing eaching	
	10514.5'	**SC-14**	Siliceous Mudstone	shale and quartz grains	tight spacing, the larger the vein the blockier the dolomite(H)			
	10515'6"	**SC-14a**	Siliceous Mudstone	shale and detrital quartz	large vein, dolomite on outside with multiple events inside-blocky calcite precipitated followed by pyrite(H)			Alizarin red
	10532'	**SC-15**	Siliceous Mudstone	shale and quartz grains	small lenticular veins(dolomite)(H)cross cut by large blocky vein (dolomite)(V)		interesting veining pattern at both ends of large vein(zebra dolomite?). Small veins appear to compose the large perpendicular vein.	Alizarin red
	10531'5"	**SC-15a**	Siliceous Mudstone	shale with detrital quartz and carbonate	largest vein: fibrous twinned calcite perpendicular to vein orientation, second event a blocky to mosaic calcite oriented parallel to vein direction(V). Smaller veins exhibit fibrous feature with faint dirty line splitting (H)down middle. Smallest veins cross-cut 'smaller' veins are composed of silica		"cone-in-cone" has sweeping exctinction	SEM and alizarin
	10534'	**SC-16**	Siliceous Mudstone	shale and quartz grains	two small lenticular veins, sparry calcite(H)			

Snider A1-H Core Thin Sections	Depth	Abbrev	Classification	Matrix	Veins	Allochems	Misc.	Microscopy
	10547'	**SC-17a**	Siliceous Mudstone	shale and quartz grains	small veins-calcite, dirtier(H). Large veins-perpendicular to small and cross-cutting small, also calcite with split feature(V)			
		SC-17b	Siliceous Mudstone	shale and quartz grains	small lenticular veins-dolomite(H). Large vein cross-cuts small perpendicular, baroque dolomite(V)			
	10547'5"	**SC-17c**	Siliceous Mudstone	shale with detrital quartz and carbonate	horizontal veins-dolomite and calcite; vertical veins baroque dolomite . Silca veins throughout. Pyrite in horizontal veins			Alizarin red
	10555'	**SC-18**	Siliceous Mudstone	shale and quartz grains	largest vein baroque dolomite, small veins, dolomite and some with split feature(H)			
	10556'6"	**SC-18a**	Siliceous Mudstone	shale with detrital quartz and carbonate	thin veins- silica(H); thick veins-two (perhaps three)events, calcite precip in both, oldest a dirtier fibrous cement, younger is dolomite, youngest another calcite precip(H)		trace amounts of pyrite spread throughout matrix	Alizarin red
	10564'7"	**SC-19**	Siliceous Mudstone	shale and quartz grains, clast feature	vein, radial calcite, pyrite			Alizarin red
	10565'8"	**SC-19a**	Siliceous Mudstone	shale with detrital quartz and carbonate	one large blocky calcite filled vein(V) split by silica vein(H). A few matrtix clasts within			
	10577'8"	**SC-20**	Siliceous Mudstone	calcite grains (higher quartz, calcite/shale ratio)	anastomizing vein with dolomite, split feature(H)			
	10614'	**SC-21**	Siliceous Mudstone	shale,calcite and quartz grains, clast feature	one vein with microspar and shale(dirty color)(H)			
	10628.5'	**SC-22**	Siliceous Mudstone	calcite grains, dolomite (higher quartz, calcite/shale ratio)	Large vein with calcite(dirty) on edge with barite. Anhydrite in middle. Pyrite in vein(V)			

Snider A1-H Core Thin Sections	Depth	Abbrev	Classification	Matrix	Veins	Allochems	Misc.	Microscopy
	10630'1"	SC-22a	Siliceous Mudstone	shale with detrital quartz and carbonate(higher non-shale ratio than SC19a)	Three sets of veins: oldest run parallel to width of thin section, have blocky to fibrous calcite texture(H). Middle aged set trends 'NE-SW' with blocky texture(V). Youngest is thickest and has Drusy mosaic texture with two 'elbows' (V)		youngest vein appears to have formed synstructurally with shearing event	
	10652'6"	SC-23c	Dolomite	Dolomite with minor silca grains	Silica rich veining/brecciation lined with dark mineral (hydrocarbon?) Calcedony present, matrix clasts within. Small veins filled with block calcite(H)		Diagenetic chert?	
	10653'	SC-23 a	Dolomite	double terminating quartz, saddle dolomite	vugs		Apatite, leucoxene. Hydrothermal fluid alteration?	
		SC23-b	Dolomite	double terminating quartz				SEM
	10687'4"	SC-24	Siliceous Laminated Mudstone	calcite grains (higher quartz, calcite/shale ratio)			high fissility	

Coleman Core Thin Sections	Depth	Abbrev.	Classification	Matrix	Veins	Allochems	Misc.	Microscopy
	10807'10"	CG-1	carbonate-rich mudstone	shale with detrital carbonate and minor silica		minor shell fragments, few crinoids	one 'large' opaque mineral with calcite inside	
	10822'	CG-2	dolostone	dolomite	none	none		
	10830'7"	CG-3A		dirty calcite. Opaque mineral throughout	Pyrite rim, calcite, then barite in middle. Small dolomite vein with quartz?		edge with dolomite,barite	SEM
	10830'7"	CG-3B		dirty calcite. Opaque mineral throughout	Pyrite rim, calcite then barite in middle.			
	10848'2"	CG-5	siliceous mudstone	Shale with detrital silica and minor detrital carbonate	thin silica filled. Intersecting vein has matrix within and minor amounts of silica(H)	a few minor shell fragments(calcite filled)		
	10857'	CG-6	carbonate-rich mudstone	minor shale, detrital carbonate-grain supported				
	10893'7"	CG-7	mudstone	shale with detrital silica and carbonate, minor burrows	none	a few small shell fragments, calcite filled		
	10933'4"	CG-8	mudstone	shale with detrital carbonate and silica, minor burrowing present	small and silica filled	large bivalves(some with impunctate structure), cubic pyrite present	small silica veins cross cut bivalves, including pyrite)	
	10934'6"	CG-9	carbonate-rich mudstone	shale with detrital carbonate and minor silica	none	large brachiopod (impunctate structure), pyrite within. Small brach with middle replaced by pyrite (rim calcite)		
	10951'4"	CG-10	carbonate-rich mudstone	shale with detrital carbonate	minor and silica filled(H)	none	large pyrite laths(appearance of brecciation), a few have sphalerite replacing pyrite.	
	10954'7"	CG-11	siliceous mudstone	very dark shale with detrital silica	very few, but silica filled(H)	shell has pyrite, chert(?), micrite,bladed opaque mineral		REFLECTED LIGHT
	10956'10"	CG-12	mudstone	shale with equal parts detriral carbonate and silica	small and silica filled(H)	Large allochem has pyrite as well as shell frags replaced by sphalerite, crushed cephalopod shells		SEM and REFLECTED LIGHT
	10973'8"	CG-13	siliceous mudstone	Shale with detrital silica and minor carbonate		large- solution reprecipitaiton, micrite on rim with baroque dolomite in middle	(edge with calcite perpendicular, radial) and (small barite in middle of calcite	SEM and REFLECTED LIGHT
	10975'9"	CG-14	siliceous mudstone	shale with detrital silica		Crinoids in matrix, fractured stromatolites? Large bivalves		

Coleman Core Thin Sections	Depth	Abbrev.	Classification	Matrix	Veins	Allochems	Misc.	Microscopy
	10981'6"	CG-15	siliceous mudstone	dark shale with silica and minor carbonate grains	small and silica filled(H)	wavy and filled with drousy mosaic calcite	pyrite grains in matrix	alizarin red
	11003'8"	CG-16	siliceous mudstone	Shale with detrital silica and minor carbonate	minor lenticular silica veins(H)	Shell filled in three stages (silica on rim with two calcite precipitation events within), radial and drousy mosaic		alizarin red
	11004'1"	CG-17	siliceous mudstone	Shale with detrital silica and minor carbonate	minor lenticular silica veins	shell frags filled with calcite and polycrystalline quartz(early silica) . Large shell has radial calcite and impunctate structure	baroque dolomite allochem cross cut by minor silica vein	alizarin red
	11015'	CG-18	burrowed mudstone	shale with minor detrital carbonate and silica	some minor silica filled veins(H)	bivalve fragments (calcite, dolomite and pyrite)	burrows filled with micrite	
	11016'6"	CG-19	burrowed mudstone	shale with detrital carbonate	anastomizing vein filled with calcite (post burrowing, veining moves around burrows)(V)		burrows throughout matrix	
	11025'7"	CG-20	laminated siliceous mudstone	Shale with detrital silica and minor carbonate	minor lenticular silica veins(H)	small shell-three events, silica rim, calcite precip followed by pyritization. Large shell- three events, silica rim and two calcite precipitations, radial and drousy mosaic fabric		
	11029'7"	CG-21	laminated siliceous mudstone	shale with detrital silica	small and silica filled(H)		hand sample more highly fissle due to silica content, speaks to fractability of silica vs. carbonate	
	11039'2"	CG-22	siliceous mudstone	shale with silica, highly veined	small and silica filled(H)	large fragmented bivavles (impunctate structure, calcite and dolomite and pyrite), formed syndepositially(note curving of matrix around vertical shell frags)	Sphalerite(confirmed in SEM)	
	11040'6"	CG-23	siliceous mudstone	shale with detrital silica	small and silica filled(H)	large fractured shell-edge has vein like feature(solution seams), middle baroque dolomite, pyrite and sphalerite		REFLECTED LIGHT

Coleman Core Thin Sections	Depth	Abbrev.	Classification	Matrix	Veins	Allochems	Misc.	Microscopy
	11050'4"	CG-24	laminated siliceous mudstone	shale with detrital silica	small and silica filled(H)	shells filled with at least two stages of calcite. Thicker shell has barite as well	fracturing and pyritization occurred syndepositionally(see shale surrounding 'break out' points. It looks as though sulphur rich fluids came through and broke apart shell.	
	11056'9"	CG-25	laminated siliceous mudstone	shale with detrital silica (more silica than CG-23/24)	small and silica filled(H)	shell with fibrous calcite, a portion replaced by pyrite		
	11060'6"	CG-26	burrowed mudstone	shale with detrital silica (more silica than CG-23/24)	small and silica filled with minor porosity(H).Large anastomizing vein filled with calcite (post burrowing, veining moves around burrows)(V)		burrows throughout matrix	
	11067'7"	CG-27	burrowed mudstone	shale with micrite filled burrows	some minor veins with silca and some micrite on rim(H)	peloids (?) a few crinoids		
	11073'10"	CG-28	burrowed mudstone	Shale with detrital silica and minor carbonate. Small lenticular dark bands(burrows?)	small and silica filled(H)	shell has silica on rim in one zone, has thick micrite on another zone with calcite(impunctate structure) in middle. Also pyrite replacement	sphalerite present	
	11077'6"	CG-29	burrowed mudstone	shale with detrital silica and micrite filled burrows	minor silica filled veins(H)	bivalve fragments filled with blocky calcite. One shell has pyrite rim. Largest shell has drousy mosiac and radial calcite with silica on rim and lastly pyrite replacement		
	11083'6"	CG-30	burrowed mudstone	shale with detrital silica, some zones have dark lenticular lenses	small and silica filled throughout(H)	none		
	11086'2"	CG-31	burrowed mudstone	shale with silica grains and minor burrows and veins	small and silica filled(H)	diagonal shell filled with blocky calcite	sphalerite cross cut by silica vein. Note how diagonal allochem/vein occurred syndepositionally (burrow curves alongside it)	